



UNIVERSIDADE FEDERAL DO CEARÁ
CENTRO DE TECNOLOGIA
DEPARTAMENTO DE ENGENHARIA HIDRÁULICA E AMBIENTAL
PROGRAMA DE PÓS-GRADUAÇÃO EM ENGENHARIA CIVIL (RECURSOS
HÍDRICOS)

MARCELA VERÍCIMO DO NASCIMENTO

PHOTOCATALYTIC STUDY OF COMPOSITES BASED ON TITANIUM DIOXIDE
(TiO₂) AND GRAPHITIC CARBON NITRIDE (g-C₃N₄) UNDER ARTIFICIAL AND
NATURAL LIGHT

FORTALEZA

2023

MARCELA VERÍCIMO DO NASCIMENTO

PHOTOCATALYTIC STUDY OF COMPOSITES BASED ON TITANIUM DIOXIDE
(TiO₂) AND GRAPHITIC CARBON NITRIDE (g-C₃N₄) UNDER ARTIFICIAL AND
NATURAL LIGHT

Dissertação apresentada ao Programa de Pós-Graduação em Engenharia Civil (Recursos Hídricos) da Universidade Federal do Ceará, como requisito parcial à obtenção do título de Mestre em Engenharia Civil.

Área de concentração: Saneamento Ambiental

Orientador: Prof. Dr. José Capelo Neto.

Coorientador: Prof. Dr. Bruno César Barroso Salgado.

FORTALEZA

2023

Dados Internacionais de Catalogação na Publicação
Universidade Federal do Ceará
Sistema de Bibliotecas
Gerada automaticamente pelo módulo Catalog, mediante os dados fornecidos pelo(a) autor(a)

N196p Nascimento, Marcela Verícimo do.
Photocatalytic study of composites based on titanium dioxide (TiO₂) and graphitic carbon nitride (g-C₃N₄) under artificial and natural light / Marcela Verícimo do Nascimento. – 2023.
87 f. : il. color.

Dissertação (mestrado) – Universidade Federal do Ceará, Centro de Tecnologia, Programa de Pós-Graduação em Engenharia Civil: Recursos Hídricos, Fortaleza, 2023.

Orientação: Prof. Dr. José Capelo Neto .

Coorientação: Prof. Dr. Bruno César Barroso Salgado.

1. synthesis. 2. photocatalysis. 3. dye removal. 4. response surface. I. Título.

CDD 627

MARCELA VERÍCIMO DO NASCIMENTO

PHOTOCATALYTIC STUDY OF COMPOSITES BASED ON TITANIUM DIOXIDE
(TiO₂) AND GRAPHITIC CARBON NITRIDE (g-C₃N₄) ARTIFICIAL AND NATURAL
LIGHT

Dissertação apresentada ao Programa de Pós-Graduação em Engenharia Civil (Recursos Hídricos) da Universidade Federal do Ceará, como requisito parcial à obtenção do título de Mestre em Engenharia Civil.
Área de concentração: Saneamento Ambiental.

Aprovada em: __/__/____.

BANCA EXAMINADORA

Prof. Dr. José Capelo Neto (Orientador)
Universidade Federal do Ceará (UFC)

Prof. Dr. Bruno César Barroso Salgado (Coorientador)
Instituto Federal do Ceará (IFCE)

Dr. Carlos João Pestana
Robert Gordon University (RGU)

A Deus e Nossa Senhora de Guadalupe.

Aos meus pais, José e Bernardete.

AGRADECIMENTOS

O presente trabalho foi realizado com apoio da Coordenação de Aperfeiçoamento de Pessoal de Nível Superior – Brasil (CAPES) – Código de Financiamento 001.

Agradeço a Deus, pela fortaleza concedida para planejar, desenvolver e concluir este trabalho.

Ao Prof. Dr. José Capelo Neto, pela orientação, incentivo e solicitude para o desenvolvimento desta pesquisa.

Aos professores participantes da banca examinadora pelo tempo disponibilizado, pelas valiosas colaborações e sugestões.

Aos amigos do laboratório SELAQUA, que contribuíram com sugestões e auxílio técnico, em especial Raphael, Leonardo, Kelly, André e Thaís.

RESUMO

O tratamento fotocatalítico tem atraído a comunidade científica devido à produção de espécies reativas de oxigênio (ERO). Nos últimos anos, as ERO mostraram o potencial para eliminar vários tipos de poluentes. A busca por desenvolver materiais semicondutores com o aproveitamento eficiente da luz e a utilização de fontes de energia mais limpas tem sido cada vez mais comum nas publicações. Nesse contexto, o primeiro estudo objetivou sistematizar as inovações na síntese de compósitos constituídos por dióxido de titânio (TiO_2) e nitreto de carbono grafítico (g- C_3N_4). Alguns termos foram utilizados para pesquisar publicações na base de dados bibliográfica Compendex entre 2015 e 2021. Os artigos foram incluídos e excluídos de acordo com critérios específicos. Posteriormente, os artigos remanescentes foram organizados a partir da morfologia do TiO_2 e do número de publicações. Essa revisão sistemática permitiu a identificação da variabilidade morfológica nos compósitos e predominância das nanopartículas de TiO_2 . Além disso, métodos sintéticos novos, como deposição de camada atômica, deposição de vapor e agregação induzida por carga, foram desenvolvidos. A segunda parte desse trabalho desenvolveu um estudo fotocatalítico a partir da síntese de compósitos baseados em dióxido de titânio (P25) e nitreto de carbono grafítico (CN). Para esse propósito, dois reatores foram planejados para observar as respostas dos materiais (CN, CN25, CN75 e P25) às fontes de luz artificial e natural fornecidas por uma lâmpada halógena e pela exposição solar, respectivamente. Soluções contendo azul de metileno (AM) com uma concentração de 10 mg/L foram tratadas por fotocatalise. A aplicação do Delineamento do Composto Central (DCC) auxiliou na compreensão da influência dos parâmetros (pH, concentração inicial do AM e dosagem do P25) na remoção do corante. Os resultados mostraram que o P25 melhorou a resposta fotocatalítica do CN. Entretanto, o P25 no estado puro alcançou as mais altas remoções em ambas fontes luminosas. O P25 alcançou a remoção de 99,4% em 1 h sob luz solar. Os pontos críticos determinados pelo DCC foram 6,6, 1,2 g/L e 1 mg/L. O modelo cinético de primeira ordem ajustado ao processo fotocatalítico gerou o k de $0,07 \text{ min}^{-1}$. Essa modelagem mostrou que a taxa de remoção dobrou após 30 minutos de ensaio. Os resultados experimentais indicaram um potencial alto para aplicação da fotocatalise heterogênea ativada por luz solar.

Palavras-chave: síntese; fotocatalise; remoção de corante; superfície de resposta.

ABSTRACT

Photocatalytic treatment has attracted the scientific community due to the production of reactive oxygen species (ROS). In recent years, ROS has shown the potential to eliminate several pollutant types. The search to develop semiconductor materials with efficient use of light and utilization of cleaner energy sources has been increasingly common in publications. In this context, the first study aimed to systematize innovations in composite synthesis constituted by the titanium dioxide (TiO₂) and graphitic carbon nitride (g-C₃N₄). Some terms were used to search the publications in Compendex bibliographic database between 2015 and 2021. Papers were included and excluded according to specific criteria. Subsequently, the remaining papers were organized from TiO₂ morphology and the number of publications. This systematic review allowed the identification of morphological variability in composites and the predominance of TiO₂ nanoparticles. In addition, new synthetic methods, such as atomic layer deposition, vapor deposition, and charge-induced aggregation, were developed. The second part of this work developed a photocatalytic study from composite synthesis based on titanium dioxide (P25) and graphitic carbon nitride (CN). For this purpose, two reactors were designed to observe materials responses (CN, CN25, CN75, and P25) to the artificial and natural light sources provided by a halogen lamp and sun exposure, respectively. Solutions containing methylene blue (MB) with an initial concentration of 10 mg/L were treated by photocatalysis. The application of Central Composite Design (CCD) aided in understanding parameters influence (pH, MB initial concentration, and P25 dosage) on the dye removal. The findings showed that P25 improved the photocatalytic response of the CN. However, pristine P25 achieved the highest removals in both light sources. P25 reached the average removal of 99.4% at 1 h under sunlight. The critical points determined by CCD for pH, P25, and MB were 6.6, 1.2 g/L, and 1 mg/L, respectively. The First-order kinetic model adjusted to the photocatalytic process generated the k value of 0.07 min⁻¹. This modeling showed that the removal rate doubled after 30 minutes of testing. Experimental results indicated a high potential for the utilization of heterogeneous photocatalysis activated by sunlight.

Keywords: synthesis; photocatalysis; dye removal; response surface.

LIST OF FIGURES

CHAPTER I

Figure 1	– Classification according to the TiO ₂ morphology found in remaining papers	20
Figure 2	– (A) The annual number of publications and (B) classification groups of the publications	21
Figure 3	– Transmission electron microscopy (TEM) images of composites (A) M0+g-C ₃ N ₄ and (B) M400	22
Figure 4	– Schematic illustration of the synthesis of g-C ₃ N ₄ /TiO ₂ composite via vapor deposition	23
Figure 5	– The schematic diagram of the synthetic route.....	23
Figure 6	– (A) Image of transmission electron microscopy (TEM) and (B) magnified image of Ti ³⁺ doped TiO ₂ mesocrystals	32
Figure 7	– Scanning electron microscope (SEM) images of (A) TiO ₂ and (B) gCN/TO5	35
Figure 8	– Transmission electron microscopy (TEM) images of g-C ₃ N ₄ /TNTs-2	38
Figure 9	– Scanning electron microscope (SEM) image of TCN–K5 sample	40
Figure 10	– (A) Transmission electronic microscopy (TEM) image and (B) high-resolution transmission electron microscopy (HRTEM) image of TiO ₂ @g-C ₃ N ₄	41
Figure 11	– Scanning electron microscope (SEM) images of (A) CNT-0 (pristine TiO ₂ hollow microsphere) and (B) CNT-15	42
Figure 12	– Schematic illustration of the preparation of C-TiO ₂ @g-C ₃ N ₄	42
Figure 13	– Transmission electron microscopy (TEM) image of photocatalyst sample (gT600)	45

CHAPTER II

Figure 1	– Schematic illustration of reactor A	59
Figure 2	– Schematic illustration of reactor B	60
Figure 3	– MB removal by photocatalysts under artificial light in reactor A (Experimental conditions: photocatalyst dosage = 0.5 g/L; MB = 10 mg/L; V = 50 mL; contact time = 7 h)	64
Figure 4	– MB removal by photocatalysts under artificial light in reactor B (Experimental conditions: photocatalyst dosage = 0.5 g/L; MB = 10 mg/L; V = 200 mL; contact time = 1 h; agitation speed = 50 rpm)	66
Figure 5	– (A) MB removal by photocatalysts under sunlight irradiation and (B) light intensity data recorded in reactor B (Experimental conditions: photocatalyst dosage = 0.5 g/L; MB = 10 mg/L; V = 200 mL; contact time = 1 h; agitation speed = 50 rpm)	67
Figure 6	– Dye removal promoted by treatments with different photocatalysts (photocatalysis) and without photocatalyst (photolysis) in reactor B	68
Figure 7	– Plot of (A) experimental responses <i>versus</i> predicted responses for MB removal and (B) normal probability for raw residuals	69
Figure 8	– Pareto chart containing the effect of all factors on the MB removal	70
Figure 9	– (A) 3D response surface plots and (B) 2D contour plots for P25 <i>versus</i> pH (Experimental conditions: V = 200 mL; contact time = 1 h; agitation speed = 50 rpm)	71
Figure 10	– (A) 3D response surface plots and (B) 2D contour plots for MB <i>versus</i> P25 (Experimental conditions: V = 200 mL; contact time = 1 h; agitation speed = 50 rpm)	72
Figure 11	– (A) 3D response surface plots and (B) 2D contour plots for MB <i>versus</i> pH (Experimental conditions: V = 200 mL; contact time = 1 h; agitation speed = 50 rpm)	73

Figure 12 – First-order kinetic model of MB removal by P25 adjusted to (A) L1 and (B) L1 and L2 (Experimental conditions: pH = 6.6; P25 dosage = 1.2 g/L; MB = 10 mg/L; V = 200 mL; contact time = 1 h; agitation speed = 50 rpm) 75

LIST OF TABLES

CHAPTER I

Table 1	– Synthetic methods of composites with non-modified TiO ₂ nanoparticles and non-doped g-C ₃ N ₄ nanosheets	24
Table 2	– Synthetic methods of composites with non-modified TiO ₂ nanoparticles and doped g-C ₃ N ₄ nanosheets	27
Table 3	– Synthetics methods of composites with modified TiO ₂ nanoparticles and non-doped g-C ₃ N ₄ nanosheets	29
Table 4	– Synthetics methods of composites with modified TiO ₂ nanoparticles and doped g-C ₃ N ₄ nanosheets	31
Table 5	– Synthetic methods of composites with TiO ₂ mesocrystals and g-C ₃ N ₄ nanosheets	33
Table 6	– Preparation methods of composites formed by TiO ₂ quantum dots and g-C ₃ N ₄ nanosheets	34
Table 7	– Synthetic methods of composites with TiO ₂ nanosheets and non-doped g-C ₃ N ₄ nanosheets	36
Table 8	– Synthetic methods of composites with TiO ₂ nanosheets and doped g-C ₃ N ₄ nanosheets.....	37
Table 9	– Synthetic methods of composites with TiO ₂ nanotubes and g-C ₃ N ₄ nanosheets	38
Table 10	– Synthetic methods of composites with TiO ₂ nanofibers, nanowires, and nanobelts and g-C ₃ N ₄ nanosheets	40
Table 11	– Synthetic methods of composites with TiO ₂ nanorods and g-C ₃ N ₄ nanosheets	42
Table 12	– Synthetic methods of composites with TiO ₂ spheres and g-C ₃ N ₄ nanosheets	44
Table 13	– Synthetic methods of composites with TiO ₂ different morphologies and g-C ₃ N ₄ nanosheets	46

CHAPTER II

Table 1	– Name and composition of photocatalysts used in experiments	60
Table 2	– Factors and levels (coded and uncoded) used in the CCD with $\alpha = 1.68$	62
Table 3	– Statistical tests of dye removal data by photocatalysts under artificial light	64
Table 4	– Statistical tests of dye removal data by photocatalysts under sunlight	65
Table 5	– Statistical tests of dye removal data by photocatalysts under sunlight with light intensity monitoring	66
Table 6	– Critical values of the factors for MB removal	74
Table 7	– Parameters of linear fit for MB removal by P25	76

LISTA DE ABREVIATURAS E SIGLAS

MB	Methylene blue
CCD	Central Composite Design
MOF	Organic-metal framework
CBM	Conduction band minimum
ROS	Reactive oxygen species
AOP	Advanced Oxidative Process

TABLE OF CONTENTS

GENERAL INTRODUCTION	16
CHAPTER I	
1 INTRODUCTION	18
2 METHODOLOGY	19
2.1 Search strategies	19
2.2 Inclusion and exclusion criteria	19
2.3 Conduction of systematic review and data	20
3 RESULTS	21
3.1 Literature search	21
3.2 Non-modified TiO₂ nanoparticles	21
3.2.1 Non-doped g-C₃N₄ nanosheets	21
3.2.2 Doped g-C₃N₄ nanosheets	25
3.3 Modified TiO₂ nanoparticles	27
3.3.1 Non-doped g-C₃N₄ nanosheets	27
3.3.2 Doped g-C₃N₄ nanosheets	30
3.4 TiO₂ mesocrystals	32
3.5 TiO₂ quantum dots	33
3.6 TiO₂ nanosheets	34
3.6.1 Non-doped g-C₃N₄ nanosheets	34
3.6.2 Doped g-C₃N₄ nanosheets	36
3.7 TiO₂ nanotubes	37
3.8 TiO₂ nanofibers, nanowires and nanobelts	39
3.9 TiO₂ nanorods	41
3.10 TiO₂ spheres	42
3.11 Different morphologies	44
4 DISCUSSION	46
5 CONCLUSION	49
REFERENCES	51

CHAPTER II

1 INTRODUCTION	57
2 METHODOLOGY	58
2.1 Materials	58
2.2 Synthesis of graphitic carbon nitride (CN)	58
2.3 Synthesis of CN/P25 composites	59
2.4 Reactors design	59
2.5 Photocatalytic tests	60
2.6 Statistical analysis	61
2.6.1 Central Composite Design (CCD)	61
2.7 Kinetics of photocatalysis	63
3 RESULTS AND DISCUSSION	63
3.1 Photocatalysis of composites under artificial light	63
3.2 Photocatalysis of composites under sunlight	65
3.3 Central composite design (CCD)	68
3.3.1 Predictive model	68
3.3.2 Response surface analysis	70
3.3.3 Determination of optimal conditions for MB removal	73
3.4 Kinetics of photocatalysis	75
4 CONCLUSIONS	76
REFERENCES	78
GENERAL CONCLUSIONS	83
GENERAL REFERENCES	84

1 GENERAL INTRODUCTION

Heterogeneous photocatalysis is recognized among the Advanced Oxidative Processes (AOP) because it represents a renewable, economical, simple, and efficient alternative (ATUL *et al.*, 2013; BIANCHI *et al.*, 2006; GÓMEZ-PASTORA *et al.*, 2017; LI *et al.*, 2016; SRIKANTH *et al.*, 2017). Process efficiency is related to reactive oxidative species produced, such as hydroxyl radicals, superoxide ions, and peroxy radicals (JOSEPH; VIJAYANANDAN, 2021; PRIHOD'KO; SOBOLEVA, 2013). These molecules promote a selectivity lack, allowing the removal of several pollutants as organic and inorganic molecules and pathogenic microorganisms (ARSLAN-ALATON; TURELI; OLMEZ-HANCI, 2009; MECHA *et al.*, 2019; PONIEDZIAŁEK; RZYMSKI; WIKTOROWICZ, 2014).

One of the most used dyes in photocatalysis studies is methylene blue (MB) (ZHANG *et al.*, 2010). This azo dye with an aromatic structure also is widely applied in the textile industry (SARKAR *et al.*, 2020; WANG *et al.*, 2022). The high chemical stability of dyes is responsible for remaining in the environment for long periods and their low biodegradability (BASTURK; KARATAS, 2015; ISARI *et al.*, 2018; SUN *et al.*, 2019). Azo dyes are found in several textile effluents, representing a threat when discharged untreated into water bodies (SAEED *et al.*, 2022; SARKAR *et al.*, 2020). Photocatalysis is particularly attractive to the industrial effluent treatment field since it can eliminate aromatic compounds. (BENKHAYA; M' RABET; EL HARFI, 2020; HERRMANN, 2005).

Conventional treatment methods have been ineffective in successful dye degradation, generating the necessity to waste treatment (TU *et al.*, 2019). While coagulation and flocculation only transfer the pollutant phase, heterogeneous photocatalysis promotes contaminating substances destruction (AHMED; HAIDER, 2018; DARIANI *et al.*, 2016a). Furthermore, coagulation contains the risk of secondary pollution when the treatment of resulting sludge is inadequate (AL-MAMUN *et al.*, 2019). Photocatalytic treatment from redox reactions can convert pollutants into CO₂, H₂O, and inorganic ions (BADVI; JAVANBAKHT, 2021; MOUSAVI; HABIBI-YANGJEH; POURAN, 2018).

The search for aligning photocatalysis with cleaner energy source has grown. A light source appropriate to the semiconductor bandgap and oxygen availability is fundamental to conducting the photocatalytic process under ambient conditions (CHATTERJEE; DASGUPTA, 2005; REZA; KURNY; GULSHAN, 2017). The use of sunlight as a photon source has become photocatalysis more economical, reducing the utilization of expensive lamps and system maintenance (DIN *et al.*, 2021; MOREIRA *et al.*, 2018). The photons absorption

promotes electron and hole pairs production, inducing a series of redox reactions on the photocatalyst surface (BHANVASE; SHENDE; SONAWANE, 2017; WANG *et al.*, 2015).

Titanium dioxide (TiO₂) has strongly attracted the research field for its promising properties (low toxicity, chemical and biological stability, low cost, and high efficiency) (HUANG *et al.*, 2021; TU *et al.*, 2019; XU *et al.*, 2017; ZHANG *et al.*, 2011b). The TiO₂ wide bandgap (3.2 eV) is active by ultraviolet light (UV) and only 4% of the solar spectrum contains UV (PAN *et al.*, 2013; WU *et al.*, 2017). The recombination of photogenerated pairs (electrons and holes) is common among semiconductors, including pristine TiO₂, becoming its effect harmful to the production of oxidative species (PEIRIS *et al.*, 2021). The scientific community aims to overcome the TiO₂ limitations by reducing bandgap energy, promoting charge separation, and using visible light that is 42% of solar radiation (BAI *et al.*, 2019; SERPONE; EMELINE, 2012; TAYEL; RAMADAN; EL SEOUD, 2018).

Among alternatives for semiconductors modification, the junction of TiO₂ with other materials has been adopted to enhance photocatalytic activity (FEIZPOOR; HABIBI-YANGJEH; VADIVEL, 2017; ZHU; ZHOU, 2019). Graphitic carbon nitride (g-C₃N₄), a polymeric semiconductor, has been used for its activity under visible light (MONGA; BASU, 2019). In general, this study aimed to evaluate the photocatalytic activity of composites synthesized with TiO₂ and g-C₃N₄ under artificial and natural light. For this, it was necessary: to investigate the synthetic methods of composites based TiO₂ and g-C₃N₄, to evaluate the photocatalytic performance of synthesized composites, and to analyze the influence of pH factors, initial concentration, and photocatalyst dosage of the material with greater performance.

The master dissertation structure is organized into five parts: (i) general introduction; (ii) chapter I containing review paper; (iii) chapter II containing research paper; (iv) general conclusion; (v) general introduction references. The papers are manuscripts prepared for submission, that are presented in the chapters.

CHAPTER I

COMPOSITES SYNTHESIS BASED ON TITANIUM DIOXIDE (TiO₂) AND GRAPHITIC CARBON NITRIDE (g-C₃N₄) WITH PHOTOCATALYTIC ACTIVITY UNDER VISIBLE LIGHT – A SYSTEMATIC REVIEW

ABSTRACT

Heterogeneous photocatalysis generates reactive oxidative species, enabling pollutants mineralization into carbon dioxide and water. The scientific community has studied semiconductors materials synthesis with high photocatalytic activity to promote depollution. One of the most promising strategies is coupling titanium dioxide (TiO₂) with graphitic carbon nitride (g-C₃N₄) to enhance photocatalytic activity under visible light. This review aimed to systematize information about composites synthesis methods based on TiO₂ and g-C₃N₄, as well as parameters linked to their heterojunctions characteristics. For this purpose, literatures published between 2015 and 2021 were investigated in the Compendex database in a systematic way. From the results was possible to know synthesis methods and the parameters studied in recent years. Also, this work may contribute to the identification of synthesis modifications to improve visible light absorption and increase the efficiency of electron-hole pairs of semiconductors.

Keywords: photocatalysis; annealing; solvothermal; doping; heterostructure.

1 INTRODUCTION

Heterogeneous photocatalysis has been considered a promising Advanced Oxidative Process (AOP) (SOLOMON *et al.*, 2012). It produces free radicals with strong oxidizing power, mainly hydroxyl radicals, eventually mineralizing the pollutants into carbon dioxide and water (BALAKRISHNAN; CHINTHALA, 2022; KHEDR *et al.*, 2019). During photocatalysis the conversion of photon energy absorbed into chemical energy occurs, offering great potential for many applications mainly in water and wastewater treatment (AHMED; HAIDER, 2018). Studies in the area of photocatalysis have aroused interest from the work developed by Honda and Fujishima (FUJISHIMA; HONDA, 1972; OHTANI, 2010), enabling the understanding of photoelectrochemical water splitting with single-crystal electrode.

Titanium dioxide (TiO₂) is a material with high photocatalytic activity, good chemical stability, non-toxic, low cost, and eco-friendly (CHEN; MAO, 2007; LAI *et al.*, 2016; SRIDHARAN; JANG; PARK, 2013). Among the TiO₂ polymorphic forms, rutile is the most

stable and anatase is the most active photocatalyst (HU; TSAI; HUANG, 2003). Unfortunately, TiO_2 can absorb only ultraviolet radiations (about 5% of solar light) due to its large bandgap (~ 3.2 eV, < 380 nm), making its application under solar radiation unfeasible (TANG *et al.*, 2016; ZHANG *et al.*, 2011a). A competitive strategy to synthesize composites with TiO_2 for practical applications is to extend light absorption to the visible spectrum and reduce the photoinduced electron-hole pairs recombination (TANG *et al.*, 2016).

Among various strategies, coupling TiO_2 with other semiconductors to form heterojunction can be used to enhance photocatalytic efficiency (LI *et al.*, 2015d). In that sense, graphitic carbon nitride (g- C_3N_4) has been applied due to the narrow bandgap (2.7 eV) and for being chemically stable, non-toxic properties, easily synthesized, and “earth-abundant” (LOW *et al.*, 2014). However, the photocatalytic performance of g- C_3N_4 is limited by moderately low efficiency, lower specific surface area, and high recombination rate of electron-hole pairs (SRIDHARAN; JANG; PARK, 2013; ZHANG *et al.*, 2011a).

Heterojunctions formed by TiO_2 and g- C_3N_4 have demonstrated the ability to reduce the recombination of photogenerated electron-hole pairs and to enhance the photocatalytic activity of TiO_2 under visible light (FAGAN *et al.*, 2016; QU *et al.*, 2016). This systematic review aimed to identify synthesis methods applied to composites manufacturing based on TiO_2 and g- C_3N_4 , their production parameters, and effects on their characteristics.

2 METHODOLOGY

2.1 Search strategies

An exploratory analysis was conducted to find keywords used in review articles focused on the synthesis of composite based on g- C_3N_4 and TiO_2 with activity under visible light. Compendex (Computerized engineering index) is the most comprehensive and complete database of engineering literature available in the world (DRESSEL, 2017). Terms were searched in the Compendex database through Capes Periodical Portal in title, abstract, and keywords of articles published from 2015 to 2021. The systematic search in the electronic database used the following terms "titanium dioxide OR TiO_2 " AND "graphitic carbon nitride or g- C_3N_4 " AND "photocatalyst OR photocatalysis" AND "composite or heterojunction" AND "visible light".

2.2 Inclusion and exclusion criteria

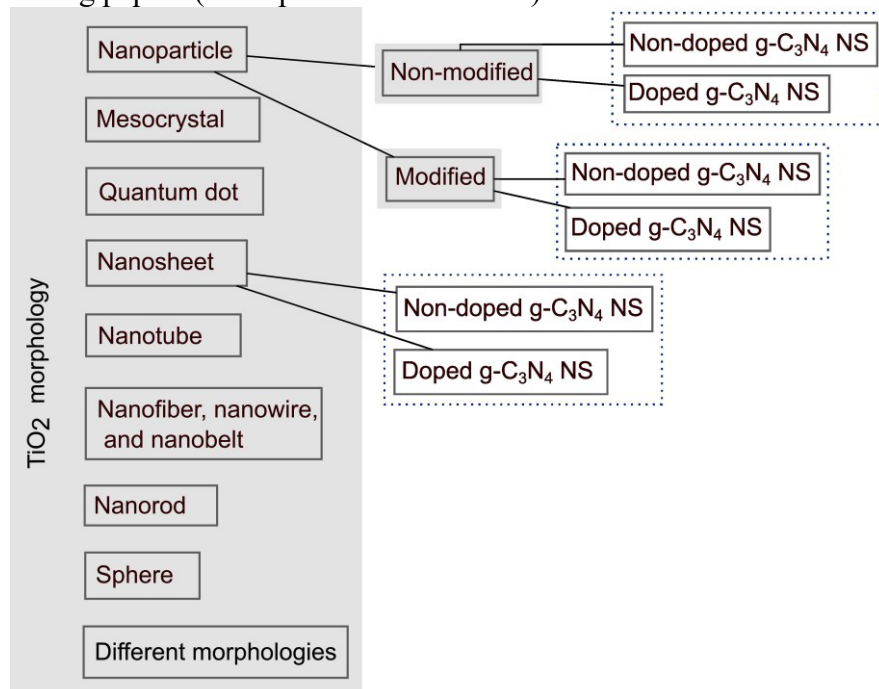
Literature screening was applied from a check of criteria on abstracts and full texts of remaining papers. These inclusion and exclusion criteria were:

- i) Papers focused on binary composites published in the English language were included in the systematic review;
- ii) Publications about non-binary composites, papers published in other languages, and review articles were excluded from the study.

2.3 Conduction of systematic review and data extraction

Selected articles were divided into groups according to the morphology of titanium dioxide and number of publications: (a) non-modified TiO₂ nanoparticles; (b) modified TiO₂ nanoparticles; (c) TiO₂ mesocrystals; (d) TiO₂ quantum dots; (e) TiO₂ nanosheets; (f) TiO₂ nanotubes; (g) TiO₂ nanofibers, nanowires and nanobelts; (h) TiO₂ nanorods; (i) TiO₂ spheres; (j) different morphologies. The information related to the precursors of titanium dioxide and graphitic carbon nitride, mixing technique of the precursors, coupling technique to form the interface, variable parameters in the preparation method, surface area, and the composite bandgap were systematized in tables.

Figure 1 – Classification according to the TiO₂ morphology found in remaining papers (NS represents nanosheets)



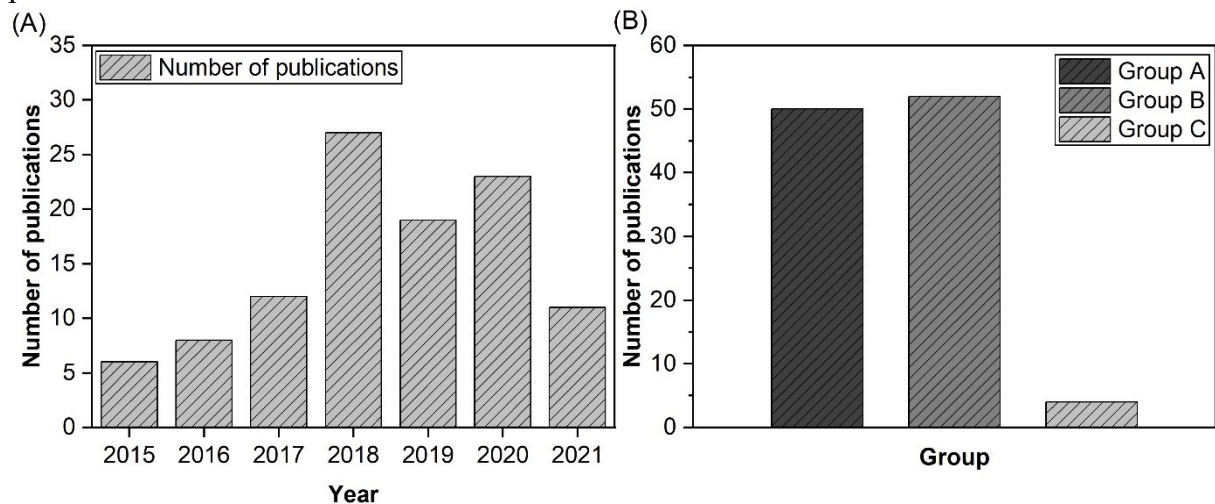
Source: elaborated by the author.

3 RESULTS

3.1 Literature search

The literature search identified 106 articles published between 2015 and 2021 shown in Figure 2A. An increase in publications was observed until 2018, as the total number of published articles varied significantly from 2018 to 2021. The works were divided into three groups Figure 2B. Group A (binary composites), Group B (non-binary composites), and Group C (works in a non-English language, without TiO₂, and reviews). The systematic review was based on articles from Group A, however, the large number of articles in Group B indicated a new trend in the scientific research.

Figure 2 – (A) The annual number of publications and (B) classification groups of the publications



Source: elaborated by the author.

3.2 Non-modified TiO₂ nanoparticles

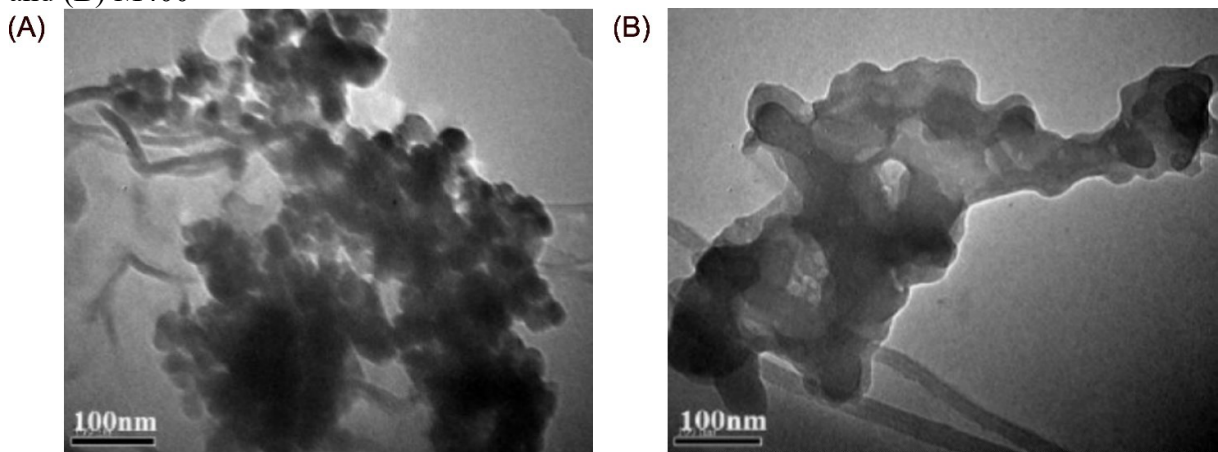
In this session, composites based on TiO₂ nanoparticles were organized from joining with doped and non-doped graphitic g-C₃N₄ nanosheets.

3.2.1 Non-doped g-C₃N₄ nanosheets

In a study developed by Ma, Wang, and He (2016), calcination was used to transform TiO₂ P25 and melamine into a composite formed by TiO₂ spherical particles and g-C₃N₄ 2D lamellar structure. The mechanical mixing of precursors generated a composite with

only parts of the TiO₂ nanoparticles embedded in the g-C₃N₄ structure (Figure 3A). However, agitation followed by calcination resulted in g-C₃N₄ being better distributed on the surface of the photocatalyst (Figure 3B). The composites produced with agitation exhibited higher photocatalytic activity compared to mechanically mixed, although their similar surface areas and the same g-C₃N₄ content (400 wt%).

Figure 3 – Transmission electron microscopy (TEM) images of composites (A) M0+g-C₃N₄ and (B) M400

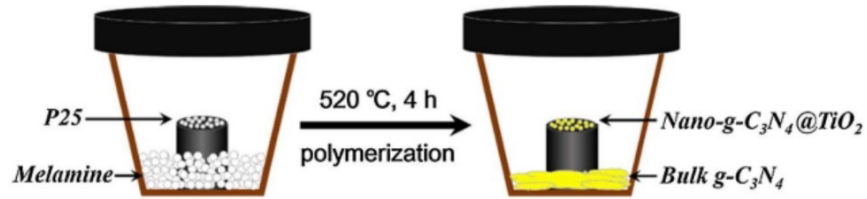


Source: adapted from Ma, Wang and He (2016).

Qu *et al.* (2016) studied the calcination temperature to synthesize a photocatalyst from tetrabutyl titanate and melamine. Temperatures below 400°C caused an increase of specific surface area, while temperatures above 400°C promoted the shrinkage of surface area. Melon structure was formed at low temperature due to the presence of TiO₂ during the melamine condensation. The dimerization of melamine forms melam and the rearrangement of melam and melamine produces melem, heat increasing the melem is transformed to melon (MISHRA *et al.*, 2019). The melon yielded a high surface area and small pore size to the photocatalyst prepared at 400°C. On the other hand, composites (2, 4, and 8% of melamine) produced by calcination at 600°C showed no activity under visible light (FAGAN *et al.*, 2016).

The vapor deposition method enabled the growth of g-C₃N₄ on the surfaces of the TiO₂ nanoparticles without contact with melamine during the calcination (TAN *et al.*, 2018b). The TiO₂ P25 nanoparticles were placed on top of the cylinder and melamine was inserted on the bottom of the crucible (Figure 4). The precursors of g-C₃N₄ sublimed during the heating process and condensed to form the tri-s-triazine structure (HUI *et al.*, 2021). This method yielded a photocatalyst (CN/TiO₂-24) with a specific surface area (67.1 m²/g) about 13 times higher than that of bulk-CN (6.1 m²/g).

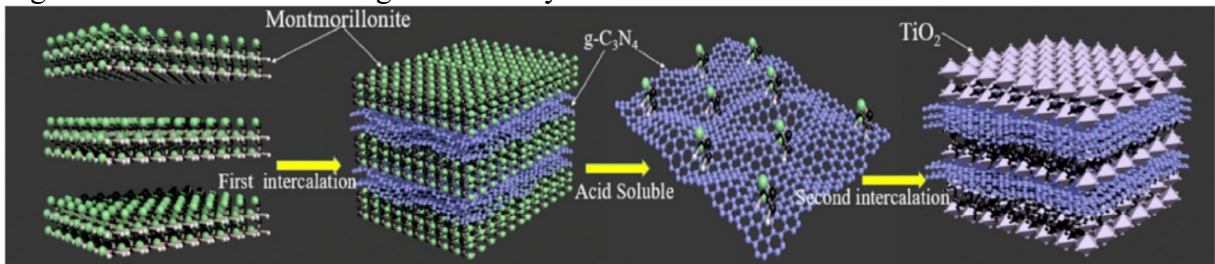
Figure 4 – Schematic illustration of the synthesis of $g\text{-C}_3\text{N}_4/\text{TiO}_2$ composite via vapor deposition



Source: adapted from Tan *et al.* (2018b).

In another experiment, montmorillonite was used as a template to create a multilayer in-line connection structure between the TiO_2 and $g\text{-C}_3\text{N}_4$ through intercalation method presented in Figure 5 (LI *et al.*, 2021). First, the spaces between the montmorillonite layers were filled with $g\text{-C}_3\text{N}_4$ obtained from urea. The second step involved acid leaching to remove the montmorillonite, as well as filling remaining spaces with TiO_2 . The researchers also studied the variation of the acid-dissolving time (6, 12, 18, and 24 h) in the synthesis of the composites.

Figure 5 – The schematic diagram of the synthetic route



Source: adapted from Li *et al.* (2021).

Shen *et al.* (2017) showed that the direct growth through thermal treatment was possible due to reactions during the synthesis process. Tetrabutyl titanate was reacted with deionized water to produce peroxotitanate, with the further addition of dicyandiamide to the peroxotitanate solution. This mixture was dried and calcined at 500°C , generating a porous structure of TiO_2 and $g\text{-C}_3\text{N}_4$. The decomposition of polyethylene glycol (PEG) and cetyl-trimethyl-ammonium bromide (CTAB) during calcination was responsible for the mesoporous structure with a large surface area (ZHANG *et al.*, 2014).

The hydrothermal method was used to construct a heterojunction from tetrabutyl titanate and melamine (JIA *et al.*, 2020). Initially, tetrabutyl titanate was transformed into MIL-125 (Ti) with the use of an organic-metal framework (MOF) as a model to acquire a porous structure. The porous TiO_2 ($196.5 \text{ m}^2/\text{g}$) had a great influence to the large specific surface area

(177.5 m²/g) of TCN8 photocatalyst when compared to the g-C₃N₄ (19.3 m²/g). This composite yielded better photocatalytic performance among composites with different concentrations of g-C₃N₄ (4, 8, and 15 wt%).

The solvothermal method was applied to fabricate g-C₃N₄/TiO₂ nanoporous heterostructure from tetrabutyl titanate (TBOT) and urea (TANG *et al.*, 2016). The researchers worked with TiO₂ spheres with irregular spindle-shaped embedded in the g-C₃N₄ structure. Enhanced photocatalytic activity was observed and thought to be related to the bandgap between g-C₃N₄ and TiO₂, larger BET surface area, and higher efficient separation of photogenerated electron-hole pairs.

Lv *et al.* (2019) developed an atomic layer deposition (ALD) based on individual cyclic and gas-solid deposition reactions to modify the surface. This technique was applied to construct a suitable interfacial structure in the TiO₂/g-C₃N₄ heterojunction. Each cycle of the process was constituted by four steps: pulsing TiCl₄, purging, pulsing H₂O, and purging again. In this composite, TiO₂ developed like a nano-island on the planar structure of g-C₃N₄ nanosheets. Table 1 presents some reaction conditions for the synthesis of TiO₂/g-C₃N₄ composites in different routes.

Table 1 – Synthetic methods of composites with non-modified TiO₂ nanoparticles and g-C₃N₄ nanosheets

(continue)					
Reference	Precursor	Mixing technique	Joining technique	Variable parameter	Surface area Bandgap
(MA; WANG; HE, 2016)	TiO ₂ P25 Melamine	Agitation for 30 min	<u>Calcination:</u> heat of covered crucible at 550°C (r = 15°C/min) for 4 h under air atmosphere	Melamine wt%: 0, 65, 300, 330, 400, 500 and 600	60.8 m ² /g
(TAN <i>et al.</i> , 2018b)	TiO ₂ P25 Melamine	-	<u>Vapor deposition:</u> heat of covered crucible at 520 °C (r = 15 °C/min) for 4 h	Melamine mass: 4, 8, 16, 24, 30 or 48 g	67.1 m ² /g 2.75 eV
(FAGAN <i>et al.</i> , 2016)	Titanium isopropoxide Melamine	Grind for 10 min	<u>Calcination:</u> heat at 600 °C (r = 5 °C/min) for 2 h in air	g-C ₃ N ₄ wt%: 2, 4 and 8	28.5-29.4 m ² /g 3.06-3.11 eV

Table 1 – Synthetic methods of composites with non-modified TiO₂ nanoparticles and g-C₃N₄ nanosheets

(conclusion)					
Reference	Precursor	Mixing technique	Joining technique	Variable parameter	Surface area Bandgap
(QU <i>et al.</i> , 2016)	Tetrabutyl titanate Melamine	Grinding	<u>Calcination:</u> heat for 2 h	Calcination temperature: 300, 400, 500, 600 and 700 °C	5.05-73.96 m ² /g 2.34-3.10 eV
(TANG <i>et al.</i> , 2016)	Tetrabutyl titanate (TBOT) Urea	Stirring	<u>Solvothermal-calcination:</u> autoclaved at 200°C for 24 h, centrifugation, wash, dry in vacuum at 60°C for 10 h and heat at 450°C for 2 h	g-C ₃ N ₄ wt%: 10, 20 and 30	176.5-240.3 m ² /g
(LV <i>et al.</i> , 2019)	Tetrabutyl titanate Dicyandiamide	-	<u>ALD deposition:</u> pulse and purge process at 200°C of Petri dish	Number of ALD cycles: 5, 10, 35 and 65	39.8-44.7 m ² /g 2.40 eV
(SHEN <i>et al.</i> , 2017)	Tetrabutyl titanate Dicyandiamide	Agitation	<u>Thermal treatment:</u> vacuum dry oven for 24 h, milling and calcination at 500°C (r = 0.5 °C/min) for 3 h	-	591.93 m ² /g 2.52 eV
(LI <i>et al.</i> , 2021)	Tetrabutyl titanate (TBTO) Urea	Ultrasonication for 1 h	<u>Hydrothermal:</u> autoclaved at 180°C for 12 h, cooled, washed and dried at 60°C for 12 h	Leaching time: 6, 12, 18 and 20 h	172.9 m ² /g 2.44-2.65 eV
(JIA <i>et al.</i> , 2020)	Tetrabutyl titanate Melamine	Grinding for 5 min	<u>Calcination:</u> heat at 500 °C (r = 5 °C/min) for 120 min	g-C ₃ N ₄ wt%: 4, 8 and 15	117.3 m ² /g 3.13-2.62 eV

Source: elaborated by the author.

3.2.2 Doped g-C₃N₄ nanosheets

Li *et al.* (2016) synthesized phosphorus-doped g-C₃N₄ nanosheets coated with TiO₂ nanoparticles square flake by solvent-thermal method to improve the photocatalytic activity under visible light. The doping of nanosheets from melamine and phosphonitrilic chloride trimer (Cl₆N₃P₃) resulted in the replacement of nitrogen atoms by phosphorus in the g-C₃N₄ lattice. A large area was obtained in the doped g-C₃N₄ than in pristine g-C₃N₄ because the surface and edges of the stacked lamellar structure became rougher. The reduction of charge separation efficiency in composite with the high phosphorous content indicated that the dopant could act as recombination centers of electrons and holes.

The *in-situ* method was applied to fabricate a photocatalyst with carbon-doped supramolecule-based g-C₃N₄ (BCCN) layers and TiO₂ nanoparticles (HU *et al.*, 2019). BCCN structure presented stacked nanosheets with smooth surfaces and mesopores. The porous structure formation of BCCN was possible due to the partial decomposition of the cyanuric acid into gas under elevated temperatures (ZHOU *et al.*, 2018). Composite with a 30% of BCCN showed the integration between nanosheets and some nanoparticles, indicating that BCCN was a stable substrate for loading TiO₂. In the study of photocatalytic activity, the composite 40% BCCNT had a lower performance compared to 30% BCCNT. The excess of BCCN may act as recombination centers and hinder the light absorption (ZHOU *et al.*, 2018).

In another study, recrystallization-annealing strategy was used to fabricate a composite with alkalinized g-C₃N₄ and TiO₂ (LIU *et al.*, 2019). The sodium bicarbonate (NaHCO₃) was dissociated and incorporated into g-C₃N₄ during heat treatment, producing pores in the g-C₃N₄ when NaHCO₃ decomposed. Sodium doping not only increased the composite surface area from 50.8 to 56.4 m²/g, but the zeta potential also changed from -26.0 to -68.8 mV. In addition, during the thermal treatment, the bonds between carbon and nitrogen were replaced by carbon and hydroxyl.

Hao *et al.* (2017b) produced a composite of TiO₂ and g-C₃N₄ from the hydrothermal reaction between titanium tetrachloride (TiCl₄) and melamine. The hydrolysis of TiCl₄ generated hydrochloric acid (HCl), which was used as a proton source to acidify melamine. The protonation of amino groups of melamine and the modification in the thermal condensation mode of melamine resulted in the formation of more abundant mesoporous. The researchers observed that the ratio of melamine/TiCl₄ in the synthesis played a crucial role in determining composite specific surface area.

The information about synthetic methods above is listed in Table 2.

Table 2 – Synthetic methods of composites with non-modified TiO₂ nanoparticles and g-C₃N₄ doped nanosheets

Reference	Precursor	Mixing technique	Joining technique	Variable parameter	Surface area Bandgap
(LI <i>et al.</i> , 2016b)	Tetrabutyl titanate Melamine	Ultrasonication	<u>Solvent-thermal</u> : autoclave at 180 °C for 12 h, wash and dry at 80°C for 2 h	Cl ₆ N ₃ P ₃ mass: 0.01, 0.03 and 0.05 g	2.85-2.94 eV
(HU <i>et al.</i> , 2019)	Tetrabutyl titanate Melamine Cyanuric acid	Sonification for 30 min and stirring for 24 h	<u>Dry</u> : dry at 60°C for 12 h	BCCN mass ratio: 10, 20, 30, and 40%	-
(LIU <i>et al.</i> , 2019)	TiO ₂ Urea	Sonification and crystallization in an oil bath at 100°C	<u>Recrystallization-annealing</u> : grind and calcination at 550°C for 2 h (r = 3°C/min)	-	56.4 m ² /g 2.79 eV
(HAO <i>et al.</i> , 2017b)	Titanium tetrachloride Melamine	Agitation for 30 min and agitation for 2 h	<u>Hydrothermal-calcination</u> : autoclave at 180°C for 4 h, dry at 100°C for 10 h and heat at 550°C (r = 5°C/min) for 2 h under air atmosphere	Melamine mass: 0.5, 1, 2, 3 and 4 g	32.1-115.6 m ² /g 2.97 eV

Source: elaborated by the author.

3.3 Modified TiO₂ nanoparticles

Synthetic methods can produce titanium dioxide (TiO₂) nanoparticles structurally modified by doping. In this session, composites based on doped TiO₂ nanoparticles were divided according to coupling with non-doped and doped g-C₃N₄ nanosheets.

3.3.1 Non-doped g-C₃N₄ nanosheets

A chemical tailoring method was used to fabricate porous g-C₃N₄ nanosheets (CNs) supported with TiO₂ nanoparticles doped with nitrogen (N) and sulfur (S) (OUYANG *et al.*, 2021). The sodium hydroxide (NaOH) acted as a hole-making agent and chemical tailor by removing the aluminum oxide (Al₂O₃) nanoparticles embedded in the g-C₃N₄ structure. This

synthesis used the lactic acid (LA) as linker and inducer, resulting in an uniform distribution of nanoparticles on the surface of porous g-C₃N₄ nanofilms and in an increase of specific surface area.

Hossain *et al.* (2021) synthesized a novel heterojunction that used sludge-generated titania (S-TiO₂) as the precursor of TiO₂ and melamine. From the sludge generated in the Ti-based flocculation, S-TiO₂ was retrieved to form a composite with melamine via calcination. Successful heterojunction formation reduced bandgap energy, contributing to superior photoactivity of the composite produced by mixing ratio of 1:3 to S-TiO₂ and melamine (STC4). Synthesis showed a significant potential for the utilization of unwanted sludge from water treatment plants, promoting sustainability and reducing the synthesis cost of photocatalysts.

A calcination approach with urea and tetrabutyl titanate was used to fabricate composite of carbon (C) doped TiO₂ with g-C₃N₄ (WU *et al.*, 2016). The C-TiO₂ and g-C₃N₄/C-TiO₂-2 photocatalysts exhibited a wide and strong light absorption in the whole UV and visible range of 200-800 nm, suggesting that both modifications could greatly improve optical absorption properties. The authors associated the good photoactivity of g-C₃N₄/C-TiO₂-2 composite with mesoporous structure and larger surface area.

Kong *et al.* (2018) fabricated Z-scheme heterojunction composed by the g-C₃N₄ crumpled sheet and Ti³⁺ doped TiO₂ nanoparticles via polycondensation of urea with TiO₂ and hydrogenated treatment. Thermal treatment in hydrogen (H₂) atmosphere has been a recognized strategy to introduce self-doped defects, extending the light absorption range of TiO₂ (CUSHING *et al.*, 2017). The electrons of the H atoms were transferred to the Ti⁴⁺ of TiO₂ to form Ti³⁺ defects (PAN *et al.*, 2013). This treatment conferred Ti³⁺ defect states below the conduction band minimum (CBM) of TiO₂ and improved visible light absorption of the composite.

One-step heating was used to form a composite with Ti³⁺ self-doped TiO₂ and g-C₃N₄ prepared from H₂Ti₃O₇ nanotubes and melamine (LI *et al.*, 2015b). Ultrasonic treatment provided full coverage of surface H₂Ti₃O₇ nanotubes by melamine due to the formation of hydrogen bonds. The self-collapse process of H₂Ti₃O₇ nanotubes, as well as the generation of reducing gas in the decomposition of melamine, contributed to the transformation of nanotubes into nanoparticles. Oxygen vacancies were produced in the nanotubes under anoxic decomposition conditions in thermal treatment, forming Ti³⁺ self-doped TiO₂.

A synthesis of composite with 2D porous g-C₃N₄ and nitrogen (N) doped TiO₂ P25 by *in situ* and facile annealing strategy was developed to enhance the quantum effect (DING *et*

al., 2015). Doped TiO₂ P25 acted in the formation of a porous structure with reduced thickness of g-C₃N₄, providing a high specific surface area and enhanced charges separation when compared to the g-C₃N₄ bulk. Some surface defects can arise in g-C₃N₄ and act as trappers to the electrons or holes on the surface, increasing the separation time of photogenerated pairs.

Jiang *et al.* (2018) used a facile three-step approach to synthesize a heterojunction constituted of nitrogen (N) doped TiO₂ and g-C₃N₄. These components were prepared separately to coupling by solution-mediated method and calcination. Uniform assembly of nanoparticles on the g-C₃N₄ layers was achieved in the first process, and the relatively low temperature used (450°C) intensified the interface interaction between semiconductors during the calcination. Nitrogen doping extended absorption spectra in the visible region due to narrowed bandgap from 3.2 eV (pristine TiO₂) to 2.84 eV (N-TiO₂).

A sol-gel-assisted low-temperature calcination method was developed for the homogeneous growth of doped TiO₂ nanoparticles over g-C₃N₄ (MOHAMED *et al.*, 2018a). The urea was used as a source of nitrogen and phosphorous during the TiO₂ structure formation and, at the same time, thermal condensation occurred transforming urea into the polymeric g-C₃N₄. The polarity of urea molecules allows movement, rotation, and freely vibration when they are dissolved in the water. This contributed to establish a good interaction between precursors during the hydrolysis-polymerization of TiO₂ in an aqueous urea solution. The heating and calcination at 400°C induced the transition of the amorphous TiO₂ doped with carbon (C) and nitrogen (N) co-doped into crystalline form, contributing to the formation of the composite.

The parameters involved on the synthesis above are summarized in Table 3.

Table 3 – Synthetics methods of composites with modified TiO₂ nanoparticles and g-C₃N₄ nanosheets

(continue)					
Reference	Precursor	Mixing technique	Joining technique	Variable parameter	Surface area Bandgap
(OUYANG <i>et al.</i> , 2021)	Titanium disulfate Melamine	Agitation for 30 min	<u>Calcination:</u> heat at 450 °C for 1 h (r = 2°C/min)	CNs mass: 40, 80 and 120 mg	73.36 m ² /g 2.76 eV
(HOSSAIN <i>et al.</i> , 2021)	TiCl ₄ Melamine	-	<u>Calcination:</u> heat at 550 °C (r =10°/min) under atmospheric pressure for 3 h	S-TiO ₂ / melamine weight ratio: 2:1, 1:1, 1:2, 1:3, 1:4 and 1:5	30.40- 52.33 m ² /g 2.65 eV

Table 3 – Synthetics methods of composites with modified TiO₂ nanoparticles and g-C₃N₄ nanosheets

Reference	Precursor	Mixing technique	Joining technique	Variable parameter	Surface area Bandgap
(WU <i>et al.</i> , 2016)	Tetrabutyl titanate Urea	Grinding	<u>Calcination:</u> heat under N ₂ atmosphere at 350 °C (r = 1°C/min) for 4 h and heat at 600 °C (r = 5 °C/min) for 1 h	Membrane powder/urea mass ratio: 1:0.8, 1.0:1.0 and 1.2:1.0	212-248 m ² /g
(LI <i>et al.</i> , 2015b)	Commercial TiO ₂ Melamine	Ultrasonication for 30 min, stirring for 4 h and centrifugation	<u>Calcination:</u> heat of crucible an at 520 °C for 4h	Melamine/H ₂ Ti ₃ O ₇ nanotubes ratio weight: 4, 8, 6 and 32	-
(KONG <i>et al.</i> , 2018)	Anatase TiO ₂ Urea	-	<u>Calcination-hydrogenation:</u> heat at 500°C for 4 min and at 350° for 30 min in H ₂ /air atmosphere	-	63 m ² /g 2.8 eV
(DING <i>et al.</i> , 2015)	TiO ₂ P25 Urea	Grinding	<u>Calcination:</u> heat of a covered crucible at 520 °C (r = 25 °C/min) for 4 h	P25/urea mass ratio: 1:4, 1:8 and 1:10	-
(JIANG <i>et al.</i> , 2018)	Titanium nitride Urea	Sonication	<u>Calcination:</u> heat at 450 °C for 2 h	N-TiO ₂ mass: 15, 20, 25, 30 and 35 mg	-
(MOHAM ED <i>et al.</i> , 2018a)	Titanium butoxide Urea	Stirring for 30 min	<u>Sol-gel-calcination:</u> crystallization at 80°C, grind and heat at 400 °C (r = 5°C/min) for 4 h	-	51.13 m ² /g 2.45 eV

Source: elaborated by the author.

3.3.2 Doped g-C₃N₄ nanosheets

The hydrothermal treatment was applied to transform melamine and titanium oxohydride sol precursor into Ti³⁺-TiO₂/O-g-C₃N₄ photocatalyst (LI *et al.*, 2017a). This

heterojunction was constituted by TiO₂ nanoparticles doped with Ti³⁺ and g-C₃N₄ nanosheets doped with oxygen (O). Titanium oxohydride was obtained from the incomplete reaction of titanium hydride (TiH₂) and hydrogen peroxide (H₂O₂). The ultrasonic treatment allowed the penetration of TiH₂ into the layer interspaces of g-C₃N₄. The oxygen vacancies (Ov) were detected after the synthesis because they could be formed around the Ti³⁺ to satisfy the requirement of charge equilibrium (SU *et al.*, 2013). These modifications caused the improvement of electronic conductivity and extension of the light absorption range to the visible-light region.

A facile method to manufacture nanocomposite films formed by protonated g-C₃N₄ (pCN) and Ti³⁺ self-doped TiO₂ under ambient temperature was used by Huang *et al.* (2019). TiO₂ sol and pCN solution were prepared separately before being mixed to coat the glasses. The TiO₂ contributed significantly to the immobilization of pCN because it was used as chemical glue. During the sol-gel method, titanium alkoxides aqueous medium were converted into ultra-fine TiO₂ nanocrystals by hydrolysis and condensation reactions at low temperature (<100°C) (LI; WHITE; LIM, 2004). Additionally, the protonation of g-C₃N₄ contributed by providing a better dispersion, high surface, adjustment of electronic band gaps, and improved charge separation efficiency (ZHANG *et al.*, 2009).

A TCN70 photocatalyst was prepared by hydrothermal process and calcination using the hydroxylated g-C₃N₄ (CN-OH) and the oxygen-vacant TiO₂ (Ov-TiO₂) (MA *et al.*, 2021). The construction of composite aimed to facilitate the separation of photogenerated carriers and to enhance photocatalytic efficiency. The success of the synthesis occurred due to the synergic effect between CN-OH and Ov-TiO₂ from a self-built electric field (E) at the interface between CN-OH and Ov-TiO₂.

Table 4 presents the parameters of synthetic methods related.

Table 4 – Synthetics methods of composites with modified TiO₂ nanoparticles and g-C₃N₄ doped nanosheets

(continue)					
Reference	Precursor	Mixing technique	Joining technique	Variable parameter	Surface area Bandgap
(LI <i>et al.</i> , 2017a)	Titanium hydride Melamine	Ultrasonication for 20 min	<u>Hydrothermal</u> : autoclave, heat at 160°C for 27 h, wash and dry at 60°C for 3 h	Ti ³⁺ -TiO ₂ /O-g-C ₃ N ₄ mass ratio: 1:1, 1:2, 1:4 and 1:8	-

Table 4 – Synthetics methods of composites with modified TiO₂ nanoparticles and g-C₃N₄ doped nanosheets

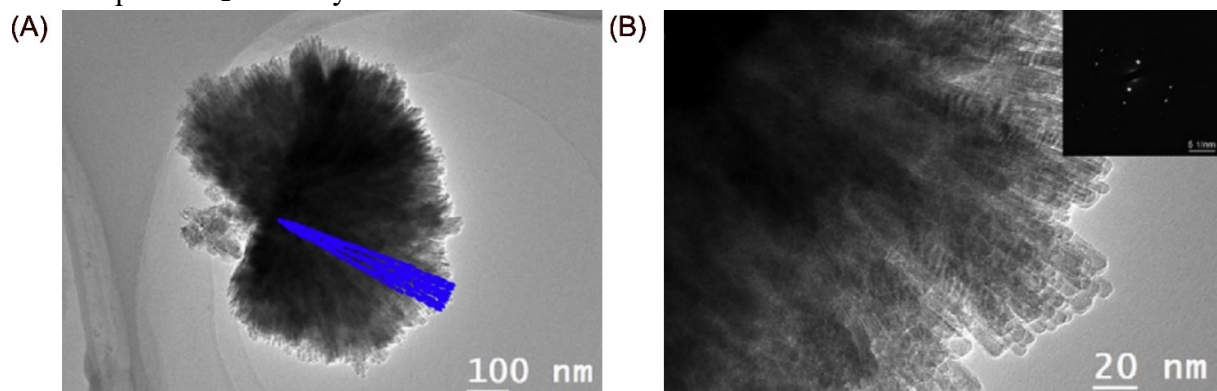
Reference	Precursor	Mixing technique	Joining technique	Variable parameter	(conclusion)
					Surface area Bandgap
(HUANG <i>et al.</i> , 2019)	Tetrabutyl titanate Melamine	Ultrasonication for 5 times	-	pCN mass ratio: 0.66, 1.32, 3.23 and 6.25%	-
(MA <i>et al.</i> , 2021)	Isopropyl titanate Melamine	Sonication for 30 min and dry at 70°C for 12 h	<u>Calcination:</u> heat at 450°C for 2 h (r = 2°Cmin ⁻¹) in atmosphere air	CN-OH weight ratio: 10, 30, 50, 70 and 90%	-

Source: elaborated by the author.

3.4 TiO₂ mesocrystals

A facile solvothermal method was applied to form direct Z-scheme Ti³⁺ doped Meso-TiO₂/g-C₃N₄ (YU *et al.*, 2018). In this process, acetone molecules were absorbed by TiO₂ nanoparticles, reducing partially the Ti⁴⁺ species into Ti³⁺ species and oxygen vacancies (YU *et al.*, 2017). An urchin-like shape composed of grown-up and organized TiO₂ nanoparticles with fixed crystallographic orientation was formed (Figure 6A and 6B). The researchers associated the enhanced lifetime of charge carriers and formation of new chemical bonds with improved light absorption and photocatalytic activity of material.

Figure 6 – (A) Image of transmission electron microscopy (TEM) and (B) magnified image of Ti³⁺ doped TiO₂ mesocrystals



Source: adapted from Yu *et al.* (2018).

The g-C₃N₄ nanosheets were used as the substrate to guide the heterogeneous growth of defective anatase TiO_{2-x} mesocrystals (TAN *et al.*, 2018a). The g-C₃N₄ nanosheets acted as stable supporting materials for anchoring spindle-shaped particles even after

sonification. Since the amino groups (N-H) of g-C₃N₄ acted as the heterogeneous nucleation sites, anchor of TiO₂ nanoparticles contributed to avoiding the agglomeration. During the calcination, an abstraction of oxygen atoms from the crystal lattice of TiO₂ yielded large quantities of oxygen vacancies.

A g-C₃N₄ NS/TMC composite formed by TiO₂ mesocrystals (TMC) and g-C₃N₄ nanosheets (g-C₃N₄ NS) was produced by calcination (ELBANNA; FUJITSUKA; MAJIMA, 2017). Ultrasonic treatment transformed crumpled sheet-like morphology with many stacking layers into thin nanosheets with a few hundred nanometers. In this material, monocrystals acted as electron transfer channel to promote charge separation. The composite synthesized with 31 wt% of g-C₃N₄ and P25 showed a similar surface area to the composite with TMC, but it obtained a photocatalytic activity 7 times lower.

The methods mentioned above are shown in Table 5.

Table 5 – Synthetic methods of composites with TiO₂ mesocrystals and g-C₃N₄ nanosheets

Reference	Precursor	Mixing technique	Joining technique	Variable parameter	Surface area Bandgap
(YU <i>et al.</i> , 2018)	Titanium tetrachloride Melamine	Ultrasonicati on for 15 min	<u>Solvothermal method</u> : autoclave at 60°C	g-C ₃ N ₄ /TiO ₂ mass ratio: 1:9, 1:3, 1:1, 3:1 and 9:1	238.29 m ² /g
(TAN <i>et al.</i> , 2018a)	Titanium (III) chloride Urea	Stirring for 10 min	<u>Solvothermal treatment-calcination</u> : autoclave at 150 °C for 5 h, dry at 60°C and heat at 400°C for 1 h in air	g-C ₃ N ₄ wt%: 0, 20, 25, 33.3 and 40	165 m ² /g
(ELBANNA; FUJITSUKA; MAJIMA, 2017)	Titanium (IV) fluoride Melamine	Ultrasonicati on for 30 min and stirring for 24 h and dry	<u>Calcination</u> : heat at 400° C for 2 h in an air atmosphere	g-C ₃ N ₄ wt%: 11, 20, 31, 41 and 63	557.4 m ² /g 22.79 eV

Source: elaborated by the author.

3.5 TiO₂ quantum dots

In-situ pyrolysis of NH₂-MIL-125 (Ti) and melamine was used to fabricate a 0D/2D heterostructure composed by oxygen vacancy-rich TiO₂ quantum dots confined in the g-C₃N₄

nanosheets (SHI *et al.*, 2019). The construction of composite aimed to separate photogenerated charge carriers efficiently by building the interface. The mesopores and macropores of the structure were developed due to the release of a large amount of gas (NH_3 and CO_2) during the pyrolysis process.

On the other hand, the photocatalyst constituted by TiO_2 quantum dot doped with fluorine (F- TiO_2 QDs) and g- C_3N_4 nanosheet was synthesized via solvothermal treatment (WANG *et al.*, 2021). The hydrofluoric acid used played a role in the F- TiO_2 QDs distribution on the surface of g- C_3N_4 , causing the delay in the hydrolysis of Ti precursor, improving visible light capture, and aiding the formation of covalent bonds between semiconductors. The TiO_2 quantum dots provided more active sites and enhanced the light-harvesting, while C-O covalent bond established in the interface afforded an effective pathway for charge transfer and selective recombination.

These synthesis processes are shown in Table 6.

Table 6 – Preparation methods of composites formed by TiO_2 quantum dots and g- C_3N_4 nanosheets

Reference	Precursor	Mixing technique	Joining technique	Variable parameter	Surface area Bandgap
(SHI <i>et al.</i> , 2019)	Titanium (IV) Isopropoxide Melamine	-	<u>Calcination:</u> heat of covered crucible at 550°C ($r = 5^\circ\text{C}/\text{min}$) for 2 h, milled and heat of uncovered crucible at 450°C for 2 h	Melamine/ NH_2 -MIL-125 mass ratio: 5:0.05, 5:0.1, 5:0.15 and 5:0.4	19.8-134.4 m^2/g 2.34-2.44 eV
(WANG <i>et al.</i> , 2021)	Titanium butoxide Dicyandiamide	Stirring for 30 min	<u>Solvothermal:</u> Autoclave at 180°C for 24 h, spin, wash and dry at 60°C overnight	TBOT mass: 1.08, 0.54 and 0.27 g	116.3 m^2/g 2.58 eV

Source: elaborated by the author.

3.6 TiO_2 nanosheets

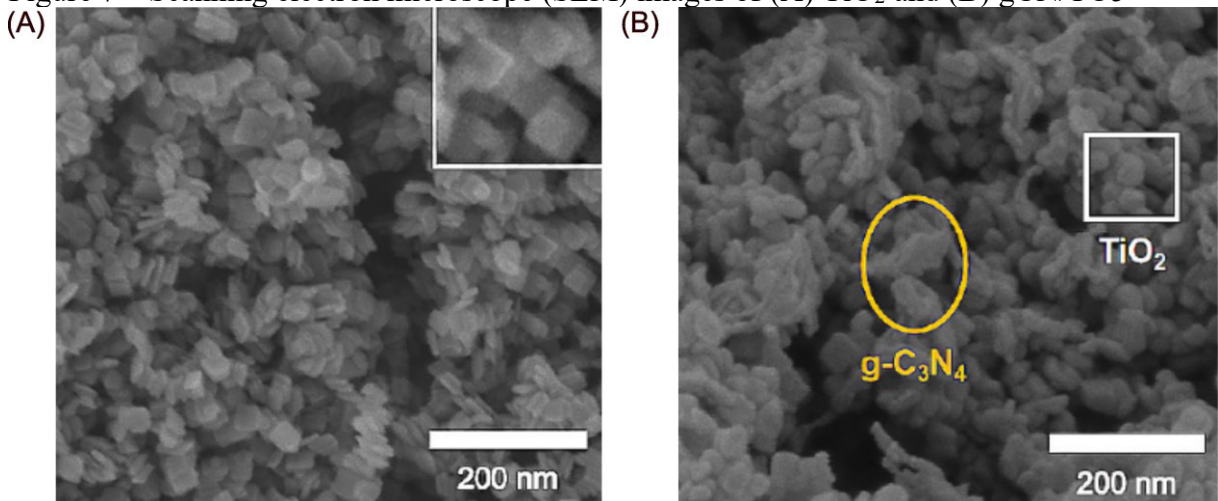
3.6.1 Non-doped g- C_3N_4 nanosheets

A solvothermal method was applied in the synthesis of nanosheet TiO_2 coupled

tightly with g-C₃N₄ nanosheet from tetrabutyl titanate and melamine (JIANG *et al.*, 2017). As result, it formed interfacial covalent Ti-O-N bonds favoring electrostatic interactions to promote electron transfer and to suppress charge recombination. The interfacial interaction between components in the composite can make the photocatalytic reaction more efficient than the heterojunction fabricated by physical mixture.

The vapor deposition method, recognized by its robustness, convenience, and effectiveness was applied to couple the g-C₃N₄ and TiO₂ nanosquare (LV *et al.*, 2020). The square TiO₂ sheets synthesized from hydrothermal synthesis presented a block-like structure composed of a flat-lying square sheets structure of TiO₂ (Figure 7A). The melamine vapor phase sublimation contributed to g-C₃N₄ deposition on the TiO₂ nanocrystal, forming the composite through calcination (Figure 7B). This method enabled a close contact and high-quality interface to benefit electrons transfer and photocatalytic performance.

Figure 7 – Scanning electron microscope (SEM) images of (A) TiO₂ and (B) gCN/TO5



Source: adapted from Lv *et al.* (2020)).

The self-assembly method TiO₂/g-C₃N₄ 2D/2D nanocomposites were successfully synthesized by calcination from tetrabutyl titanate and dicyandiamide (YANG *et al.*, 2019). The composite presented TiO₂ nanosheets (TNs) horizontally loaded on the g-C₃N₄ nanosheets (CNs) with close interfacial contact, increasing the contact area effectively. Besides efficient separation of the photoexcited electron and hole, the suitable band positions contributed to photocatalytic activity.

The information about synthetic methods is in Table 7.

Table 7 – Synthetic methods of composites with TiO₂ nanosheets and g-C₃N₄ nanosheets

Reference	Precursor	Mixing technique	Joining technique	Variable parameter	Surface area Bandgap
(JIANG <i>et al.</i> , 2017)	Tetrabutyl titanate Melamine	-	<u>Solvothermal:</u> autoclavation at 180°C for 12 h	TiO ₂ /g-C ₃ N ₄ mass ratio: 1:1, 1.5:1, 4:1, 6:1, 8:1, 10:1, 12:1 and 14:1	62.33-75.19 m ² /g
(YANG <i>et al.</i> , 2019)	Tetrabutyl titanate Dicyandiamide	Agitation for 12 h	<u>Calcination:</u> heat at 400°C for 4 h	TiO ₂ wt%: 5, 10, 15, 20 and 25	29.33 m ² /g
(LV <i>et al.</i> , 2020)	Tetrabutyl titanate Melamine	-	<u>Vapor deposition:</u> heat at 520°C (r = 10°C/min) for 4 h	Melamine mass: 0.5, 10, 15 and 20 g	2.8-2.9 eV

Source: elaborated by the author.

3.6.2 Doped g-C₃N₄ nanosheets

Zhang and coworkers proposed wet-chemistry self-assemble approach to synthesize 2D-2D TiO₂/g-C₃N₄ heterojunctions (ZHANG *et al.*, 2020). Nitride carbon graphitic (g-C₃N₄) was produced from a cyanuric acid–melamine supramolecular precursor. The hydrogen-bonded formed between cyanuric acid and melamine contributed to improvement of carbon nitride synthesis (SHALOM *et al.*, 2013). The pretreatment with acid or alkali of ultrathin 2D-TiO₂ nanosheets and g-C₃N₄ nanosheets into aqueous solvents promoted the adsorption between materials by tailored surface electrostatic force. The in-situ growth allowed the formation of strong chemical bonds between the nanosheets during the self-assembly compared to weak contact heterostructures formed by the physical mixture.

Solvothermal treatment, co-calcination, and surface charged-induced heteroaggregation were used to produce composites based on TiO₂ and g-C₃N₄ (ZHONG *et al.*, 2019). The modification of g-C₃N₄ by solvothermal method and acid treatment generated O-CN and H-CN bonds. As TiO₂ nanosheets were fabricated *in situ* by P123 template-assisted self-assembly, the residual P123 can interfere with the charge and mass transference of the photocatalytic process. The physically mixed composite produced weak Van der Waals interaction which did not accelerate photocatalysis, while Ti-O-N covalent linkages were formed between semiconductors from the hydrothermal method (GU *et al.*, 2017). However, the charge-induced aggregated sample did not inhibit electron-hole recombination through

electrostatic interaction.

These synthetic methods are systematized in Table 8.

Table 8 – Synthetic methods of composites with TiO₂ nanosheets and g-C₃N₄ doped nanosheets

Reference	Precursor	Mixing technique	Joining technique	Variable parameter	Surface area Bandgap
(ZHANG <i>et al.</i> , 2020)	Titanium (IV) isopropoxide Melamine	Ultrasonication for 60 min	<u>Hydrothermal-calcination</u> : autoclave and heat at 300°C for 1 h	g-C ₃ N ₄ mass: 5, 10, 50 and 100 mg	43.4-385.6 m ² /g 2.75 eV
(ZHONG <i>et al.</i> , 2019)	Titanium isopropoxide Melamine	Ultrasonication for 30 min Ultrasonicated in the ice bath for 2 h	<u>Solvothermal</u> : autoclave at 150° for 20 hours, wash and dry 60°C overnight <u>Co-calcination</u> : dry at 60°C overnight and calcination at 450°C for 2 h (r = 10°C/min) <u>Charge-induced aggregation</u> : centrifuge and dry at 60 °C overnight	Synthetic methods	73-263 m ² /g 2.44-2.54

Source: elaborated by the author.

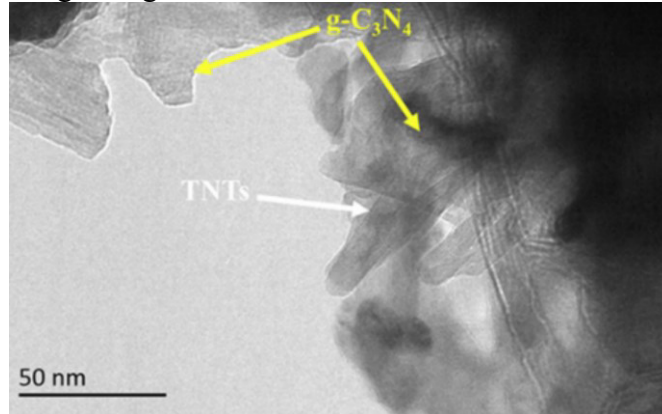
3.7 TiO₂ nanotubes

The g-C₃N₄/TNTs heterostructures were prepared by *in situ* growth of graphitic carbon nitride (g-C₃N₄) from urea on the surface of TiO₂ nanotube arrays (TNTs) (SIM *et al.*, 2020). The composite prepared with 1.5 g of urea reduced the band energy to 1.8 eV due to the impurity energy level induced by g-C₃N₄. This coupling of materials reduced the recombination of photogenerated electron-hole pairs. The researchers reported that the increase in urea content (1.5-2.0 g) caused aggregation of g-C₃N₄, reducing interfacial adhesion between materials.

Ji *et al.* (2020) optimized a method based on hydrothermal reaction and calcination to synthesize photocatalysts. This method transformed titanate into material with proportions of anatase and rutile similar to the P25, forming “hot spots” at rutile-anatase-titanate interfaces. These structures acted in conjunction with transition points in the interface, leading to the

efficient and rapid electron transfer from rutile to anatase as a result of bandgap and phases proportion (OHTANI, 2010). The structure of the composite was constituted by g-C₃N₄ 2D sheets and TiO₂ nanotubes (Figure 8). The photocatalyst structure design was executed by fine controlling of precursors ratio and calcination temperature.

Figure 8 – Transmission electron microscopy (TEM) images of g-C₃N₄/TNTs-2



Source: adapted from Ji *et al.* (2020).

In other experiment, the thermal condensation polymerization was used to form the phosphorus-doped carbon nitride quantum dots (CNPQDs) deposited on the surface of the nanotube arrays formed by circular anatase (TNA) as well as on the nanotubes of square-shaped rutile (STNA) (KUMAR *et al.*, 2020). Urea and citric acid reacted via condensation polymerization to generate the basic carbon nitride framework, while 1-n-butyl-3-methylimidazolium hexafluorophosphate (BMIM-PF6) served as the source of phosphorus doping. Annealing transformed the morphology of the cylindrical nanotubes into square-shaped nanotubes (STNA). This material obtained a higher density of the “hot spots”, contributing to enhanced light-harvesting of the CNPQD-STNAs photocatalyst.

The methods mentioned above are summarized in Table 9.

Table 9 – Synthetic methods of composites with TiO₂ nanotubes and g-C₃N₄ nanosheets

(continue)

Reference	Precursor	Mixing technique	Joining technique	Variable parameter	Surface area Bandgap
(SIM <i>et al.</i> , 2020)	Titanium (Ti) foil Urea	Immersion in the aqueous solution for 24 h	<u>Calcination</u> : heat at 550°C for 3 h	Urea mass: 1, 1.5 and 2 g	1.8 eV

Table 9 – Synthetic methods of composites with TiO₂ nanotubes and g-C₃N₄ nanosheets

Reference	Precursor	Mixing technique	Joining technique	Variable parameter	Surface area Bandgap
(JI <i>et al.</i> , 2020)	P25 TiO ₂ Melamine	Stir for 1 h, sonification for 2 h and dry at 105°C for 24 h	<u>Calcination:</u> grind and heat at 500°C for 2 h	g-C ₃ N ₄ mass: 0.3, 0.6, 0.9 and 1.5 g	63.4 m ² /g 3.44 eV
(KUMAR <i>et al.</i> , 2020)	Ti foil Urea	-	<u>Hydrothermal:</u> autoclave at 120 °C for 12 h, cool, wash and dry at 60 °C	-	-

Source: elaborated by the author

3.8 TiO₂ nanofibers, nanowires and nanobelts

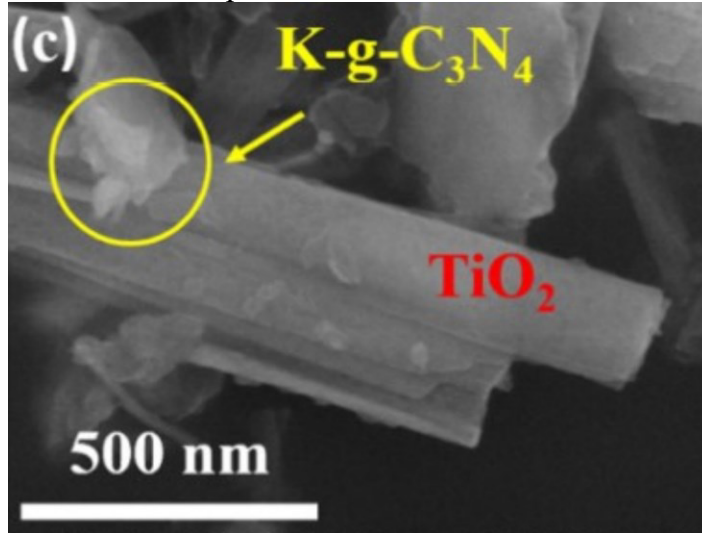
Composites were formed by Na₂Ti₃O₇ ultralong nanotubes hydrolyzed in the presence of g-C₃N₄ to promote a structural transformation (SUN *et al.*, 2018). Probably, the structural change occurred during the hydrothermal treatment, favoring the growth of TiO₂ nanoparticles from the crumble of Na₂Ti₃O₇ nanotubes. This process produced heterojunctions constituted by rice spike-like g-C₃N₄/TiO₂ nanowires. Extension to visible light response occurred by effects of the interface coordination between materials and production of Ti³⁺ after hydrothermal treatment.

TiO₂ nanofibers (HBTiO₂) were fabricated by electrospinning followed by an alkali-hydrothermal process (NASIR *et al.*, 2020). The synthesis process by vapor deposition resulted in heterojunction with small particles of g-C₃N₄ deposited uniformly on the surface of the nanowires. The quantum dots (QDs) in the interstitial spaces of HBTiO₂ formed a flat surface, reducing the surface area from 205.5 to 92.4 m²/g (LI *et al.*, 2017b). The introduction of QDs on the semiconductor surface narrowed the bandgap energy and facilitated electrons transport under visible light.

A hydrothermal method followed by calcination was applied to fabricate composite with K-doped graphitic carbon nitride (g-C₃N₄) and TiO₂ nanobelts (MA *et al.*, 2018a). Doping with potassium (K) narrowed the bandgap from 2.70 to 2.55 eV and improved charge transfer in layers by chemical bonds between potassium (K) atoms with carbon (C) and nitrogen (N) atoms of g-C₃N₄. The researchers concluded that crystallinity and surface area were not the

main factors responsible for the composite photocatalytic activity. Figure 9 shows several particles of TCN-K5 composite deposited on the surface of TiO₂ nanobelts.

Figure 9 – Scanning electron microscope (SEM) image of TCN-K5 sample



Source: adapted from Ma *et al.* (2018a).

Fiber surface of TiO₂ doped with cobalt (Co²⁺) fabricated by electrospinning and calcination was used as support to in-situ growth of g-C₃N₄ quantum shell (SONG *et al.*, 2020). The thickness and loading amount of the g-C₃N₄ nanoshell could be precisely controlled by the regulation of melamine content. The addition of Co²⁺ prevented the structural collapse of fibrous membranes in the post-treatment process, and the absorption edge was extended from ultraviolet to visible (NGHIA; NEGISHI; HUE, 2018). Photocatalytic performance was attributed not only to 3D porous networks and match of energy bands, but also to uniformity of g-C₃N₄ onto Co-TiO₂ fibers and close contact interface.

The related synthetic processes are organized in Table 10.

Table 10 – Synthetic methods of composites with TiO₂ nanofibers, nanowires and nanobelts and g-C₃N₄ nanosheets

(continue)					
Reference	Precursor	Mixing technique	Joining technique	Variable parameter	Surface area Bandgap
(NASIR <i>et al.</i> , 2020)	Tetrabutyl titanate Melamine	-	Vapor deposition: heat at 520°C (r = 15°C/min) for 4 h	Melamine mass: 2, 4, 6, 8 and 10 g	92.39 m ² /g 2.71 eV

Table 10 – Synthetic methods of composites with TiO₂ nanofibers, nanowires and nanobelts and g-C₃N₄ nanosheets

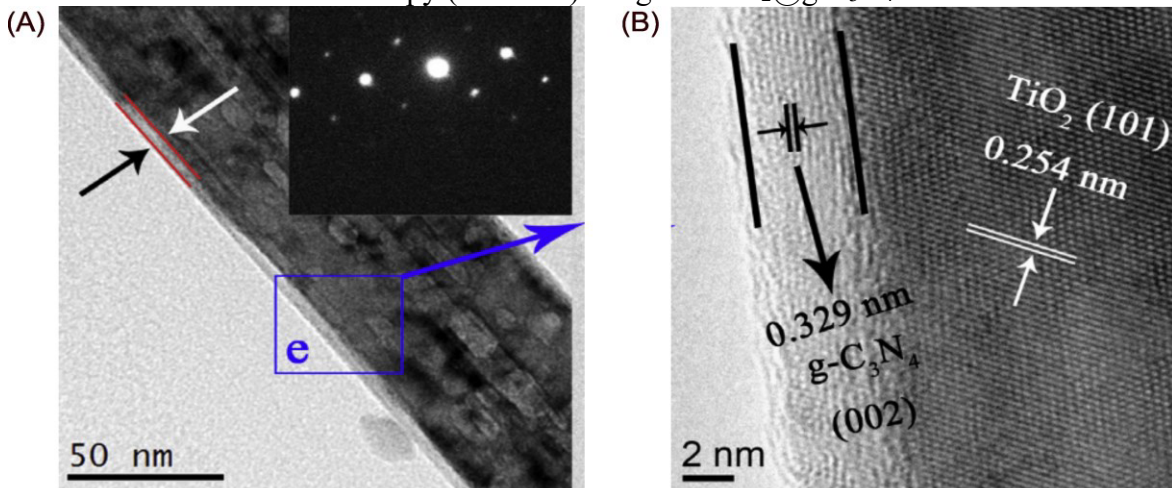
Reference	Precursor	Mixing technique	Joining technique	Variable parameter	Surface area Bandgap
(SUN <i>et al.</i> , 2018)	P25 Dicyandiamide	Ultrasonication for 30 min	<u>Hydrothermal:</u> autoclave for 4 h at 200° C	g-C ₃ N ₄ /TiO ₂ mass ratio: 0.2, 1, 5 and 8	2.63-2.93 eV
(SONG <i>et al.</i> , 2020)	Titanium isopropoxide (TIP) Melamine	-	<u>Calcination:</u> heat at 320°C for 1 h and at 520°C for 2 h	Melamine mass: 0.1, 0.2 and 0.5 g	-
(MA <i>et al.</i> , 2018a)	Anatase TiO ₂ Thiourea	Sonication for 10 min and dry at 70 °C for 12 h	<u>Calcination:</u> heat at 550°C for 4 h (r = 5 °C/min)	KBr mass: 0.009, 0.015 and 0.021 g	25.67-26.38 m ² /g 2.55 eV

Source: elaborated by the author.

3.9 TiO₂ nanorods

TiO₂@g-C₃N₄ core-shell nanorod arrays were fabricated by a saturated aqueous solution method (HAO *et al.*, 2017a). In this method, rutile TiO₂ nanorod arrays were immersed in a heptazine saturated solution to form a shell. Transformation of melamine into a bigger unit of heptazine retarded sublimation during the polymerization process (KUMAR; RAO, 2014). This contributed to the in-situ fabrication of the g-C₃N₄ shell in calcination, producing a thin layer of g-C₃N₄ on the surface of rutile TiO₂ nanorods (Figure 10A and 10B).

Figure 10 – (A) Transmission electronic microscopy (TEM) image and (B) high-resolution transmission electron microscopy (HRTEM) image of TiO₂@g-C₃N₄



Source: adapted from Hao *et al.* (2017a).

Using a simple hydrothermal method Luan *et al.* (2018) formed an heterojunction between TiO₂ nanorods and g-C₃N₄ nanosheets (CN NS) from titanium (III) chloride and urea. The addition of g-C₃N₄ in the reaction solution enabled it to be the loaded *in situ*, resulting in a well distributed CN NS on to surface of TiO₂ nanorods.

Construction of g-C₃N₄/TiO₂ nanorods was based on vacuum-assisted impregnation, aimed to overcome capillary force generated by thermal polymerization of cyanamide confined in protonated titanate nanotubes (H-TNTs) (JIANG *et al.*, 2020). Cyanamide (CA) and alcohol penetrated the space inside of the H-TNTs, allowing the permanence of g-C₃N₄ precursor in the structure after the ethanol evaporation. A part of CA was decomposed to yield NH₃, while the rest was polymerized into g-C₃N₄. During this process, H-TNTs were shrunk and dehydrated to form TiO₂ nanorods. NH₃ released generated oxygen vacancies protected between intern and extern layers of g-C₃N₄.

These synthetic processes are presented in Table 11.

Table 11 – Synthetic methods of composites with TiO₂ nanorods and g-C₃N₄ nanosheets

Reference	Precursor	Mixing technique	Joining technique	Variable parameter	Surface area Bandgap
(LUAN <i>et al.</i> , 2018)	Titanium (III) chloride Urea	Stirring for 3 h	<u>Solvothermal</u> : autoclave for 3 h at 90°C, wash and dry for 12 h at 60°C	g-C ₃ N ₄ mass: 90, 120 and 150 mg	241.5 m ² /g 2.9 eV
(HAO <i>et al.</i> , 2017a)	Titanium butoxide Melamine	Immersion for 15 min and dry at 80°C for 30 min	<u>Calcination</u> : heat at 500°C for 2 h	Heptazine saturated solution/deionized water volume ratio: 3:7, 5:5 and 7:3	2.75 eV
(JIANG <i>et al.</i> , 2020)	TiO ₂ P25 Cyanamide	-	<u>Vacuum treatment-calcination</u> : heat at 55 °C for 60 min in the vacuum, evaporation at 65°C and heat at 550 °C (r = 3°C/min) for 120 min	Cyanamide mass: 100, 200, 400, 600 and 800 mg	2.98 eV

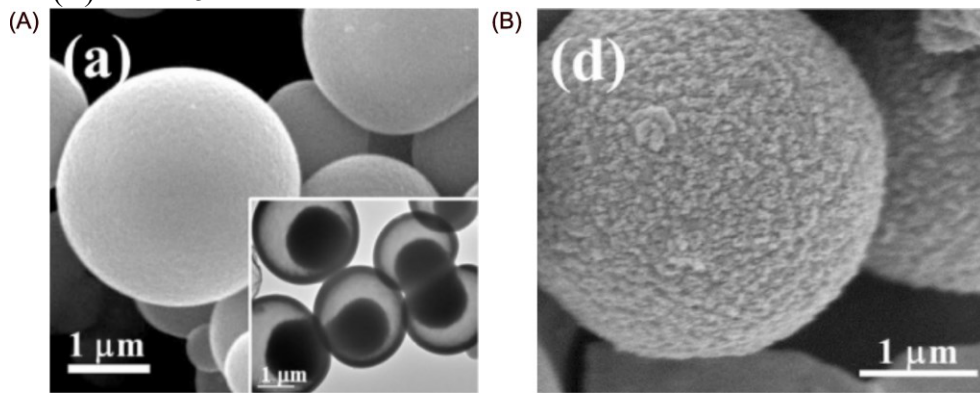
Source: elaborated by the author.

3.10 TiO₂ spheres

A series of core-shell composites with variable content of g-C₃N₄ were prepared by

self-assembly method (MA *et al.*, 2018b). Microspheres with a unique sphere-in-sphere structure (Figure 11A) formed the core-shell structure. This structure was composed of TiO₂ hollow microspheres as the core and g-C₃N₄ as the shell (Figure 11b). The small size, low density, and high dissolution of g-C₃N₄ particles on the TiO₂ surfaces during ultrasonic treatment were responsible for the surface area increase. The elevated content of the hydroxyl in the CNT-15 surface composite possibly contributed to the trap of holes, enhanced charge-transfer efficiency, and photocatalytic activity.

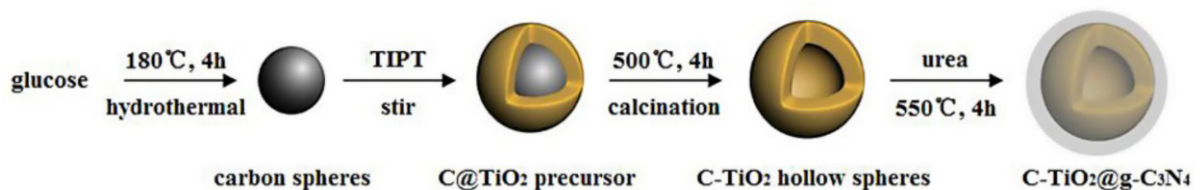
Figure 11 – SEM images of (A) CNT-0 (pristine TiO₂ hollow microsphere) and (B) CNT-15



Source: adapted from Ma *et al.* (2018b).

In-situ growth was used to deposit g-C₃N₄ on the surface of C-TiO₂ hollow spheres providing intimate contact between the semiconductors (ZOU *et al.*, 2017). Synthesis of C-TiO₂ hollow spheres used carbon spheres as template and the application of hydrothermal method followed by calcination (Figure 12). The authors attributed the reduced surface area of composite formed to the covering or filling of some mesopores by g-C₃N₄. In spite of that, the good performance of the composites could be attributed to g-C₃N₄ visible light response, to the improvement of the efficiency of charge separation due to the strong interactions between materials, and to the reflections of light within the interior cavity of the spherical structure.

Figure 12 – Schematic illustration of the preparation of C-TiO₂@g-C₃N₄



Source: adapted from Zou *et al.* (2017).

Spheres composed of TiO₂ nanosheets with a high percentage of {001} facets and g-C₃N₄ formed a heterojunction via a solvothermal method followed by calcination (MA *et al.*, 2016). G-C₃N₄ was adsorbed on the surface of the TiO₂ sheets with a high percentage of {001} facets, affecting the local reaction environment, and influencing the crystal growing condition and final crystallinity. The added hydrofluoric acid (HF) in synthesis reduced surface energies of anatase crystal, especially {001} facets. Besides, F⁻ effectively stabilized {001} facets, restraining the growth along the direction. Enhanced photocatalytic efficiency could be attributed to reactive {001} TiO₂ crystal facets and interfacial connections between g-C₃N₄ and TiO₂.

The synthetic procedures reported above are shown in Table 12.

Table 12 – Synthetic methods of composites with TiO₂ spheres and g-C₃N₄ nanosheets

Reference	Precursor	Mixing technique	Joining technique	Variable parameter	Surface area Bandgap
(MA <i>et al.</i> , 2018b)	Ammonium hexafluoro-titanate Melamine	Stirring for 24 h and evaporation at 80°C	<u>Thermal treatment</u> : dry under vacuum at 70°C	g-C ₃ N ₄ mass: 0, 0.01, 0.02, 0.04, 0.10, 0.15 and 0.20 g	30.6-41.6 m ² /g 2.75 eV
(ZOU <i>et al.</i> , 2017)	Titanium isopropoxide (TIPT) Urea	Dispersion by ultrasonic treatment	<u>Calcination</u> : heat at 550°C for 2 h	Urea/C-TiO ₂ weight ratio: 1:1, 2:1 and 3:1	67-121.1 m ² /g
(MA <i>et al.</i> , 2016)	Tetrabutyl titanate (TBOT) Melamine	Sonication for 30 min	<u>Solvothermal-calcination</u> : autoclave at 180°C for 12 h, wash, dry in vacuum at 40°C and heat at 450°C for 1 h	g-C ₃ N ₄ wt%: 10, 30, 50, 70 and 80	2.55 eV

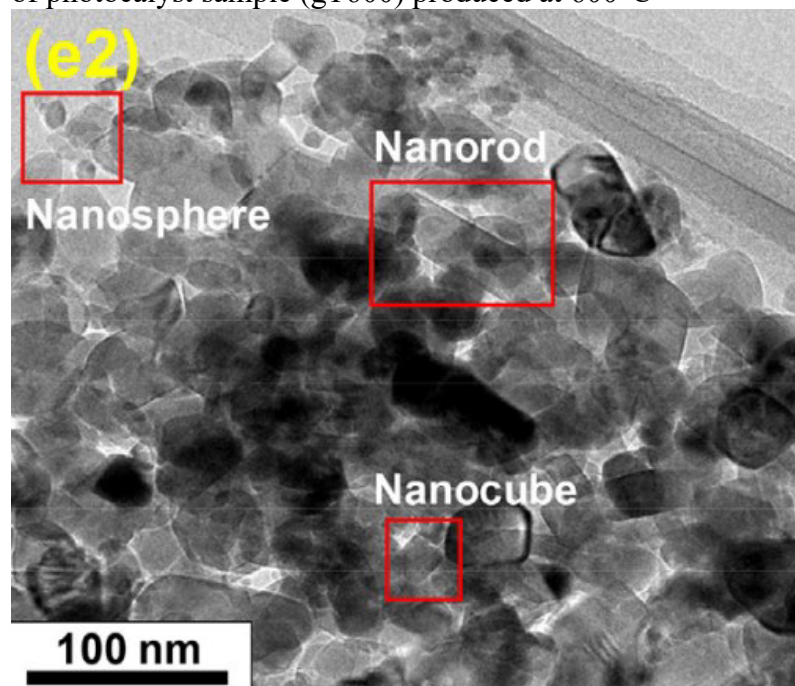
Source: elaborated by the author.

3.11 Different morphologies

The simultaneous growth of TiO₂ anatase/rutile mixed-phase and g-C₃N₄ with desirable properties was successfully obtained via sol-gel-assisted heat treatment (MOHAMED *et al.*, 2018b). Variation of temperature was used to understand the evolution of core-shell

nanoarchitectures. At 400°C, the formation of anatase and rutile was observed, as well as a complete transformation of urea into g-C₃N₄. On the other hand, at 600°C, the generation of nanoparticles anatase/rutile mixed phase with shape nanostructures as nanorod, nanospheres, nanocubes, and others occurred (Figure 13). This method developed a core-shell structure composed of anatase/rutile mixed-phase as a core and g-C₃N₄ as a shell. The use of urea does not only function as a g-C₃N₄ precursor but also was responsible for the *in-situ* nitrogen and carbon doping.

Figure 13 – Transmission electron microscopy (TEM) image of photocatalyst sample (gT600) produced at 600°C



Source: adapted from Mohamed *et al.* (2019).

A seed-induced solvothermal method was used to grow various TiO₂ nanostructures (0D nanoparticles, 1D nanowires, 2D nanosheets and 3D mesoporous nanocrystals) on g-C₃N₄ surfaces (LI *et al.*, 2015d). The microstructure and morphology of TiO₂ were readily tunable by the seed-induced growth approach. Researchers produced a heterojunction composed of meso-TiO₂ nanospheres (3D) and CN nanosheets (2D) with well-dispersed and intimate interfacial contact. Raise of seed concentration (>1 mM) produced 0D/2D type hybrid structure due to the restraint of self-assembly, leading to complete suppression of meso-TiO₂ nanosphere. Besides these structures, heterojunctions with TiO₂ nanowires (1D) and ultrathin nanosheets (2D) were synthesized. Seed-induced growth generated more homogeneous dispersions, enabling a better charge separation and an efficient electron transfer in the hybrid structure.

The synthetic methods are systematized in Table 13.

Table 13 – Synthetic methods of composites with TiO₂ different morphologies and g-C₃N₄ nanosheets

Reference	Precursor	Mixing technique	Joining technique	Reference	Surface area Bandgap
(LI <i>et al.</i> , 2015c)	Titanium tetrachloride Titanium (IV) oxysulfate Urea	Stir for 20 min	<u>Solvothermal:</u> Autoclavation at 105°C for 48 h, centrifugation, wash and dry at 60°C in air overnight	Aqueous TiCl ₄ seed: 5, 30, 60, 240 μM and 1 mM	102 m ² /g
(MOHAMED <i>et al.</i> , 2018b)	Titanium-n-butoxide Urea	Stir for 30 min and after addict of HNO ₃ stir for 30 min	<u>Calcination:</u> ground and heat in air for 4 h (r = 5°C/min)	Calcination temperature: 300, 400, 500 and 600°C	11.31-51.73 m ² /g 2.45-2.53 eV

Source: elaborated by the author.

4 DISCUSSION

The manufacture of composites based on TiO₂ nanoparticles used methods such as calcination, vapor deposition, solvothermal, atomic layer deposition (ALD), crystallization, and hydrothermal. However, calcination has been the most widely studied due to its ability to link semiconductor materials during synthesis. Calcination temperature influenced the composite surface area and structural organization of the g-C₃N₄ molecule (QU *et al.*, 2016). Fagan *et al.* (2016) reported that temperature calcination of 600°C did not produce composites with activity under visible light.

The vapor deposition method involved the calcination process without contact between precursors, coupling semiconductors from melamine sublimation (TAN *et al.*, 2018b). Some studies included substances as montmorillonite, polyethylene glycol (PEG), and cetyl trimethyl ammonium bromide to develop new structural organizations or to increase pores formation (LI *et al.*, 2021; SHEN *et al.*, 2017). A higher porous structure contains more active centers for the capture, photocatalytic degradation, and more efficient diffusion of organic molecules (OUYANG *et al.*, 2021).

Non-modified TiO₂ nanoparticles were linked with non-doped and doped g-C₃N₄ nanosheets. P, C, Na, and protons were introduced in the g-C₃N₄ structure (HAO *et al.*, 2017b; HU *et al.*, 2019; LI *et al.*, 2016a; LIU *et al.*, 2019). These modifications altered the surface area,

porosity, and surface charge of composites. In addition, dopant excess acted as a recombination center.

Composites with modified TiO₂ nanoparticles also could be organized according to g-C₃N₄ nanosheets. N, S, C, and Ti³⁺ were introduced in TiO₂ nanoparticles structures, while g-C₃N₄ nanosheets remained non-doped (HOSSAIN *et al.*, 2021; KONG *et al.*, 2018; OUYANG *et al.*, 2021; WU *et al.*, 2016). Some studies produced heterojunctions with modifications both in TiO₂ nanoparticles and g-C₃N₄ nanosheets (HUANG *et al.*, 2019; LI *et al.*, 2017a; MA *et al.*, 2021). This strategy reduced the bandgap size and extended the adsorption spectrum to the visible light region (JIANG *et al.*, 2018). The modifications variability consolidated TiO₂ nanoparticles as morphology most explored in composites production.

Solvothermal and calcination methods were also applied to fabricate composites with TiO₂ morphologies of mesocrystals and quantum dots. These methods generated TiO₂ mesocrystals structures with specific surface areas between 165 and 557.4 m²/g. In addition, Ti³⁺ species and vacancies promoted charges separation in the heterojunctions (ELBANNA; FUJITSUKA; MAJIMA, 2017; TAN *et al.*, 2018a; YU *et al.*, 2018). A bandgap of 2.34 eV was observed in composite with TiO₂ quantum dots modified by oxygen vacancies and fluorine (SHI *et al.*, 2019). The pores and mesopores formation and the increase of active sites also enhanced photocatalytic performance.

Several studies produced composites from coupling non-modified TiO₂ and doped g-C₃N₄ nanosheets. G-C₃N₄ nanosheets were doped with C, O, and H (ZHANG *et al.*, 2020; ZHONG *et al.*, 2018). The reported methods were solvothermal, calcination, deposition vapor, hydrothermal, and charge-induced aggregation. Solvothermal, co-calcination, and charge-induced aggregation methods were studied by Zhong *et al.* (2018), which observed covalent linkages only in composites produced by solvothermal. Zhang *et al.* (2020) observed that acid or alkaline pretreatment developed electrostatic forces contributing to the increase of semiconductors junction strength.

Composites based on TiO₂ nanotubes were fabricated by calcination and hydrothermal method. Change in precursors proportion and calcination temperature allowed structural control, producing a composite with P25 characteristics (JI *et al.*, 2020). Composites with TiO₂ nanotubes and g-C₃N₄ quantum dots developed a high density of “hot spots” (KUMAR *et al.*, 2020). The smallest bandgap (1.8 eV) was developed from titanium (Ti) foil and urea by calcination (SIM *et al.*, 2020).

Composites with TiO₂ nanofibers, nanowires, and nanobelts were synthesized by vapor deposition, hydrothermal, and calcination. Nanotubes were transformed into nanofibers

with Ti^{3+} before being submitted to the hydrothermal method (SUN *et al.*, 2018). Cobalt-doped nanofibers were composed of a core-shell structure with g- C_3N_4 , while the heterojunction was formed using nanobelts doped with potassium and g- C_3N_4 nanosheets (MA *et al.*, 2018b; SONG *et al.*, 2020).

Solvothermal, calcination, and vacuum treatment methods were used to synthesize composites based on TiO_2 nanorods. The solvothermal method allowed core-shell structure formation from TiO_2 nanorods with a saturated heptazine solution (HAO *et al.*, 2017a). Nanorods with vacancies containing internal and external g- C_3N_4 layers were produced by vacuum treatment and calcination (JIANG *et al.*, 2020). Luan *et al.* (2019) applied the hydrothermal method to develop a structure with load *in situ*, producing photocatalyst surface area with a large surface of $241.5 \text{ m}^2/\text{g}$.

Composites with TiO_2 spheres and g- C_3N_4 nanosheets were fabricated by vacuum treatment, calcination, and solvothermal. Ma *et al.* (2018b) built core-shell structures with TiO_2 microspheres and g- C_3N_4 by thermal treatment in a vacuum. Most syntheses applied no pretreatment to obtain the composite with a greater surface area, while few studies used ultrasonic pretreatment to enhance particle dispersion. Doping with C and the interior cavity of TiO_2 hollow spheres increased the luminous energy utilization in the composite (ZOU *et al.*, 2017). Ma, Wang, and He (2016) enhanced the g- C_3N_4 photocatalytic performance with spheres composed by assembly of TiO_2 nanosheets with a high percent of {001} facets synthesized by the solvothermal-calcination method.

The technique involving seed-induced solvothermal formed composites of TiO_2 structural types by altering seed amounts (LI *et al.*, 2015d). This method promoted homogenous dispersions, better charge separation, and efficient electron transfer. In addition, different structural forms and structure core-shell were developed throughout the temperature calcination procedure (MOHAMED *et al.*, 2018b).

Since sol-gel, precipitation, or hydrothermal methods are considered complex and time-consuming, a more convenient method could facilitate composite synthesis (SHEN *et al.*, 2017). Calcination has been used individually or as an added step of the process. This technique was able to promote the fusion of precursors and obtain a better interfacial connection between TiO_2 and g- C_3N_4 (SHEN *et al.*, 2017). In addition, the hydrothermal method provided a better nanoparticles distribution and a stronger interface between semiconductors to decrease the recombination rate of photogenerated pairs compared with the physical mixture (MA; WANG; HE, 2016; QU *et al.*, 2016).

The parameters studied in composite synthesis were the amount of g- C_3N_4

precursor, amount of TiO₂ precursor, the proportion of precursors, calcination temperature, number of ALD cycles, washing time, and dopant mass. Parameters variation aimed for a composite with a high interfacial connection between semiconductors materials to promote charge separation (SHEN *et al.*, 2017). Electrons in the g-C₃N₄ conduction band can be transferred to the TiO₂ conduction band, while holes in the TiO₂ valence band can be displaced to the g-C₃N₄ valence band from interfacial interaction (MA; WANG; HE, 2016). This reduced charges recombination, while more electrons and holes could participate in photocatalytic reactions (LI *et al.*, 2015a).

Separation of charges and large specific surface area was responsible for increased photocatalytic capability under visible light (JIA *et al.*, 2020; QU *et al.*, 2016). Commonly, a photocatalyst with a large surface area could contain more active sites for adsorption and photodegradation of organic pollutants (DONG *et al.*, 2015; QU *et al.*, 2016). However, an excess of g-C₃N₄ nanosheets can interfere with composite photocatalytic performance (FAGAN *et al.*, 2016; JIA *et al.*, 2020; LV *et al.*, 2019). G-C₃N₄ nanosheets can cover active sites of TiO₂ surface, blocking the participation of region and hindering photocatalytic reactions (FAGAN *et al.*, 2016; JIA *et al.*, 2020).

5 CONCLUSION

As result of the systematic review, the most common methods used were the calcination, hydrothermal, and solvothermal. Calcination was recognized to be less time-consuming method, while hydrothermal succeeded to develop a strong interface between semiconductors.

In the calcination process, the influence of temperature is a variable determining the characteristics of the composite. The synthetic methods for the formation of composites with TiO₂ nanoparticles has been widely studied. On the other hand, other morphologies such as mesocrystals, quantum dots, nanofibers, nanowires, nanobelts, nanorods and spheres were less commonly published. The application of new techniques such as atomic layer deposition (ALD), vapor deposition and charge-induced aggregation has been tested to construct composites, but in a smaller scale.

Semiconductors doping has been applied to modify the structure and to extend light absorption, although the doping of g-C₃N₄ nanosheets has been considered for composites, composites with other TiO₂ morphologies are more widely used. Spherical structures with hydroxylated species across the entire surface showed a better use of light, increasing

photocatalytic efficiency.

Among the parameters studied for synthetic methods, the amount of g-C₃N₄ precursor, amount of TiO₂ precursor and the precursor proportion have been investigated to find the optimal concentration. Calcination has been able to produce composites with promising characteristics similar to more elaborate techniques for photocatalytic application. Synthetic parameters investigation is necessary to produce more efficient composites for application in photocatalytic systems.

REFERENCES

- AHMED, S.; HAIDER, W. Heterogeneous photocatalysis and its potential applications in water and wastewater treatment: a review. **Nanotechnology**, v. 29, n. 34, p. 342001, 2018.
- BALAKRISHNAN, A.; CHINTHALA, M. Comprehensive review on advanced reusability of g-C₃N₄ based photocatalysts for the removal of organic pollutants. **Chemosphere**, v. 297, 2022.
- CHEN, X.; MAO, S. Titanium dioxide nanomaterials: Synthesis, properties, modifications and applications. **Chemical Reviews**, v. 107, n. 7, p. 2891–2959, 2007.
- CUSHING, S. *et al.* Effects of defects on photocatalytic activity of hydrogen-treated titanium oxide nanobelts. **Acs Catalysis**, v. 7, n. 3, p. 1742-1748, 2017.
- DING, M. *et al.* Facile in situ synthesis of 2D porous g-C₃N₄ and g-C₃N₄/P25(N) heterojunction with enhanced quantum effect for efficient photocatalytic application. **Journal of Alloys and Compounds**, v. 635, p. 34–40, 2015.
- DONG, G. *et al.* Facile synthesis of porous graphene-like carbon nitride (C₆N₉H₃) with excellent photocatalytic activity for NO removal. **Applied Catalysis B: Environmental**, v. 174, p. 477-485, 2015.
- DRESSEL, W. Engineering Village. **The Charleston Advisor**, v. 19, n. 1, p. 19–22, 2017.
- ELBANNA, O.; FUJITSUKA, M.; MAJIMA, T. G-C₃N₄/TiO₂ mesocrystals composite for H₂ evolution under visible-light irradiation and its charge carrier dynamics. **ACS Applied Materials and Interfaces**, v. 9, n. 40, p. 34844–34854, 2017.
- FAGAN, R. *et al.* Photocatalytic properties of g-C₃N₄-TiO₂ heterojunctions under UV and visible light conditions. **Materials**, v. 9, n. 4, 2016.
- FUJISHIMA, A.; HONDA, K. Electrochemical Photolysis of Water at a Semiconductor Electrode. **Nature**, v. 238, n. 5358, p. 37–38, 1972.
- GU, W. *et al.* Face-to-Face Interfacial Assembly of Ultrathin g-C₃N₄ and Anatase TiO₂ Nanosheets for Enhanced Solar Photocatalytic Activity. **ACS Applied Materials & Interfaces**, v. 9, n. 34, p. 28674–28684, 2017.
- HAO, J. *et al.* Synthesis of TiO₂@g-C₃N₄ core-shell nanorod arrays with Z-scheme enhanced photocatalytic activity under visible light. **Journal of Colloid and Interface Science**, v. 508, p. 419–425, 2017a.
- HAO, R. *et al.* In situ hydrothermal synthesis of g-C₃N₄/TiO₂ heterojunction photocatalysts with high specific surface area for Rhodamine B degradation. **Applied Surface Science**, v. 411, p. 400–410, 2017b.
- HOSSAIN, S. *et al.* Synthesis and NO_x removal performance of anatase S–TiO₂/g-CN heterojunction formed from dye wastewater sludge. **Chemosphere**, v. 275, p. 130020, 2021.

HU, Y.; TSAI, H.; HUANG, C. Effect of brookite phase on the anatase–rutile transition in titania nanoparticles. **Journal of the European Ceramic Society**, v. 23, n. 5, p. 691–696, 2003.

HU, Z. *et al.* Construction of carbon-doped supramolecule-based g-C₃N₄/TiO₂ composites for removal of diclofenac and carbamazepine: A comparative study of operating parameters, mechanisms, degradation pathways. **Journal of Hazardous Materials**, v. 380, p. 120812, 2019.

HUANG, Y. *et al.* Protonated g-C₃N₄/Ti³⁺ self-doped TiO₂ nanocomposite films: Room-temperature preparation, hydrophilicity, and application for photocatalytic NO_x removal. **Applied Catalysis B: Environmental**, v. 240, p. 122–131, 2019.

HUI, J. *et al.* Graphitic-C₃N₄ coated floating glass beads for photocatalytic destruction of synthetic and natural organic compounds in water under UV light. **Journal of Photochemistry & Photobiology, A: Chemistry**, v. 405, p. 112935, 2021.

Ji, H. *et al.* 2D/1D graphitic carbon nitride/titanate nanotubes heterostructure for efficient photocatalysis of sulfamethazine under solar light: Catalytic “hot spots” at the rutile–anatase–titanate interfaces. **Applied Catalysis B: Environmental**, v. 263, p. 118357, 2020.

JIA, J. *et al.* MOF-derived the direct Z-scheme g-C₃N₄/TiO₂ with enhanced visible photocatalytic activity. **Journal of Sol-Gel Science and Technology**, v. 93, n. 1, p. 123–130, 2020.

JIANG, D. *et al.* Nanotube confinement-induced g-C₃N₄/TiO₂ nanorods with rich oxygen vacancies for enhanced photocatalytic water decontamination. **Applied Physics A**, v. 126, n. 4, p. 246, 2020.

JIANG, G. *et al.* Photocatalytic NO oxidation on N-doped TiO₂/g-C₃N₄ heterojunction: Enhanced efficiency, mechanism and reaction pathway. **Applied Surface Science**, v. 458, n. July, p. 77–85, 2018.

JIANG, X. *et al.* Sustainable methods for decontamination of microcystin in water using cold plasma and uv with reusable TiO₂ nanoparticle coating. **International Journal of Environmental Research and Public Health**, v. 14, n. 5, p. 480, 2017.

KHEDR, T. *et al.* Photodegradation of microcystin-LR using visible light-activated C/N-co-modified mesoporous TiO₂ photocatalyst. **Materials**, v. 12, n. 7, p. 1027, 2019.

KONG, L. *et al.* Ti³⁺ defect mediated g-C₃N₄/TiO₂ Z-scheme system for enhanced photocatalytic redox performance. **Applied Surface Science**, v. 448, p. 288–296, 2018.

KUMAR, P. *et al.* Noble metal free, visible light driven photocatalysis using TiO₂ nanotube arrays sensitized by P-doped C₃N₄ quantum dots. **Advanced Optical Materials**, v. 8, n. 4, 2020.

KUMAR, S.; RAO, K. Polymorphic phase transition among the titania crystal structures using a solution-based approach: from precursor chemistry to nucleation process. **Nanoscale**, v. 6,

n. 20, p. 11574–11632, 2014.

LAI, Y. *et al.* Recent advances in TiO₂-based nanostructured surfaces with controllable wettability and adhesion. **Small**, v. 12, n. 16, p. 2203–2224, 2016.

LI, G. *et al.* Enhanced visible-light-driven photocatalytic inactivation of *Escherichia coli* using g-C₃N₄/TiO₂ hybrid photocatalyst synthesized using a hydrothermal-calcination approach. **Water Research**, v. 86, p. 17–24, 2015a.

LI, K. *et al.* In-situ-reduced synthesis of Ti³⁺ self-doped TiO₂/g-C₃N₄ heterojunctions with high photocatalytic performance under led light irradiation. **ACS Applied Materials & Interfaces**, v. 7, n. 17, p. 9023–9030, 2015b.

LI, K. *et al.* Synergetic effect of Ti³⁺ and oxygen doping on enhancing photoelectrochemical and photocatalytic properties of TiO₂/g-C₃N₄ heterojunctions. **ACS Applied Materials & Interfaces**, v. 9, n. 13, p. 11577–11586, 2017a.

LI, S. *et al.* A sustainable approach for lignin valorization by heterogeneous photocatalysis. **Green Chemistry**, v. 18, n. 3, p. 594–607, 2016a.

LI, Y. *et al.* Seed-induced growing various TiO₂ nanostructures on g-C₃N₄ nanosheets with much enhanced photocatalytic activity under visible light. **Journal of Hazardous Materials**, v. 292, p. 79–89, 2015c.

LI, Y. *et al.* Hybridization of rutile TiO₂ (rTiO₂) with g-C₃N₄ quantum dots (CN QDs): An efficient visible-light-driven Z-scheme hybridized photocatalyst. **Applied Catalysis B: Environmental**, v. 202, p. 611–619, 2017b.

LI, Y.; WHITE, T.; LIM, S. Low-temperature synthesis and microstructural control of titania nano-particles. **Journal of Solid State Chemistry**, v. 177, n. 4–5, p. 1372–1381, 2004

LI, Z. *et al.* Phosphorus-doped g-C₃N₄ nanosheets coated with square flake-like TiO₂: Synthesis, characterization and photocatalytic performance in visible light. **Journal of Molecular Catalysis A: Chemical**, v. 425, p. 340–348, 2016b.

LI, Z. *et al.* Preparation of heterogeneous TiO₂/g-C₃N₄ with a layered mosaic stack structure by use of montmorillonite as a hard template approach: TC degradation, kinetic, mechanism, pathway and DFT investigation. **Applied Clay Science**, v. 207, 2021.

LIU, H. *et al.* Fabrication of surface alkalized g-C₃N₄ and TiO₂ composite for the synergistic adsorption-photocatalytic degradation of methylene blue. **Applied Surface Science**, v. 473, p. 855–863, 2019.

LOW, J. *et al.* Two-dimensional layered composite photocatalysts. **Chemical Communications**, v. 50, n. 74, p. 10768-10777, 2014.

LUAN, S. *et al.* Enhancing photocatalytic performance by constructing ultrafine TiO₂ nanorods/g-C₃N₄ nanosheets heterojunction for water treatment. **Science Bulletin**, v. 63, n. 11, p. 683–690, 2018.

- LV, B. *et al.* Vapor deposition of g-C₃N₄ on TiO₂ nanosquares for efficient photodegradation of MB and Cr⁶⁺ under visible light. **Diamond and Related Materials**, v. 110, 2020.
- LV, P. *et al.* Less is more: Enhancement of photocatalytic activity of g-C₃N₄ nanosheets by site-selective atomic layer deposition of TiO₂. **Applied Surface Science**, v. 494, p. 508–518, 2019.
- MA, J. *et al.* Fabrication of g-C₃N₄/TiO₂ hierarchical spheres with reactive {001} TiO₂ crystal facets and its visible-light photocatalytic activity. **International Journal of Hydrogen Energy**, v. 41, n. 6, p. 3877–3887, 2016.
- MA, J. *et al.* Potassium ions intercalated into g-C₃N₄-modified TiO₂ nanobelts for the enhancement of photocatalytic hydrogen evolution activity under visible-light irradiation. **Nanotechnology**, v. 29, n. 21, 2018a.
- MA, J. *et al.* A novel composite material based on hydroxylated g-C₃N₄ and oxygen-vacant TiO₂ for improvement of photocatalytic performance. **Applied Surface Science**, v. 546, 2021.
- MA, J.; WANG, C.; HE, H. Enhanced photocatalytic oxidation of NO over g-C₃N₄-TiO₂ under UV and visible light. **Applied Catalysis B: Environmental**, v. 184, p. 28–34, 2016.
- MA, L. *et al.* Synthesis of core-shell TiO₂@ g-C₃N₄ hollow microspheres for efficient photocatalytic degradation of rhodamine B under visible light. **Applied Surface Science**, v. 430, p. 263–272, 2018b.
- MISHRA, A. *et al.* Graphitic carbon nitride (g-C₃N₄)-based metal-free photocatalysts for water splitting: A review. **Carbon**, v. 149, p. 693–721, 2019.
- MOHAMED, M. *et al.* Concurrent growth, structural and photocatalytic properties of hybridized C, N co-doped TiO₂ mixed phase over g-C₃N₄ nanostructured. **Scripta Materialia**, v. 142, p. 143–147, 2018a.
- MOHAMED, M. *et al.* In-depth understanding of core-shell nanoarchitecture evolution of g-C₃N₄@C, N co-doped anatase/rutile: Efficient charge separation and enhanced visible-light photocatalytic performance. **Applied Surface Science**, v. 436, p. 302–318, 2018b.
- NASIR, M. *et al.* Hybridization of g-C₃N₄ quantum dots with 1D branched TiO₂ fiber for efficient visible light-driven photocatalytic hydrogen generation. **International Journal of Hydrogen Energy**, v. 45, n. 27, p. 13994–14005, 2020.
- NGHIA, N.; NEGISHI, N.; HUE, N. Enhanced adsorption and photocatalytic activities of co-doped TiO₂ immobilized on silica for paraquat. **Journal of Electronic Materials**, v. 47, n. 1, p. 692–700, 2018.
- OHTANI, B. Photocatalysis A to Z-What we know and what we do not know in a scientific sense. **Journal of Photochemistry and Photobiology C: Photochemistry Reviews**, v. 11, p. 157–178, 2010.
- OUYANG, W. *et al.* Visible-light-response g-C₃N₄@N,S-TiO₂ nanocomposites for superior photocatalysis and photoelectrochemical performance. **Journal of Alloys and Compounds**,

v. 866, 2021.

PAN, X. *et al.* Defective TiO₂ with oxygen vacancies: synthesis, properties and photocatalytic applications. *Nanoscale*, v. 5, n. 9, p. 3601, 2013.

QU, A. *et al.* Effects of calcining temperature on photocatalysis of g-C₃N₄/TiO₂ composites for hydrogen evolution from water. *Materials Research Bulletin*, v. 80, p. 167–176, 2016.

SHALOM, M. *et al.* Improving Carbon Nitride Photocatalysis by Supramolecular Preorganization of Monomers. *Journal of the American Chemical Society*, v. 135, n. 19, p. 7118–7121, 2013.

SHEN, G. *et al.* Easy synthesis of g-C₃N₄/TiO₂ heterostructure photocatalyst with large surface area and excellent photocatalytic activity. *Ceramics International*, v. 43, 2017.

SHI, H. *et al.* Interfacial charge transfer in 0D/2D defect-rich heterostructures for efficient solar-driven CO₂ reduction. *Applied Catalysis B: Environmental*, v. 245, p. 760–769, 2019.

SIM, L. *et al.* In situ growth of g-C₃N₄ on TiO₂ nanotube arrays: Construction of heterostructures for improved photocatalysis properties. *Journal of Environmental Chemical Engineering*, v. 8, n. 1, 2020.

SOLOMON, R. *et al.* Enhanced photocatalytic degradation of azo dyes using nano Fe₃O₄. *Journal of the Iranian Chemical Society*, v. 9, n. 2, p. 101–109, 2012.

SONG, J. *et al.* Highly flexible, core-shell heterostructured, and visible-light-driven titania-based nanofibrous membranes for antibiotic removal and *E. coil* inactivation. *Chemical Engineering Journal*, v. 379, 2020.

SRIDHARAN, K.; JANG, E.; PARK, T. J. Novel visible light active graphitic C₃N₄-TiO₂ composite photocatalyst: Synergistic synthesis, growth and photocatalytic treatment of hazardous pollutants. *Applied Catalysis B: Environmental*, v. 142–143, p. 718–728, 2013.

SU, J. *et al.* Porous titania with heavily self-doped Ti³⁺ for specific sensing of Co at room temperature. *Inorganic Chemistry*, v. 52, n. 10, p. 5924–5930, 2013.

SUN, M. *et al.* Rice spike-like g-C₃N₄/TiO₂ heterojunctions with tight-binding interface by using sodium titanate ultralong nanotube as precursor and template. *Ceramics International*, v. 44, n. 7, p. 8125–8132, 2018.

TAN, B. *et al.* Defective anatase TiO_{2-x} mesocrystal growth in situ on g-C₃N₄ nanosheets: construction of 3D/2D z-scheme heterostructures for highly efficient visible-light photocatalysis. *Chemistry - A European Journal*, v. 24, n. 50, p. 13311–13321, 2018a.

TAN, Y. *et al.* One-step synthesis of nanostructured g-C₃N₄/TiO₂ composite for highly enhanced visible-light photocatalytic H₂ evolution. *Applied Catalysis B: Environmental*, v. 230, p. 260–268, 2018b.

TANG, H. *et al.* Novel spindle-shaped nanoporous TiO₂ coupled graphitic g-C₃N₄ nanosheets with enhanced visible-light photocatalytic activity. *Ceramics International*, v. 42, n. 16, p.

18443–18452, 2016.

WANG, J. *et al.* Engineering Z-system hybrids of 0D/2D F-TiO₂ quantum dots/g-C₃N₄ heterostructures through chemical bonds with enhanced visible-light photocatalytic performance. **New Journal of Chemistry**, v. 45, n. 6, p. 3067–3078, 2021.

WU, Y. *et al.* Mesoporous graphitic carbon nitride and carbon–TiO₂ hybrid composite photocatalysts with enhanced photocatalytic activity under visible light irradiation. **Journal of Environmental Chemical Engineering**, v. 4, n. 1, p. 797–807, mar. 2016.

YANG, Y. *et al.* G-C₃N₄ nanosheets coupled with TiO₂ nanosheets as 2D/2D heterojunction photocatalysts toward high photocatalytic activity for hydrogen production. **Catalysis Letters**, v. 149, p. 2930–2939, 2019.

YU, X. *et al.* Mesocrystalline Ti³⁺–TiO₂ hybridized g-C₃N₄ for efficient visible-light photocatalysis. **Carbon**, v. 128, p. 21–30, 2018.

ZHANG, J. *et al.* Sulfur-mediated synthesis of carbon nitride: Band-gap engineering and improved functions for photocatalysis. **Energy Environ. Sci.**, v. 4, n. 3, p. 675–678, 2011.

ZHANG, K. *et al.* Preparation of highly visible light active Fe–N co-doped mesoporous TiO₂ photocatalyst by fast sol–gel method. *Journal of Nanoparticle Research*, v. 16, n. 2, p. 2246, 14 fev. 2014.

ZHANG, Y. *et al.* Activation of Carbon Nitride Solids by Protonation: Morphology Changes, Enhanced Ionic Conductivity, and Photoconduction Experiments. **Journal of the American Chemical Society**, v. 131, n. 1, p. 50–51, 2009.

ZHANG, Y. *et al.* Strongly interfacial-coupled 2D-2D TiO₂/g-C₃N₄ heterostructure for enhanced visible-light induced synthesis and conversion. **Journal of Hazardous Materials**, v. 394, 2020.

ZHONG, R. *et al.* Covalently bonded 2D/2D O-g-C₃N₄/TiO₂ heterojunction for enhanced visible-light photocatalytic hydrogen evolution. **Applied Catalysis B: Environmental**, v. 237, p. 1130–1138, 2018.

ZHONG, R. *et al.* Comparison of TiO₂ and g-C₃N₄ 2D/2D nanocomposites from three synthesis protocols for visible-light induced hydrogen evolution. **Catalysis Science & Technology**, v. 9, n. 1, p. 75–85, 2019.

ZHOU, C. *et al.* Rational design of carbon-doped carbon nitride/Bi₁₂O₁₇Cl₂ composites: a promising candidate photocatalyst for boosting visible-light-driven photocatalytic degradation of tetracycline. **ACS Sustainable Chemistry & Engineering**, v. 6, n. 5, p. 6941–6949, 2018.

ZOU, Y. *et al.* In situ synthesis of C-doped TiO₂@g-C₃N₄ core-shell hollow nanospheres with enhanced visible-light photocatalytic activity for H₂ evolution. **Chemical Engineering Journal**, v. 322, p. 435–444, 2017.

CHAPTER II

EVALUATION OF PHOTOCATALYTIC PERFORMANCE OF COMPOSITES BASED ON P25 AND CN ACTIVATED BY ARTIFICIAL AND NATURAL LIGHT

ABSTRACT

New synthetic methods of composites and reactor configurations have emerged to investigate heterogeneous photocatalysis. This study aimed to evaluate the photocatalytic activity of semiconductor composites and pristine semiconductors under the effect of two light sources (artificial lamp and natural sunlight). For this, composites were synthesized (CN25 and CN75) from commercial titanium dioxide (P25) and graphitic carbon nitride (CN). The photocatalytic experiments with methylene blue (MB) solutions were performed in two different reactors (A and B). Central Composite Design (CCD) was applied to study the effect of main factors (pH, photocatalyst dosage, and initial concentration of dye) on MB removal. In order to complement the understanding of photocatalysis, adsorption isotherms models were adjusted and a kinetic study of P25 was developed. P25 showed superior photocatalytic activity compared to other photocatalysts in different light sources, achieving a maximum removal of 99.4%. The critical points obtained by CCD with R^2 of 0.91 were 6.6, 1.2 g/L, and 1 mg/L to pH, photocatalyst dosage, and initial concentration of MB, respectively. Kinetic rates in photocatalysis with P25 doubled in half time. The findings appointed to the high potential of sunlight energy as the energy source to promote photocatalysis of pollutants with pristine P25.

Keywords: titanium dioxide; graphitic carbon nitride; sunlight; response surface methodology.

1 INTRODUCTION

Heterogeneous photocatalysis has been applied in water and wastewater treatment due to its capacity to oxidize pollutants through reactive oxygen species (DU *et al.*, 2020; FOTIOU *et al.*, 2016; WU *et al.*, 2016) and for being a eco-friendly alternative (AHMED; HAIDER, 2018). For the chemical activation in photocatalysis, the radiation source must be appropriate to the semiconductor characteristics (JO; TAYADE, 2014; SPASIANO *et al.*, 2015). Charge carriers are generated and initiate the photocatalytic reactions in the semiconductor surface (BETHI *et al.*, 2016).

The combination of photocatalysis with sunlight has a great potential to become a renewable and sustainable treatment processes (FOTIOU *et al.*, 2016). The ultraviolet and

visible regions represent approximately 4 and 42% of the solar spectrum, respectively (TAYEL; RAMADAN; EL SEOUD, 2018). In addition, sunlight utilization could reduce the cost of the treatment process (CHEN *et al.*, 2019; MONTEAGUDO *et al.*, 2020; PÉREZ, 2002). LEDs are recognized for sustainability and efficiency in photocatalysis but become electronic waste at the end of their useful life.

Despite the optimum properties of titanium dioxide (TiO₂), its bandgap (3.2 eV) limits the use of the UV region (LI *et al.*, 2015). A relatively simple strategy to overcome this bottleneck is coupling with another narrowband semiconductor (CHI *et al.*, 2019). Graphitic carbon nitride (g-C₃N₄) is active in visible light due to its suitable bandgap (2.7 eV) (MA *et al.*, 2018). It is promising candidate to applications with solar energy, contributing to solve limitations of TiO₂ photocatalysis (LIU; WANG; ANTONIETTI, 2016; SONG *et al.*, 2018). Several studies have been reported improved photocatalytic performance of TiO₂ with g-C₃N₄ (KONG *et al.*, 2018; MA; WANG; HE, 2016).

This study aims to evaluate the photocatalytic activity of composites based on commercial titanium dioxide (P25) and graphitic carbon nitride (CN) activated by artificial and natural light sources. For this purpose, composites with P25 and CN were synthesized by the calcination method. In addition, Central Composite Design (CCD) was used to understand the factors involved in photocatalysis.

2 METHODOLOGY

2.1 Materials

Commercial titanium dioxide (Aeroxide TiO₂ P25) was donated from Evonik Industries. Hydrochloric acid, sodium hydroxide, methanol, melamine, and methylene blue were also used and of analytical grade.

2.2 Synthesis of graphitic carbon nitride (CN)

Synthesis of graphitic carbon nitride used melamine as the precursor. A semi-closed crucible containing 10 g of melamine was calcined for 2 h at 520°C with a heating rate of 10°C/min. The powder was obtained by grinding after being cooled to room temperature. The product was denoted as CN.

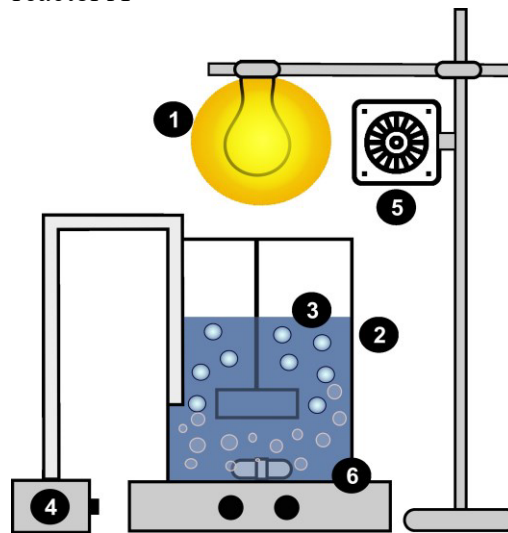
2.3 Synthesis of CN/P25 composites

Composites were prepared with varying weight ratios of CN and P25 (25 and 75% of CN). CN and P25 were added to 30 mL of methanol. The suspension was dispersed by ultrasonication for 30 minutes and magnetic stirring at 60°C for 30 minutes. A covered crucible containing final product was calcined for 2 hours at 400°C with heating rate of 10°C/min. These composites were named as CN25 and CN75.

2.4 Reactors design

Reactor A was covered in a box to avoid any external light during the experiments. A becker containing methylene blue (MB) solution and photocatalyst with constant aeration was placed in reactor A. This reactor consisted of a magnetic stirrer, a cooler directed toward the light source, and a 70 W halogen lamp positioned on the top of the beaker containing the solution (6.5 cm). The reactor components were highlighted in Figure 1: light source (1); MB solution (2); photocatalyst (3); aerator (4); cooler (5); magnetic stirrer (6).

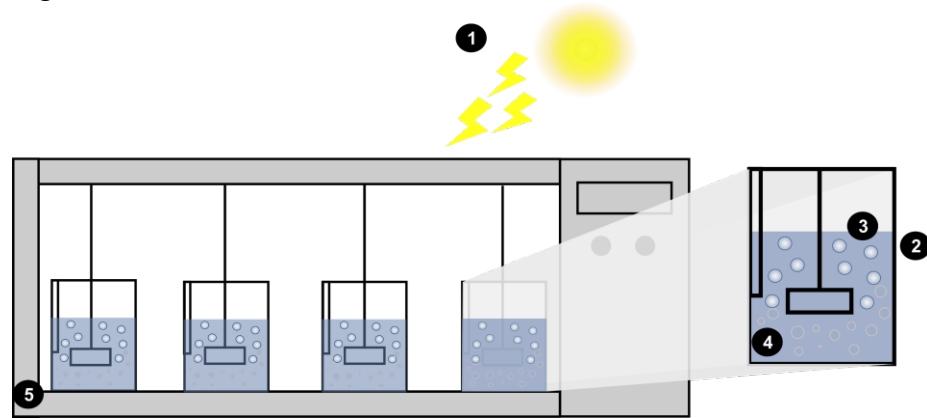
Figure 1 – Schematic illustration of reactor A



Source: elaborated by the author.

Sunlight was used as a light source in the reactor B, while the jar test was responsible for photocatalyst suspension. As shown in Figure 2, reactor B was composed of: light source (1); MB solution (2); photocatalyst (3); aerator (4); jar test (5).

Figure 2 – Schematic illustration of reactor B



Source: elaborated by the author.

2.5 Photocatalytic tests

Methylene blue (MB) was used to evaluate the performance of photocatalysts. Beakers containing MB solutions (10 mg/L) and photocatalysts (0.5 g/L) were illuminated for photocatalysis study. The values for MB solution (DARIANI *et al.*, 2016b; DASSANAYAKE; RAJAKARUNA; ABIDI, 2018; ERTUŞ; VAKIFAHMETOGLU; ÖZTÜRK, 2020) and photocatalysts concentration (DU *et al.*, 2020; MA; WANG; HE, 2016; WANG *et al.*, 2017) were adopted based on the literature. Semiconductor composites (CN25 and CN75) and pristine semiconductors (CN and P25) were exposed to the 70 W halogen lamp (Avant) for 7 hours in reactor A.

Semiconductor materials experimented with sunlight for one hour (from 10 to 11 a.m.) in reactor B. Experiments execution occurred between August and September 2021 in Fortaleza, Ceará, Brazil. The radiation in each run was registered using UV light meter (INSTRUTHERM, MRU-201) with measurement range at 290 nm to 390 nm.

The stabilization of adsorption-desorption equilibrium is provided to ensure photocatalysis evaluation. For this purpose, MB solutions with photocatalysts (Table 1) were stirred for 30 min in the dark, as observed in other studies (LI *et al.*, 2015b, 2017a; LV *et al.*, 2019). Photolysis experiments were performed under a light source but without photocatalysts in MB solutions.

Table 1 – Name and composition of photocatalysts used in experiments (continue)

Name	Weight percentage of CN (%)	Weight percentage of P25 (%)
P25	0	100

Table 1 – Name and composition of photocatalysts used in experiments
(conclusion)

Name	Weight percentage of CN (%)	Weight percentage of P25 (%)
CN25	25	75
CN75	75	25
CN	100	0

Source: elaborated by the author

Samples (4 mL) were collected and filtered by the 0.22 μm Millipore filter to evaluate dye removal. A UV–visible spectrophotometer was used to determine the absorbance of samples at 664 nm (MOHAMED *et al.*, 2018c).

2.6 Statistical analysis

The normality of data was verified using the Shapiro-Wilk test. This test was considered most powerful with different distributions and samples sizes (RAZALI; WAH, 2011). Kruskal–Wallis is a nonparametric test used to determine the existence of statistically significant differences for comparisons of three or more groups and was used in the data analysis. The null hypothesis (H_0) assumed that between representative medians of each population are equal (SHESKIN, 2000). Statistical analysis of experimental data was performed using a statistical software.

2.6.1 Central Composite Design (CCD)

Response Surface Methodology (RSM) is a collection of mathematical and statistical techniques to develop, improve, and optimize processes (BARAHIMI; MOGHIMI; TAHERI, 2019). This approach includes three stages: design and experiments, response surface modeling by regression, and optimization (TAGHIPOUR *et al.*, 2021). RSM was used to determine the optimal conditions for MB removal under sun exposure.

Central Composite Design (CCD) evaluates the main effect of each parameter and their interactions with a minimum number of experiments, being the most common design in the field of RMS (AZARGOHAR; DALAI, 2005; MACHROUHI *et al.*, 2019; VARANK *et al.*, 2020). This experimental design is composed of different design points: factorial or cubic (± 1), central (0) and, star or axials ($\pm \alpha$) (NOMAN *et al.*, 2019). In rotatable design, α represent the distance of an axial point from the center (AHMAD; ALROZI, 2010). According to Equation

(1), this coefficient depends on the number of studied parameters (N_p) in the experiments.

$$\alpha = N_p^{\frac{1}{4}} \quad (1)$$

The factors were pH, MB concentration, and P25 dosage (factors), and the response was MB removal. The experimental setup used reactor B under sun exposure for 1 hour. The experimental plan consists of random experimental runs set of 17 divided into cubics (8 runs), axials (6 runs), and centers (3 runs) points. Levels coded and uncoded of studied factors are shown in Table 2.

Table 2 – Factors and levels (coded and uncoded) used in the CCD with $\alpha = 1.32$

Coded level of factors	Uncoded level		
	pH	P25 dosage (g/L)	MB concentration (mg/L)
Minimum cubic point (-1)	6.20	0.50	10.00
Maximum cubic point (+1)	9.00	1.50	20.00
Central point (0)	7.60	1.00	15.00
Minimum axial point ($-\alpha$)	5.24	0.16	6.59
Maximum axial point ($+\alpha$)	9.95	1.84	23.41

Source: elaborated by the author.

Variables range was based on the literature: MB concentration varied between 5 and 20 mg/L (DARIANI *et al.*, 2016b) and the P25 dosage ranged from 0.1 to 2 g/L (MOHAMED *et al.*, 2018c; YU *et al.*, 2014). The pH ranged used (6.86 to 9.20) was similar to the real conditions observed on the Brazilian supply reservoirs (COGERH, 2008). The pH adjustment of MB solutions was conducted before the experiments adding NaOH and HCl solutions.

A statistical software was used to conceptualize the experimental plane and analyze the interaction between the process variables and the response. The second-order polynomial model can describe this relation mathematically by Equation 2.

$$y = \beta_0 + \sum_{i=1}^k \beta_i x_i + \sum_{i=1}^k \beta_{ii} x_i^2 + \sum_{i=1}^n \sum_{i=1}^{i < j} \beta_{ij} x_i x_j + \varepsilon \quad (2)$$

Where y is the predicted response; x_i and x_j are the variables; $x_i x_j$ is an interaction parameter; x_i^2 is the square effects; β_0 is a constant coefficient; β_i , β_{ii} and β_{ij} are coefficients of the linear, quadratic, and interaction effect; k represents the number of independent variables,

and ε is the random error (MAZHARI *et al.*, 2018). Experimental data were analyzed by multiple linear regression using the analysis of variance (ANOVA) approach, and the statistical significance of each regression term was assessed using the p-value (VARANK *et al.*, 2020).

2.7 Kinetics of photocatalysis

Experiments of photocatalytic process kinetics used the CCD critical points for pH and P25 dosage with MB initial concentration applied in the previous tests. For this, MB solutions were exposed to sunlight for 1 hour in reactor B. The variation of concentration of MB was evaluated by first-order model (Equation 3):

$$-\ln\left(\frac{C_0}{C_t}\right) = kt \quad (3)$$

Where C_0 is the initial MB concentration; C_t is the residual MB concentration at time t ; k is the kinetic constant.

3 RESULTS AND DISCUSSION

3.1 Photocatalysis of composites under artificial light

Firstly, a halogen lamp was chosen as an artificial light source to study composites with proportion CN and P25 variables. Halogen lamps are widely used in the photocatalytic performance evaluation of composites under visible light (ZHANG *et al.*, 2020; ALI *et al.*, 2018; KASSAHUN *et al.*, 2021). Kim *et al.* (2019) observed spectra of a few indoor light sources, concluding that the halogen lamp is in the visible region with greater intensity between 550 and 625 nm.

Data of MB removal obtained by photocatalysts (CN, CN25, CN75, and P25) in reactor A were statistically treated (Table 3). Shapiro-Wilk test indicated that data did not follow a normal distribution (p-value < 0.05), justifying the application of the non-parametric test. When comparing the percentage removal of each photocatalyst, the Kruskal-Wallis test showed no significant difference (p-value > 0.05). As a result, the semiconductors junction (CN25 and CN75) did not significantly increase the dye removal compared with the pristine photocatalysts (P25 and CN).

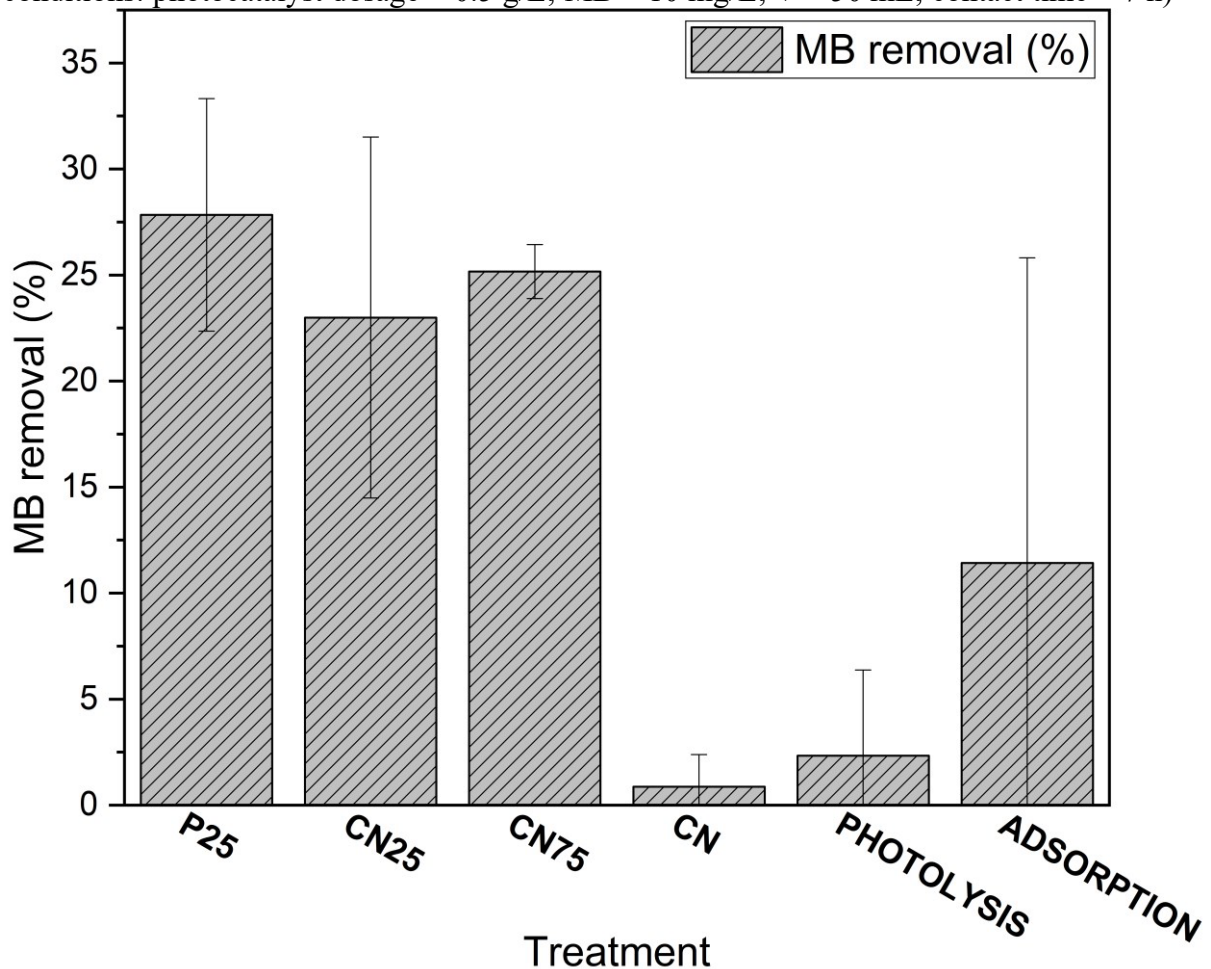
Table 3 – Statistical tests of dye removal data by photocatalyst under artificial light

Statistical test	p-value
Shapiro-Wilk	0.021
Kruskal-Wallis	0.261

Source: elaborated by the author.

Figure 3 shows the MB removal for each photocatalyst submitted to experimental conditions in reactor A. Data obtained with CN25 ($\bar{x} = 25.2\%$; $\sigma = 8.5$), CN75 ($\bar{x} = 23.0\%$; $\sigma = 1.3$), and CN ($\bar{x} = 0.9\%$; $\sigma = 1.5$) appointed enhancement of CN photocatalytic activity by adding P25 in fabricated composites. The low photocatalytic activity of CN is attributed to its high recombination of electron-hole pairs (GE *et al.*, 2012). On the other hand, the photocatalytic performance of CN25 and CN75 composites was lower than P25 ($\bar{x} = 27.8\%$; $\sigma = 5.5$).

Figure 3 – MB removal by photocatalysts under artificial light in reactor A (Experimental conditions: photocatalyst dosage = 0.5 g/L; MB = 10 mg/L; V = 50 mL; contact time = 7 h)



Source: elaborated by the author.

MB solutions were submitted to photolysis, reaching average dye removal of 2.3% ($\sigma = 4.1$). Photolysis showed a small removal compared to values obtained for photocatalysis. The stability of the MB molecules can prevent degradation by direct photolysis, becoming dye removal difficult (MOHAMED *et al.*, 2018a). Franco *et al.* (2009) observed the removal of 20% in a photolysis experiment with MB solution (20 mg/L) promoted by 450 W mercury vapor lamp (Hanovia) at 120 min. The evaluation of the adsorption effect resulted in a color removal of 4.6% ($\sigma = 5.3$).

3.2 Photocatalysis of composites under sunlight

The photocatalysts activity (P25, CN25, CN75, and CN) was investigated under sunlight in reactor B. Since intensity light is a non-controllable factor, the experiments were performed in triplicate randomly, i.e., each replicate was tested on a particular day.

The MB removal values were submitted to statistical tests (Table 4). According to the statistical analysis, the MB removal values showed normal behavior (p -value < 0.05). As the results obtained in reactor A, no statistical significance (p -value > 0.05) was found between dye removals from photocatalysts.

Table 4 – Statistical tests of dye removal data by photocatalysts under sunlight

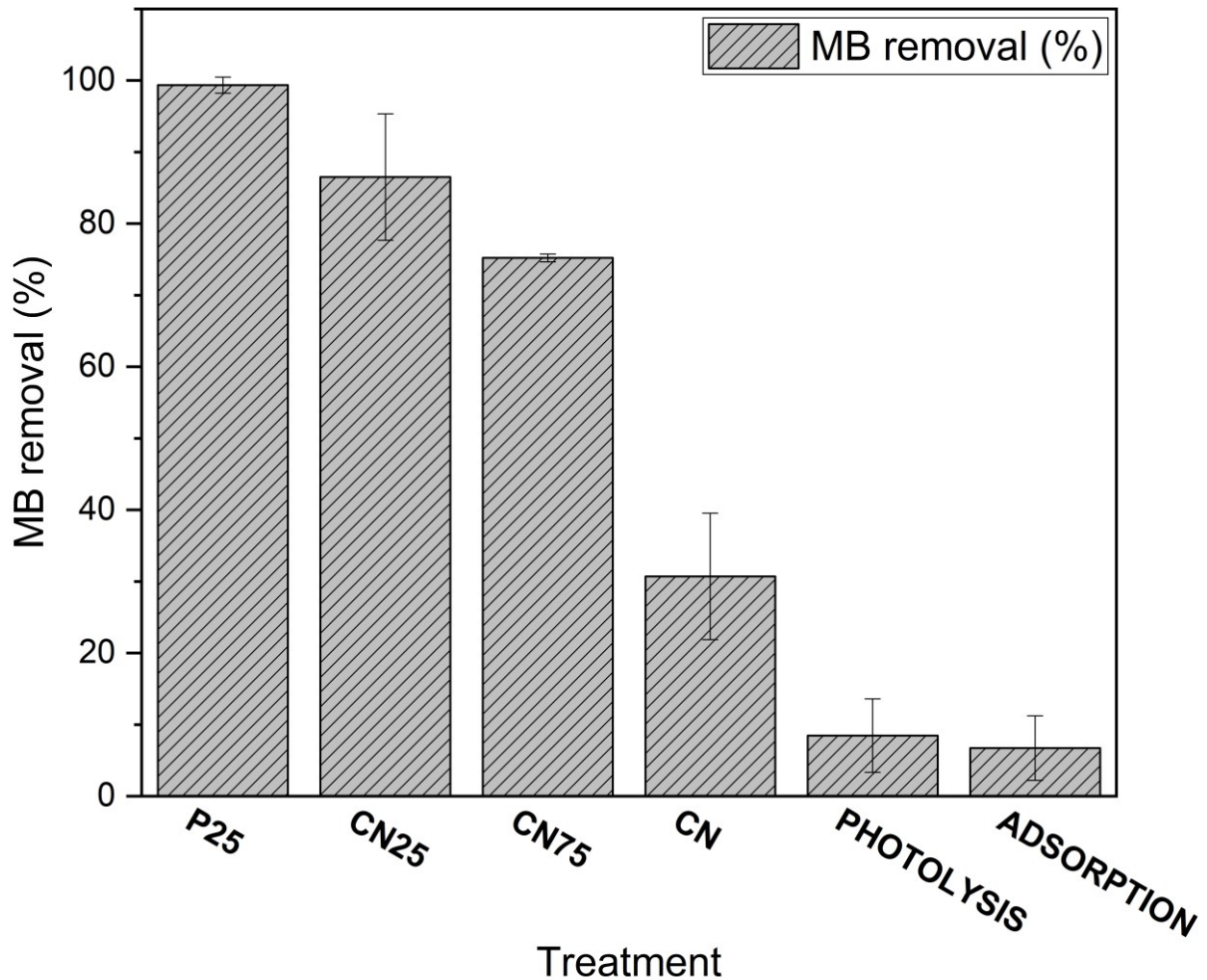
Statistical test	p-value
Shapiro-Wilk	0.045
Kruskal-Wallis	0.083

Source: elaborated by the author.

Photocatalysts activated by sunlight showed a considerable improvement in percentage terms (Figure 4), but the behavior of dye removal data was similar to those observed in reactor A. The best photocatalytic performance was developed by P25 ($\bar{x} = 93.6\%$; $\sigma = 2.2$), while CN ($\bar{x} = 26.6\%$; $\sigma = 10.4$) had the least photocatalytic activity. The CN25 ($\bar{x} = 86.1\%$; $\sigma = 13.9$) and CN75 ($\bar{x} = 69.9\%$; $\sigma = 9.2$) composites presented lower removals compared to P25, indicating that it was determining for the dye removal.

Photolysis by sunlight achieved a dye removal of 8.5% ($\sigma = 5.1$) after 1 h in reactor B. This value was higher than the percentage of 4.6% observed in reactor A. Matos *et al.* (2019) submitted MB solution (12.5 mg/L) to photolysis under artificial sunlight and considered the removal of around 5% as negligent.

Figure 4 – MB removal by photocatalysts under artificial light in reactor B (Experimental conditions: photocatalyst dosage = 0.5 g/L; MB = 10 mg/L; V = 200 mL; contact time = 1 h; agitation speed = 50 rpm)



Source: elaborated by the author.

A new approach was applied to conduct the study with sunlight. Replicates were tested under the same light conditions, but now monitoring the sunlight irradiation intensity. From the statistical analysis (Table 5), the dye removal data showed a normal behavior (p -value < 0.05) and Kruskal-Wallis test indicated significant statistical difference (p -value < 0.05) between the MB removals.

Table 5 – Statistical tests of dye removal data by photocatalyst under sunlight with light intensity monitoring

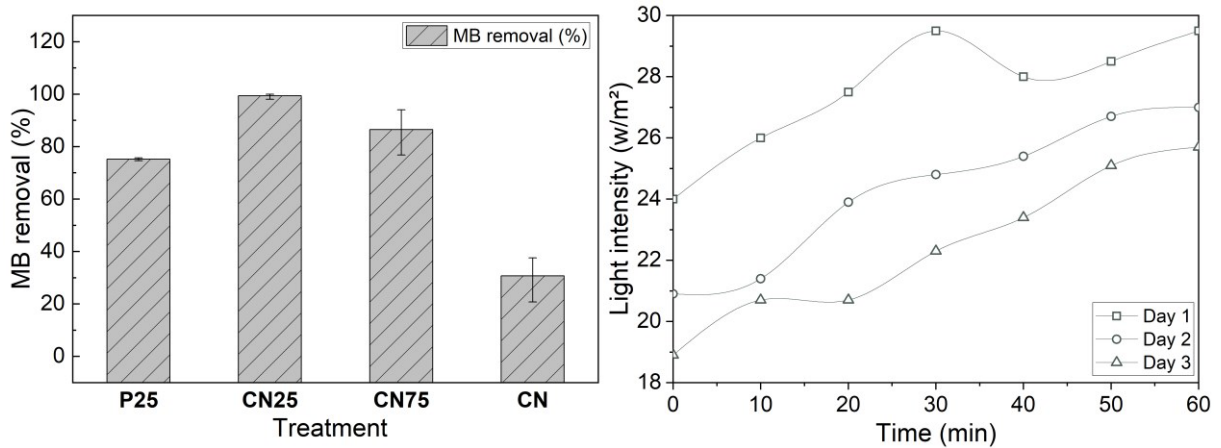
Statistical test	p-value
Shapiro-Wilk	0.033
Kruskal-Wallis	0.007

Source: elaborated by the author.

Figure 5A contains MB removals for P25 ($\bar{x} = 99.4\%$; $\sigma = 1.1$), CN25 ($\bar{x} = 85.5\%$; $\sigma = 8.8$), CN75 ($\bar{x} = 75.2\%$; $\sigma = 0.5$), and CN ($\bar{x} = 30.7\%$; $\sigma = 8.8$). Findings showed the same behavior as the previous stages, appointing the P25 as photocatalyst with better photocatalytic activity. In addition, CN did not improve the photocatalytic performance of P25 in any of the light sources. Arce-Sarria *et al.* (2017) observed that modified TiO₂ P25 via hydrothermal method did not improve the potassium hexacyanoferrate (III) removal, attributing to the loss of the rutile phase and material crystallinity.

Variations in light intensity were observed by a UV meter every 10 minutes during 1 h of sun exposure (Figure 5B). The average light intensity recorded was 27.6, 24.3, and 22.4 W/m² ($\bar{x} = 24.76$ W/m²; $\sigma = 309$) for each day. This change promoted a reduction in removal standard deviation and statistical significance between photocatalytic treatments. Furthermore, values for MB removal were close to those obtained with variable light intensity. Dai *et al.* (2003) registered the light intensity of 4 W/m² in a reactor distanced 1 cm from the LED light.

Figure 5 – (A) MB removal by photocatalysts under sunlight irradiation and (B) light intensity data recorded in reactor B (Experimental conditions: photocatalyst dosage = 0.5 g/L; MB = 10 mg/L; V = 200 mL; contact time = 1 h; agitation speed = 50 rpm)



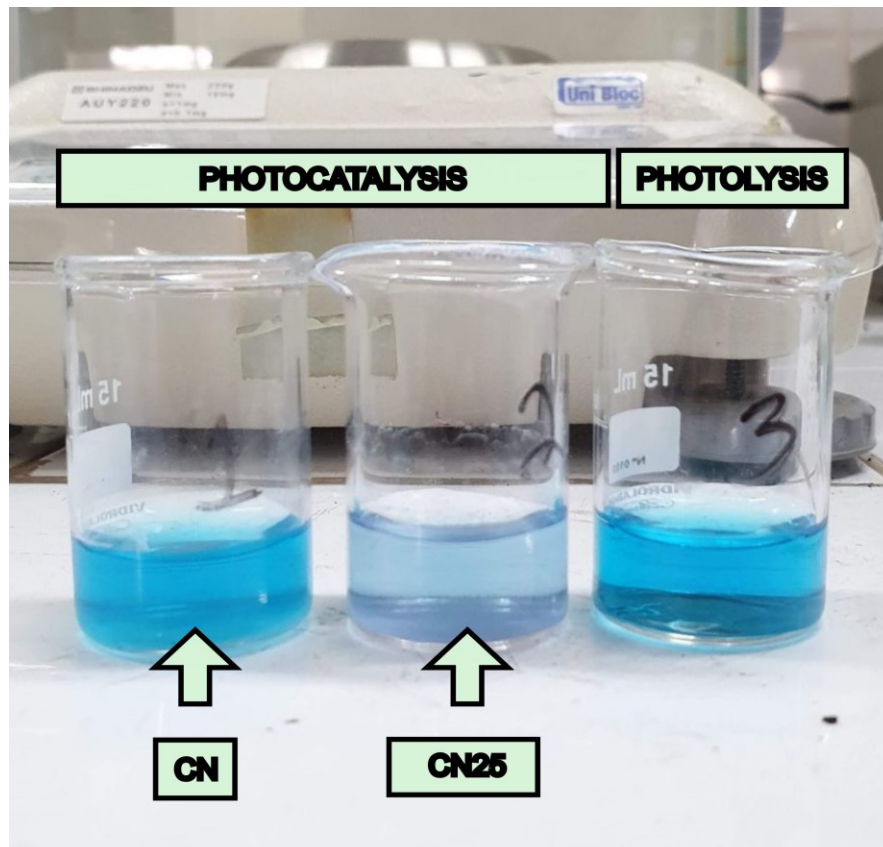
Source: elaborated by the author.

P25 provided the highest percentages of MB removal among the photocatalysts. This material contains a strong interparticle contact between anatase and rutile nanocrystals, contributing to efficient charge separation (SANG; LIU; UMAR, 2015). The great photoactivity of mixed-phase TiO₂ (anatase and rutile) can be explained by: the extension of photoactivity to the visible region by rutile small bandgap; stabilization of charge separation by electron transfer; "hot spots" production in the interface (HURUM *et al.*, 2003). UV region represents only 5% solar spectrum, but its photonic energy is higher than visible and infrared regions (WANG *et*

al., 2017). Photons with wavelengths <380 nm can promote TiO_2 excitation, generating electrons and holes to initiate oxidation-reduction reactions on the photocatalyst surface (CHAKER *et al.*, 2016; KHATAEE; KASIRI; ALIDOKHT, 2011).

Figure 6 contains three samples after 1 hour of sun exposure to the photocatalysis and photolysis process. Color reduction in MB solution after light exposure time can be attributed to the destruction of the chromophore (DASSANAYAKE; RAJAKARUNA; ABIDI, 2018). When testing artificial and natural light sources, sunlight demonstrated superior performance. Since light source intensity plays a vital role in photocatalytic degradation, generating more photons per unit time and unit area with increasing intensity (DASSANAYAKE; RAJAKARUNA; ABIDI, 2018).

Figure 6 – Dye removal promoted by treatments with different photocatalysts (photocatalysis) and without photocatalyst (photolysis) in reactor B



Source: elaborated by the author.

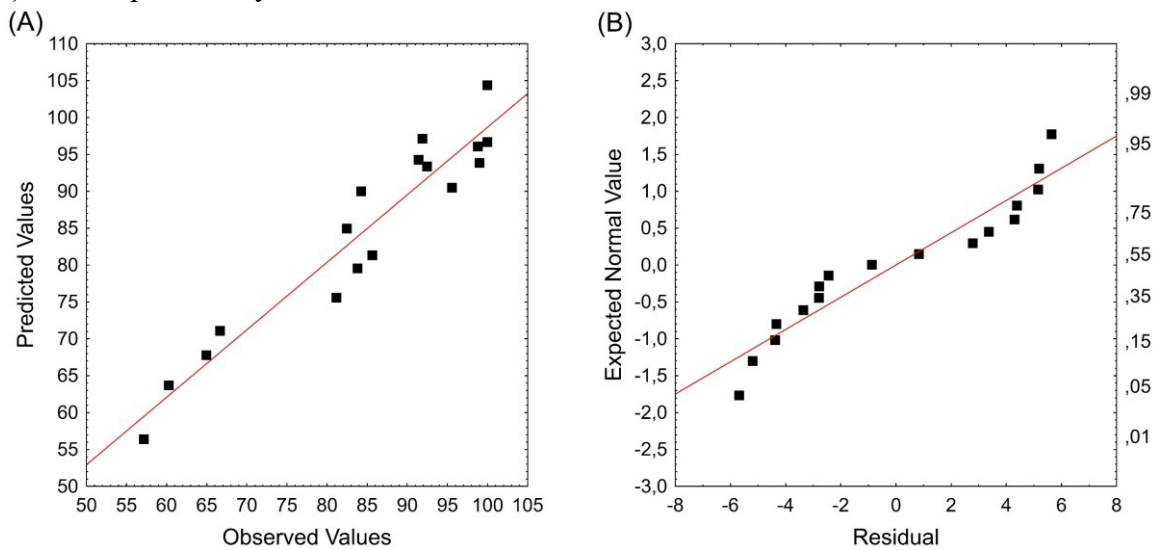
3.3 Central composite design (CCD)

3.3.1 Predictive model

Experimental design without blocks generated a predictive model with R^2 (determination coefficient) of 0.758 and R^2 -adjusted (adjusted determination coefficient) of 0.446. Dye removals were organized according to light intensity into three blocks, generating a predictive model with R^2 of 0.915 and R^2 -adjusted of 0.729. The model produced with blocks was considered reasonable since the difference between coefficients was less than 0.2 (MOHSENZADEH; MIRBAGHERI; SABBAGHI, 2019).

Figure 7A shows the predicted and experimental values for MB removal. The proximity of experimental and predicted results indicated a good fit for the model (NOMAN *et al.*, 2019). The normal probability plot of residuals indicates whether residuals follow a normal distribution (FATHINIA *et al.*, 2010; MOHSENZADEH; MIRBAGHERI; SABBAGHI, 2019). Figure 7B contains residues of experimental and predicted data. The data approached the linear trend confirming normal distribution.

Figure 7 – Plot of (A) experimental responses *versus* predicted responses for MB removal and (B) normal probability for raw residuals



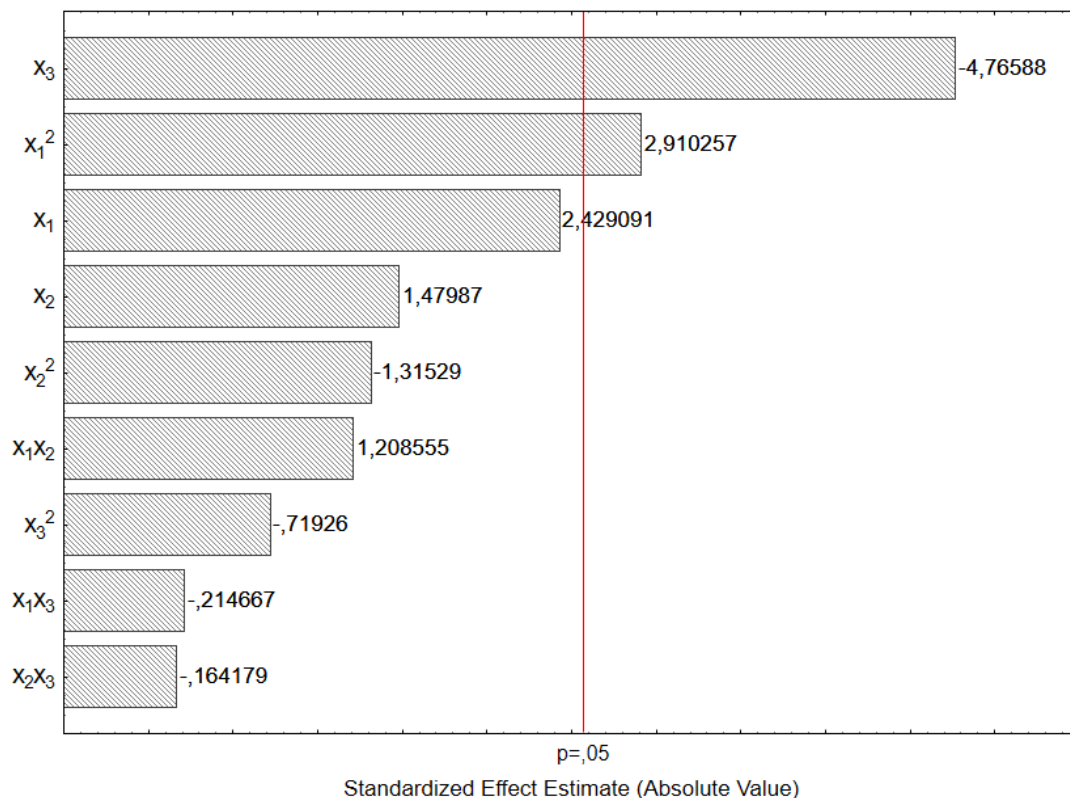
Source: elaborated by the author.

A second-order quadratic expression was proposed to model MB removal (y) as a function of pH (x_1), P25 dosage (x_2), and initial MB concentration (x_3). The regression equation fitted to data is described by Equation 5.

$$y = 269.4 - 51.4x_1 - 7.7x_2 + 1.1x_3 - 3.4x_1^2 - 12.4x_2^2 - 0.1x_3^2 + 5.6x_1x_2 - 0.1x_1x_3 - 0.2x_2x_3 \quad (5)$$

Pareto analysis provides a more significant information for the interpretation of results (FATHINIA *et al.*, 2010). Pareto chart (Figure 8) was constructed from the experimental results obtained from Central Composite Design (CCD). Factors with significant effects on MB removal were pH (p-value = 0.033 < 0.05) and initial MB concentration (p-value = 0.005 < 0.05). Sahoo and Gupta (2012) also found for MB removal by Ag⁺-doped TiO₂, that the initial dye concentration was a determining factor in photocatalysis (SAHOO; GUPTA, 2012).

Figure 8 – Pareto chart containing the effect of all factors on the MB removal



Source: elaborated by the author.

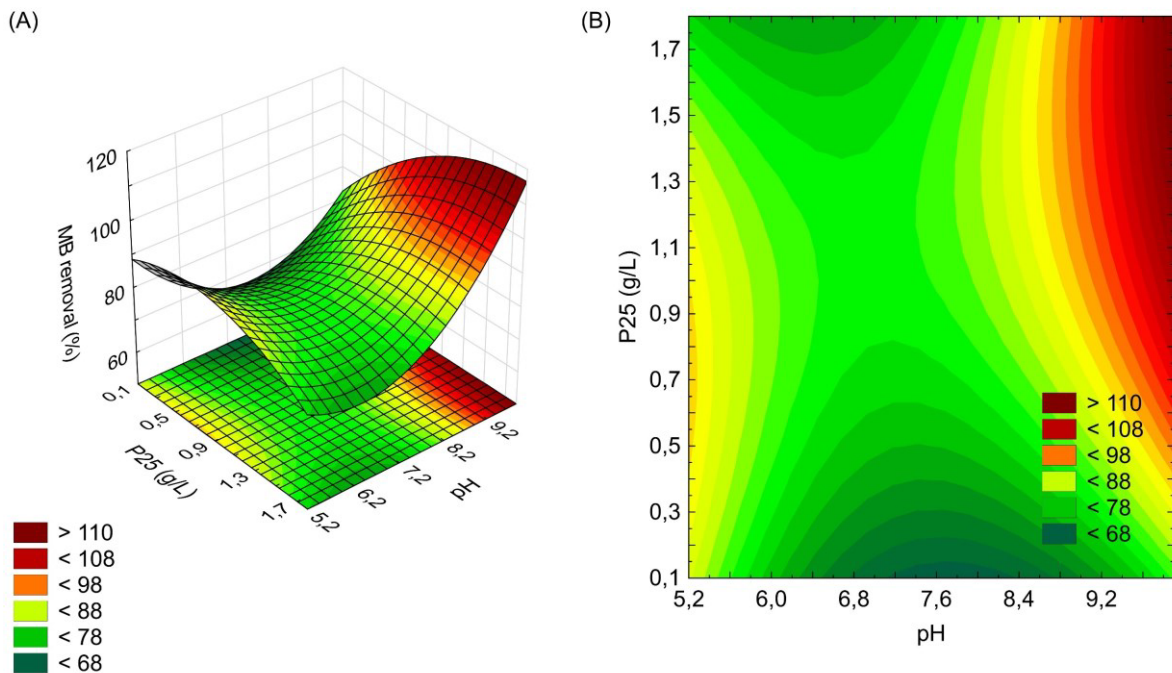
3.3.2 Response surface analysis

The construction of 3D and contour graphs was performed to study the effects of factors on the response variable. Graphs were obtained by varying two factors within experimental ranges and fixing one factor at zero level (SOLEYMANI *et al.*, 2015). Response surface plots provide the knowledge of the interaction between variables and can be used to optimize treatment efficiency (SALARIAN *et al.*, 2016; MYERS; MONTGOMERY; ANDERSON-COOK, 2009).

3D response surface and contour plot of MB removal as a function of P25 dosage

and pH are shown in Figures 9A and 9B. As a result, factors interaction appointed a good photocatalytic performance of P25 under acidic and basic conditions. MB removal reached percentages above 68% in these pH ranges. This behavior was observed over almost the entire P25 dosage range (> 0.15 g/L). Under conditions close to neutrality for fixed value in P25 dosage axis, MB removal was smaller.

Figure 9 – 3D response surface plots (A) and 2D contour plots (B) for P25 *versus* pH (Experimental conditions: $V = 200$ mL; contact time = 1 h; agitation speed = 50 rpm)



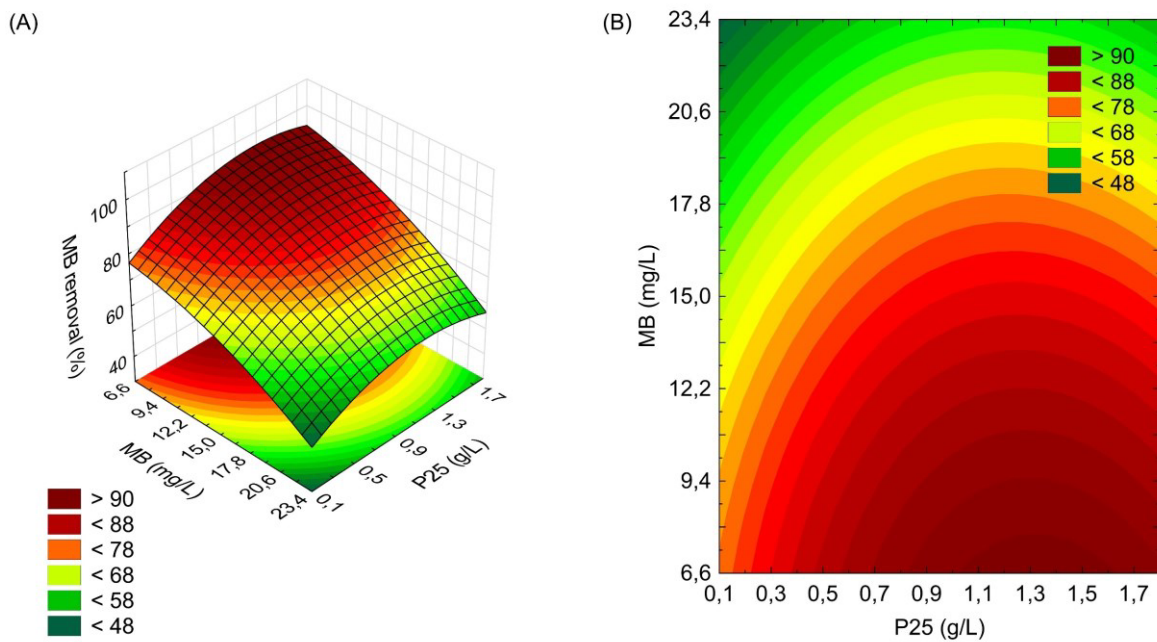
Source: elaborated by the author.

Figure 10A and 10B shows the interaction between MB initial concentration (MB) and photocatalyst dosage (P25). Further increase in initial dye concentration decreased MB removal for all values of P25. This behavior could be related to the filling of photocatalyst active sites by dye, the oxidative species requirement increase, and the reduced light penetration (MOHSENZADEH; MIRBAGHERI; SABBAGHI, 2019). Since the rise of initial concentration can block the participation of photons in the photocatalytic process (KONSTANTINOU; ALBANIS, 2004). In addition, competition between pollutants and intermediate products for active sites also can impair photocatalysis (FATHINIA *et al.*, 2010).

The region formed between 1.0 and 1.5 g/L in the P25 axis appointed negligible effect of the increasing dosage on MB removal (Figure 10B). Photocatalyst concentrations below 1 g/L considerably improved MB removal with the addition of P25. Despite that, the range of values (1.0-1.5 g/L) promoted the highest dye removals for a wide range of MB. The

initial increase of photocatalyst dosage aided the absorption more photons on photocatalyst surface due to the greater availability of active sites, promoting a more efficient degradation (SALARIAN *et al.*, 2016), and also helped to produce more oxidative species (SAHOO; GUPTA, 2012).

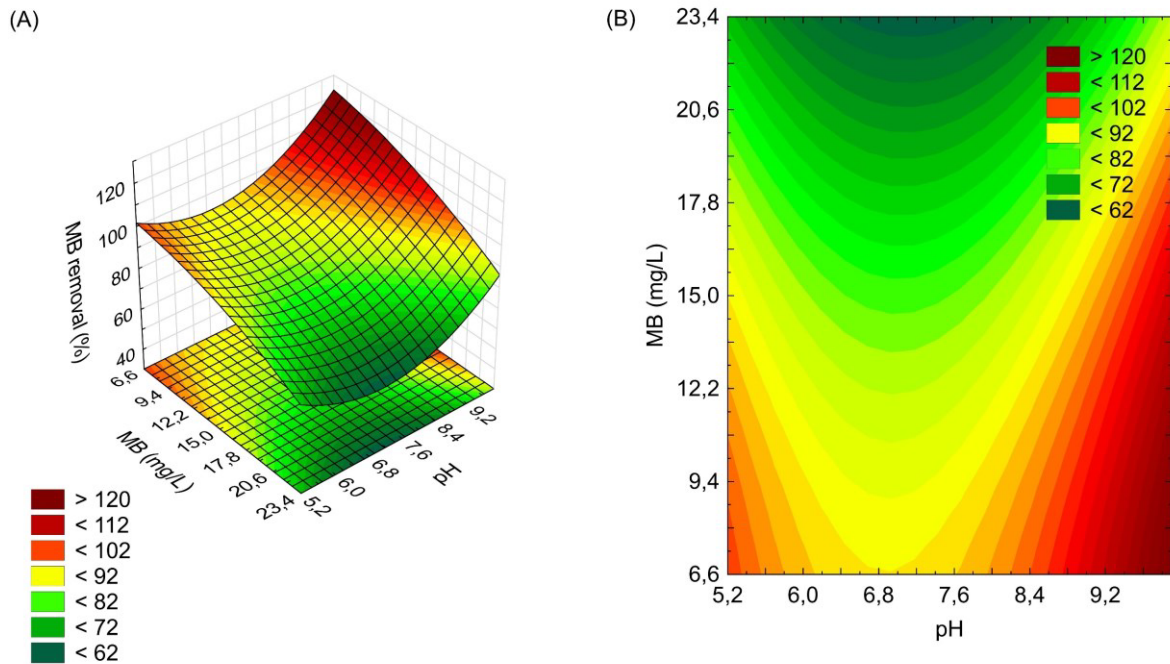
Figure 10 – 3D response surface plots (A) and 2D contour plots (B) for MB *versus* P25 (Experimental conditions: V = 200 mL; contact time = 1 h; agitation speed = 50 rpm)



Source: elaborated by the author.

Figure 11A and 11B displays 3D response surface and contour plot for the initial MB concentration and pH. MB removals were higher than 68% at the all values range for pH and MB. Findings showed a slight decrease in dye removal under neutral conditions.

Figure 11 – 3D response surface plots (A) and 2D contour plots (B) for MB *versus* pH (Experimental conditions: V = 200 mL; contact time = 1 h; agitation speed = 50 rpm)



Source: elaborated by the author.

Generally, heterogeneous photocatalysis has a strong dependence on pH, surface charge state, and band gap potential (SPASIANO *et al.*, 2015). The isoelectric point (IEP) is a point at a specific pH where the particles have no free electrical charge on surfaces (AHMADPOUR *et al.*, 2020). Thus, solid particles are positively and negatively charged at pH values below and above IEP, respectively (WEN *et al.*, 2017). The literature appointed zero-load point (pzc) of TiO₂ (Degussa P25) at pH 6.8 (KONSTANTINOU; ALBANIS, 2004; POULIOS; TSACHPINIS, 1999). The presence of MB (cationic dye) will promote a more electrostatic attraction at an alkaline medium (pH > IEP) and the weakened interaction forces in the adsorbent-adsorbate interface at an acidic medium (pH < IEP). The high dye removal values at acidic pH are attributed to the minimum MB concentration values tested.

In graphics between P25 *versus* pH (Figure 9A and 9B) and MB *versus* pH (Figure 11A and 11B) were verified removal values greater than 100%. 3D surface and contour had axes limited by CCD axial points. Some experimental results inserted in CCD obtained an MB total removal, which can contribute to the extrapolation of predicted values. High removals reached under acid and alkaline conditions also can affect results since pH was significant for the model. In addition, model accuracy ($R^2 = 0.915$; R^2 -adjusted = 0.729) also contributed for values above 100%.

3.3.3 Determination of optimal conditions for MB removal

One of the main objectives on modeling is to determine factors optimal value to maximize model response (HEIDARI *et al.*, 2020). The modeling allows the determination of the critical point. However, it can represent the maximum, minimum, or saddle point on the response surface graph (BEZERRA *et al.*, 2008). The critical values for MB removal by P25 were pH = 6.6, P25 dosage = 1.2 g/L, and MB concentration = 1 mg/L (Table 6). These conditions achieved 97.26% removal.

Table 6 – Critical values of the factors for MB removal

Factors	Observed minimum	Critical value	Observed maximum
pH	5.2	6.6	9.9
P25	0.2	1.2	1.8
MB	6.6	1.0	23.5

Source: elaborated by the author.

The modeling produced 3D response surfaces that approached the saddle shape. According to the literature, optimal values could be located at the ends of the graph saddles (HIBBERT, 2012). The highest MB removals were observed in regions far from critical points area. These areas appeared in graph extremes of MB *versus* pH (Figure 11A). The graph of P25 *versus* pH also showed higher values at edges, indicating that the critical points did not correspond to the maximum value. The saddle point is the inflection point between a relative maximum and a relative minimum (BREIG; LUTI, 2021).

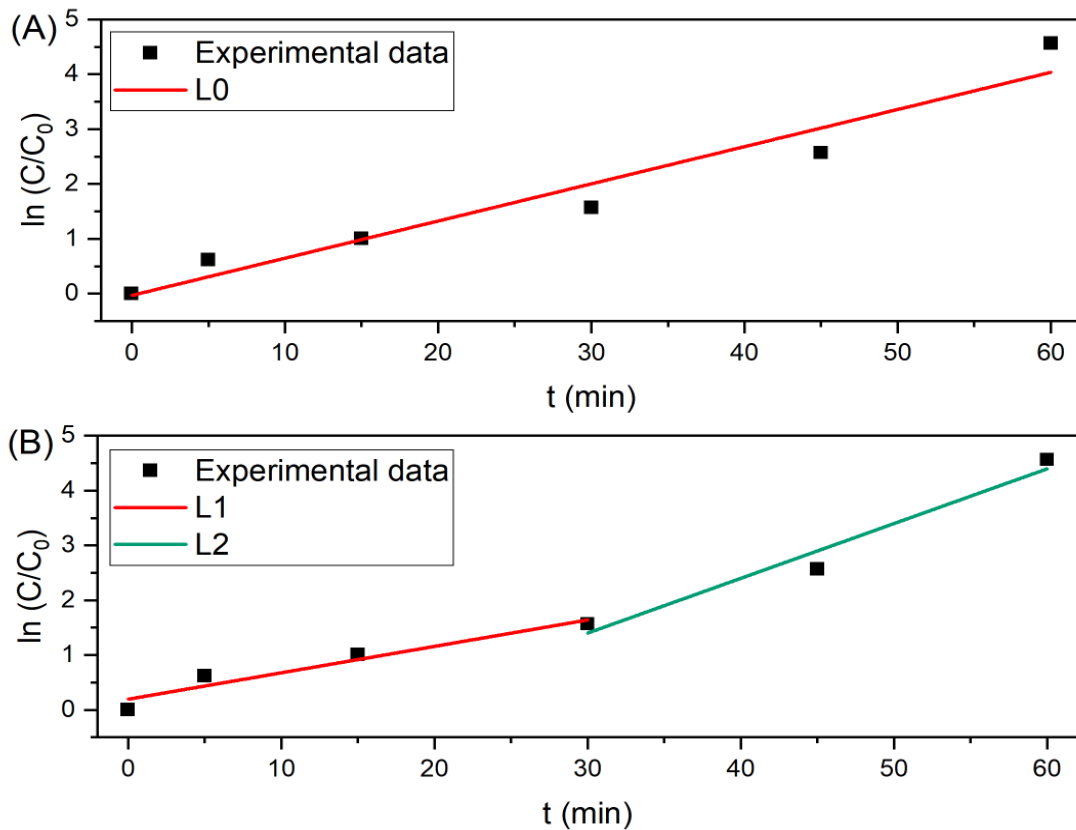
In graph of MB *versus* P25 (Figure 10A), the critical point for MB remained beside graph boundaries. The surface obtained a format similar to the 3D graph whose surface shape indicated a maximum point outside the experimental region (NAIR; MAKWANA; AHAMMED, 2014). P25 critical point was located in a region with the highest removal, but its values showed a growing trend. Şimşek *et al.* (2018) plotted a response surface with the same trend on the data and determined a critical point as saddle point.

Among critical points, only P25 dosage and pH were used in the photocatalysis kinetic study. As the MB concentration of 10 mg/L was used previously in other experiments, the value continued to be adopted. Critical points were not absolute maximum points, but the predictive model found a removal of 97.26%.

3.4 Kinetics of photocatalysis

Average dye concentration was used to plot $\ln(C_0/C_t)$ versus irradiation time (t). Initially, collected experimental data were fitted to a straight line (L0) (Figure 12A). Subsequently, data were fitted to two straight lines (Figure 12B). The first (L1) corresponded to the process in initial 30 minutes, while the second (L2) represented the removal along the final 30 minutes.

Figure 12 – First-order kinetic model of MB removal by P25 adjusted to L1 and (B) L1 and L2 (Experimental conditions: pH = 6.6; P25 dosage = 1.2 g/L; MB = 10 mg/L; V = 200 mL; contact time = 1 h; agitation speed = 50 rpm)



Source: elaborated by the author.

Table 7 shows the calculated intercept and slope values for lines L0, L1, and L2. From the first-order model, a kinetic constant (k) of 0.07 min^{-1} was greatly fitted ($R^2 = 0.94$). Futalan *et al.* (2011) determined a k of 0.0018 min^{-1} for the same MB concentration but with a higher dosage of composite (TiO_2 and chitosan) illuminated by an artificial light source.

Kinetic constants determined for L1 and L2 were 0.05 ($R^2 = 0.93$) and 0.10 min^{-1} ($R^2 = 0.96$), respectively. P25 obtained an rate for L2 with L1 value doubled, appointing to reactions more speedily after the half exposure time. Dias and Azevedo (2009) studied the removal of a solution containing three dyes (Acid Blue 9, xanthenic Acid Red 51, and azo Acid Yellow 23) by P25 under sunlight, obtaining k of 0.0033 between 0 and 75 minutes and 0.0015 between 75 and 120 minutes.

Table 7 – Parameters of linear fit for MB removal by P25

Linear fit	Intercept	Slope	R-Square
L0	-0.03	0.07	0.94
L1	0.19	0.05	0.93
L2	-1.59	0.10	0.96

Source: elaborated by the author.

MB removal of 98.9% ($\sigma = 1.85$) was observed in the experiments to study the kinetic rate of photocatalysis. The initial concentration of MB (10 mg/L) used was higher than the value appointed as the critical point (1 mg/L), although MB removal reached the predicted value (97.3%). These results show as sunlight-activated photocatalysis is promising.

4 CONCLUSIONS

Photocatalysts synthesized with titanium dioxide (P25) and graphitic carbon nitride (CN) showed photocatalytic activity in artificial light and natural sunlight. From the heterogeneous photocatalysis with coupled and pristine semiconductors were observed the following points: (i) the CN25 and CN75 composites improved the photocatalytic activity of CN (ii) the photocatalytic activity of P25 was superior to the manufactured composites; (iii) natural sunlight provided higher percentages of removal compared to artificial light; (iv) exposure of photocatalysts at the same intensity of irradiation is a significant aspect for the statistical treatment.

The predictive model ($R^2 = 0.91$) generated by Central Composite Design (CCD) allowed the identification of pH and initial concentration as the main factors in MB removal. It also determined critical points for pH (6.6), P25 dosage (1.2 mg/L), and MB concentration (1 mg/L). From CCD, it was possible to observe P25 great performance in natural sunlight under acidic and basic conditions.

P25 without modifications obtained better photocatalytic performance, reaching

value average dye removal of 99.4%. Photocatalysis removed 98.9% of the initial MB concentration (10 mg/L) at 1 h with a rate of 0.07 min^{-1} . In final 30 minutes the removal rate doubled. The Brazilian northeast receives abundant natural solar radiation with approximately 10 h of sunlight daily, making it a place with the potential to develop treatments based on solar photocatalysis (BATISTA *et al.*, 2017). Photocatalyst immobilization is crucial for future applications of photocatalytic treatment in large-scale systems. For this reason, efforts will focus on ensuring photocatalyst impregnation on support materials.

REFERENCES

- AHMAD, M.; ALROZI, R. Optimization of preparation conditions for mangosteen peel-based activated carbons for the removal of Remazol Brilliant Blue R using response surface methodology. **Chemical Engineering Journal**, v. 165, n. 3, p. 883-890, 2010.
- AHMADPOUR, N. *et al.* A potential natural solar light active photocatalyst using magnetic $ZnFe_2O_4@TiO_2/Cu$ nanocomposite as a high performance and recyclable platform for degradation of naproxen from aqueous solution. **Journal of Cleaner Production**, v. 268, 2020.
- AHMED, S.; HAIDER, W. Heterogeneous photocatalysis and its potential applications in water and wastewater treatment: a review. **Nanotechnology**, v. 29, n. 34, 2018.
- ALI, T. *et al.* Enhanced photocatalytic and antibacterial activities of Ag-doped TiO_2 nanoparticles under visible light. **Materials Chemistry and Physics**, v. 212, p. 325-335, 2018.
- ARCE-SARRIA, A. *et al.* Degradation of hexacyanoferrate (III) from gold mining wastewaters via UV-A/LED photocatalysis using modified TiO_2 P25. **Water**, v. 12, n. 9, p. 2531, 2020.
- AZARGOHAR, R.; DALAI, A. Production of activated carbon from Luscar char: Experimental and modeling studies. **Microporous and Mesoporous Materials**, v. 85, n. 3, p. 219-225, 2005.
- BARAHIMI, V.; MOGHIMI, H.; TAHERI, R. A. Cu doped $TiO_2-Bi_2O_3$ nanocomposite for degradation of azo dye in aqueous solution: Process modeling and optimization using central composite design. **Journal of Environmental Chemical Engineering**, v. 7, n. 3, 2019.
- BATISTA, L. *et al.* Solar photocatalytic application of NbO_2OH as alternative photocatalyst for water treatment. **Science of The Total Environment**, v. 596-597, p. 79-86, 2017.
- BETHI, B. *et al.* Nanomaterials-based advanced oxidation processes for wastewater treatment: A review. **Chemical Engineering and Processing - Process Intensification**, v. 109, p. 178-189, 2016.
- BEZERRA, M. *et al.* Response surface methodology (RSM) as a tool for optimization in analytical chemistry. **Talanta**, v. 76, n. 5, p. 965-977, 2008.
- BORGES, M. *et al.* Photocatalysis with solar energy: Sunlight-responsive photocatalyst based on TiO_2 loaded on a natural material for wastewater treatment. **Solar Energy**, v. 5, p. 527-535, 2016.
- CHAKER, H. *et al.* Photocatalytic degradation of methyl orange and real wastewater by silver doped mesoporous TiO_2 catalysts. **Journal of Photochemistry and Photobiology A: Chemistry**, v. 318, p. 142-149, 2016.
- CHEN, Y. *et al.* The fabrication of self-floating Ti^{3+}/N co-doped TiO_2 /diatomite granule catalyst with enhanced photocatalytic performance under visible light irradiation. **Applied**

Surface Science, v. 467-468, p. 514-525, 2019.

CHI, L. *et al.* Novel g-C₃N₄/TiO₂/PAA/PTFE ultrafiltration membrane enabling enhanced antifouling and exceptional visible-light photocatalytic self-cleaning. **Catalysis Today**, v. 335, p. 527-537, 2019.

DAI, K. *et al.* Facile synthesis of a surface plasmon resonance-enhanced Ag/AgBr heterostructure and its photocatalytic performance with 450 nm LED illumination. **Dalton Transactions**, v. 42, n. 13, 2013.

DARIANI, R. *et al.* Photocatalytic reaction and degradation of methylene blue on TiO₂ nano-sized particles. **Optik**, v. 127, n. 18, p. 7143-7154, 2016.

DIAS, M.; AZEVEDO, E. Photocatalytic decolorization of commercial acid dyes using solar irradiation. **Water, Air, and Soil Pollution**, v. 204, n. 1-4, p. 79-87, 2009.

DU, X. *et al.* Visible-light activation of persulfate by TiO₂/g-C₃N₄ photocatalyst toward efficient degradation of micropollutants. **Chemical Engineering Journal**, v. 384, n. 13, 2020.

FATHINIA, M. *et al.* Comparative photocatalytic degradation of two dyes on immobilized TiO₂ nanoparticles: Effect of dye molecular structure and response surface approach. **Journal of Molecular Catalysis A: Chemical**, v. 333, n. 1-2, p. 73-84, 2010.

FOTIOU, T. *et al.* Assessment of the roles of reactive oxygen species in the UV and visible light photocatalytic degradation of cyanotoxins and water taste and odor compounds using C-TiO₂. **Water Research**, v. 90, p. 52-61, 2016.

FRANCO, A. *et al.* Photocatalytic decolorization of methylene blue in the presence of TiO₂/ZnS nanocomposites. **Journal of Hazardous Materials**, v. 161, n. 1, p. 545-550, 2009.

FUTALAN, C. *et al.* Comparative and competitive adsorption of copper, lead, and nickel using chitosan immobilized on bentonite. **Carbohydrate Polymers**, v. 83, n. 2, p. 528-536, 2011.

GE, L. *et al.* Synthesis and efficient visible light photocatalytic hydrogen evolution of polymeric g-C₃N₄ coupled with CdS quantum dots. **The Journal of Physical Chemistry C**, v. 116, n. 25, p. 13708-13714, 2012.

GUNARATNE, H. *et al.* 'All in one' photo-reactor pod containing TiO₂ coated glass beads and LEDs for continuous photocatalytic destruction of cyanotoxins in water. **Environmental Science: Water Research & Technology**, v. 6, n. 4, p. 945-950, 2020.

HEIDARI, Z. *et al.* Degradation of furosemide using photocatalytic ozonation in the presence of ZnO/ICLT nanocomposite particles: Experimental, modeling, optimization and mechanism evaluation. **Journal of Molecular Liquids**, v. 319, 2020.

HIBBERT, D. Experimental design in chromatography: a tutorial review. **Journal of chromatography B**, v. 910, p. 2-13, 2012.

HURUM, D. *et al.* Explaining the enhanced photocatalytic activity of Degussa P25 mixed-

phase TiO₂ using EPR. **The Journal of Physical Chemistry B**, v. 107, n. 19, p. 4545-4549, 2003.

JO, W.; TAYADE, R. New generation energy-efficient light source for photocatalysis: LEDs for environmental applications. **Industrial & Engineering Chemistry Research**, v. 53, n. 6, p. 2073-2084, 2014.

KASSAHUN, S. *et al.* Process optimization and kinetics analysis for photocatalytic degradation of emerging contaminant using N-doped TiO₂-SiO₂ nanoparticle: Artificial Neural Network and Surface Response Methodology approach. **Environmental Technology & Innovation**, v. 23, 2021.

KHATAEE, A. R.; KASIRI, M. B.; ALIDOKHT, L. Application of response surface methodology in the optimization of photocatalytic removal of environmental pollutants using nanocatalysts. **Environmental technology**, v. 32, n. 15, p. 1669-1684, 2011.

KIM, S. *et al.* Recent progress in solar cell technology for low-light indoor applications. **Curr. Altern. Energy**, v. 3, n. 1, p. 3-17, 2019.

KONG, L. *et al.* Ti³⁺ defect mediated g-C₃N₄/TiO₂ Z-scheme system for enhanced photocatalytic redox performance. **Applied Surface Science**, v. 448, p. 288-296, 2018.

KONSTANTINOU, I.; ALBANIS, T. TiO₂-assisted photocatalytic degradation of azo dyes in aqueous solution: kinetic and mechanistic investigations. **Applied Catalysis B: Environmental**, v. 49, n. 1, p. 1-14, 2004.

LIU, J.; WANG, H.; ANTONIETTI, M. Graphitic carbon nitride “reloaded”: emerging applications beyond (photo) catalysis. **Chemical Society Reviews**, v. 45, n. 8, p. 2308-2326, 2016.

MA, L. Synthesis of core-shell TiO₂@ g-C₃N₄ hollow microspheres for efficient photocatalytic degradation of rhodamine B under visible light. **Applied surface science**, v. 430, p. 263-272, 2018.

MA, J.; WANG, C.; HE, H. Enhanced photocatalytic oxidation of NO over g-C₃N₄-TiO₂ under UV and visible light. **Applied Catalysis B: Environmental**, v. 184, p. 28-34, 2016.

MACHROUHI, A. *et al.* Statistical optimization of activated carbon from *Thapsia transtagana* stems and dyes removal efficiency using central composite design. **Journal of Science: Advanced Materials and Devices**, v. 4, n. 4, p. 544-553, 2019.

MATOS, J. *et al.* C-doped anatase TiO₂: Adsorption kinetics and photocatalytic degradation of methylene blue and phenol, and correlations with DFT estimations. **Journal of Colloid and Interface Science**, v. 547, p. 14-29, 2019.

MAZHARI, M. *et al.* Central composite design (CCD) optimized synthesis of Fe₃O₄@SiO₂@AgCl/Ag/Ag₂S as a novel magnetic nano-photocatalyst for catalytic degradation of organic pollutants. **Journal of Environmental Chemical Engineering**, v. 6, n. 6, p. 7284-7293, 2018.

- MOHAMED, M. *et al.* In-depth understanding of core-shell nanoarchitecture evolution of g-C₃N₄@C, N co-doped anatase/rutile: Efficient charge separation and enhanced visible-light photocatalytic performance. **Applied Surface Science**, v. 436, p. 302-318, 2018.
- MOHSENZADEH, M.; MIRBAGHERI, S.; SABBAGHI, S. Degradation of 1,2-dichloroethane by photocatalysis using immobilized PANi-TiO₂ nano-photocatalyst. **Environmental Science and Pollution Research**, v. 26, n. 30, p. 31328-31343, 2019.
- MONTEAGUDO, J. *et al.* Effect of reduced graphene oxide load into TiO₂ P25 on the generation of reactive oxygen species in a solar photocatalytic reactor. **Chemical Engineering Journal**, v. 380, 2020.
- MYERS, R.; MONTGOMERY, D.; ANDERSON-COOK, C. **Response surface methodology: process and product optimization using designed experiments**. John Wiley & Sons, 2016.
- NAIR, A.; MAKWANA, A.; AHAMMED, M. The use of response surface methodology for modelling and analysis of water and wastewater treatment processes: a review. **Water science and technology**, v. 69, n. 3, p. 464-478, 2014.
- NOMAN, M. T. *et al.* One-pot sonochemical synthesis of ZnO nanoparticles for photocatalytic applications, modelling and optimization. **Materials**, v. 13, n. 1, p. 14, 2019.
- PÉREZ, M. Fenton and photo-Fenton oxidation of textile effluents. **Water Research**, v. 36, n. 11, p. 2703–2710, 2002.
- POULIOS, I.; TSACHPINIS, I. Photodegradation of the textile dye Reactive Black 5 in the presence of semiconducting oxides. **Journal of Chemical Technology & Biotechnology**, v. 74, n. 4, p. 349–357, 1999.
- RAZALI, N.; WAH, Y. Power comparisons of Shapiro-Wilk, Kolmogorov-Smirnov, Lilliefors and Anderson-darling tests. **Journal of statistical modeling and analytics**, v. 2, n. 1, p. 21-33, 2011.
- SAEED, M. *et al.* Photocatalysis: an effective tool for photodegradation of dyes—a review. **Environmental Science and Pollution Research**, v. 29, 293-311, 2022.
- SAHOO, C.; GUPTA, A. Optimization of photocatalytic degradation of methyl blue using silver ion doped titanium dioxide by combination of experimental design and response surface approach. **Journal of Hazardous Materials**, v. 215-216, p. 302-310, 2012.
- SALARIAN, A. *et al.* N-doped TiO₂ nanosheets for photocatalytic degradation and mineralization of diazinon under simulated solar irradiation: Optimization and modeling using a response surface methodology. **Journal of Molecular Liquids**, v. 220, p. 183-191, 2016.
- SANG, Y.; LIU, H.; UMAR, A. Photocatalysis from UV/Vis to near-infrared light: towards full solar-light spectrum activity. **ChemCatChem**, v. 7, n. 4, p. 559-573, 2015.
- SENTHILKUMAR, P. *et al.* Adsorption equilibrium, thermodynamics, kinetics, mechanism and process design of zinc(II) ions onto cashew nut shell. **The Canadian Journal of**

Chemical Engineering, v. 90, n. 4, p. 973-982, 2012.

SHESKIN, D. **Parametric and nonparametric statistical procedures**. Boca Raton: CRC, 2000.

ŞİMŞEK, B. *et al.* Analysis of the effects of dioctyl terephthalate obtained from polyethylene terephthalate wastes on concrete mortar: A response surface methodology based desirability function approach application. **Journal of Cleaner Production**, v. 170, p. 437-445, 2018.

SOLEYMANI, A. *et al.* Modeling and optimization of a sono-assisted photocatalytic water treatment process via central composite design methodology. **Process Safety and Environmental Protection**, v. 94, n. C, p. 307-314, 2015.

SONG, J. *et al.* Removal of Microcystis aeruginosa and Microcystin-LR using a graphitic-C₃N₄/TiO₂ floating photocatalyst under visible light irradiation. **Chemical Engineering Journal**, v. 348, p. 380-388, 2018.

SPASIANO, D. *et al.* Solar photocatalysis: Materials, reactors, some commercial, and pre-industrialized applications. A comprehensive approach. **Applied Catalysis B: Environmental**, v. 170-171, p. 90-123, 2015.

TAGHIPOUR, T. *et al.* Photoelectro-Fenton/photocatalytic process for decolorization of an organic compound by Ag: Cd-1,4-BDOAH₂ nano-photocatalyst: Response surface modeling and central composite design optimization. **Journal of Molecular Liquids**, v. 335, 2021.

TAYEL, A.; RAMADAN, A.; EL SEOUD, O. Titanium dioxide/graphene and titanium dioxide/graphene oxide nanocomposites: synthesis, characterization and photocatalytic applications for water decontamination. **Catalysts**, v. 8, n. 11, p. 491, 2018.

VARANK, G. *et al.* Concentrated leachate treatment by electro-fenton and electro-persulfate processes using central composite design. **International Journal of Environmental Research**, v. 14, n. 4, p. 439-461, 2020.

WANG, X. *et al.* Full-spectrum-solar-light-activated photocatalysts for light-chemical energy conversion. **Advanced Energy Materials**, v. 7, n. 23, 2017.

WEN, J. *et al.* A review on g-C₃N₄-based photocatalysts. **Applied Surface Science**, v. 391, p. 72-123, 2017.

WU, Y. *et al.* Mesoporous graphitic carbon nitride and carbon-TiO₂ hybrid composite photocatalysts with enhanced photocatalytic activity under visible light irradiation. **Journal of Environmental Chemical Engineering**, v. 4, n. 1, p. 797-807, 2016.

YU, W. *et al.* Enhanced visible light photocatalytic degradation of methylene blue by F-doped TiO₂. **Applied Surface Science**, v. 319, n. 1, p. 107-112, 2014.

ZHANG, Y. *et al.* Strongly interfacial-coupled 2D-2D TiO₂/g-C₃N₄ heterostructure for enhanced visible-light induced synthesis and conversion. **Journal of hazardous materials**, v. 394, 2020.

GENERAL CONCLUSIONS

The scientific community has aimed increasing become treatment processes of pollutants more sustainable. Heterogeneous photocatalysis promoted pollutant removal using clean energy sources such as sunlight. For this, semiconductor materials must absorb the photons available in sunlight and produce oxidative reactive species.

Chapter I contributed to discovering trends in the synthetic methods of composites with titanium dioxide and graphitic carbon nitride. Calcination is the method most applied in the synthesis field. Titanium dioxide was found with several morphologies in composites. Among shapes, nanoparticle was produced by many synthetic processes. Layer deposition or ALD, vapor deposition, and charge-induced aggregation were new processes observed in publications. Combining recognized methods such as calcination, hydrothermal, and solvothermal was found. Besides semiconductor morphological changes, the varying semiconductor proportions were widely studied for photocatalytic response increase in visible light. Synthetic methods produced photocatalysts with larger surface areas, more active sites, reduced bandgaps, fewer recombination, and a strong interfacial interconnection.

Chapter II contributed to understanding the photocatalytic performance of composites with commercial titanium dioxide (P25) and graphitic carbon nitride (CN) under artificial and natural light sources. In general, the pristine and combined semiconductors showed photocatalytic activity in both light conditions. The photocatalytic activity of CN increased with P25 coupling according to MB removal. The photocatalytic activity of photocatalysts was higher in sunlight. However, P25 obtained the best value for MB removal in all experiments including the higher average removal of 99.4%. From Central Composite Design (CCD) was possible to observe high MB removals in acidic and alkaline conditions. In addition, it determined the critical points to pH (6.6), P25 (1.2 g/L) dosage, and MB concentration (1 mg/L). Photocatalytic kinetics modelling for P25 determined a rate of 0.07 min^{-1} and showed that the MB removal speed doubled in the final 30 minutes. This study indicated the potential of heterogeneous photocatalysis associated with the use of sunlight for depollution.

GENERAL REFERENCES

- AHMED, S.; HAIDER, W. Heterogeneous photocatalysis and its potential applications in water and wastewater treatment: a review. **Nanotechnology**, v. 29, n. 34, 2018.
- AL-MAMUN, M. *et al.* Photocatalytic activity improvement and application of UV-TiO₂ photocatalysis in textile wastewater treatment: A review. **Journal of Environmental Chemical Engineering**, v. 7, n. 5, 2019.
- ARSLAN-ALATON, I.; TURELI, G.; OLMEZ-HANCI, T. Treatment of azo dye production wastewaters using Photo-Fenton-like advanced oxidation processes: Optimization by response surface methodology. **Journal of Photochemistry and Photobiology A: Chemistry**, v. 202, n. 2-3, p. 142-153, 2009.
- BADVI, K.; JAVANBAKHT, V. Enhanced photocatalytic degradation of dye contaminants with TiO₂ immobilized on ZSM-5 zeolite modified with nickel nanoparticles. **Journal of Cleaner Production**, v. 280, 2021.
- BAI, L. *et al.* Kinetics and mechanism of photocatalytic degradation of methyl orange in water by mesoporous Nd-TiO₂-SBA-15 nanocatalyst. **Environmental Pollution**, v. 248, p. 516-525, 2019.
- BASTURK, E.; KARATAS, M. Decolorization of anthraquinone dye Reactive Blue 181 solution by UV/H₂O₂ process. **Journal of Photochemistry and Photobiology A: Chemistry**, v. 299, p. 67-72, 2015.
- BENKHAYA, S.; M' RABET, S.; EL HARFI, A. A review on classifications, recent synthesis and applications of textile dyes. **Inorganic Chemistry Communications**, v. 115, 2020.
- BHANVASE, B.; SHENDE, T.; SONAWANE, S. A review on graphene-TiO₂ and doped graphene-TiO₂ nanocomposite photocatalyst for water and wastewater treatment. **Environmental Technology Reviews**, v. 6, n. 1, p. 1-14, 2017.
- BIANCHI, C. *et al.* Mechanism and efficiency of atrazine degradation under combined oxidation processes. **Applied Catalysis B: Environmental**, v. 64, n. 1-2, p. 131-138, 2006.
- CHATTERJEE, D.; DASGUPTA, S. Visible light induced photocatalytic degradation of organic pollutants. **Journal of Photochemistry and Photobiology C: Photochemistry Reviews**, v. 6, n. 2-3, p. 186-205, 2005.
- DARIANI, R. S. *et al.* Photocatalytic reaction and degradation of methylene blue on TiO₂ nano-sized particles. **Optik**, v. 127, p. 7143-7154, 2016.
- DIN, M. I. *et al.* Fundamentals and photocatalysis of methylene blue dye using various nanocatalytic assemblies – a critical review. **Journal of Cleaner Production**, v. 298, 2021.
- FEIZPOOR, S.; HABIBI-YANGJEH, A.; VADIVEL, S. Novel TiO₂/Ag₂CrO₄ nanocomposites: Efficient visible-light-driven photocatalysts with n-n heterojunctions. **Journal of Photochemistry and Photobiology A: Chemistry**, v. 341, p. 57-68, 2017.
- GÓMEZ-PASTORA, J. *et al.* Review and perspectives on the use of magnetic

nanophotocatalysts (MNPCs) in water treatment. **Chemical Engineering Journal**, v. 310, p. 407-427, 2017.

HERRMANN, J. M. Heterogeneous photocatalysis: state of the art and present. **Topics in Catalysis**, v. 34, n. 1-4, p. 49-65, 2005.

HUANG, J. *et al.* Excellent visible light responsive photocatalytic behavior of N-doped TiO₂ toward decontamination of organic pollutants. **Journal of Hazardous Materials**, v. 403, p. 123857, 2021.

ISARI, A. *et al.* Photocatalytic degradation of rhodamine B and real textile wastewater using Fe-doped TiO₂ anchored on reduced graphene oxide (Fe-TiO₂/rGO): Characterization and feasibility, mechanism and pathway studies. **Applied Surface Science**, v. 462, p. 549-564, 2018.

JOSEPH, A.; VIJAYANANDAN, A. Photocatalysts synthesized via plant mediated extracts for degradation of organic compounds: A review of formation mechanisms and application in wastewater treatment. **Sustainable Chemistry and Pharmacy**, v. 22, 2021.

LI, S. *et al.* A sustainable approach for lignin valorization by heterogeneous photocatalysis. **Green Chemistry**, v. 18, n. 3, p. 594-607, 2016.

LI, Y. *et al.* Seed-induced growing various TiO₂ nanostructures on g-C₃N₄ nanosheets with much enhanced photocatalytic activity under visible light. **Journal of Hazardous Materials**, v. 292, p. 79-89, 2015.

MECHA, A. *et al.* UV and solar photocatalytic disinfection of municipal wastewater: inactivation, reactivation and regrowth of bacterial pathogens. **International Journal of Environmental Science and Technology**, v. 16, n. 7, p. 3687-3696, 2019.

MONGA, D.; BASU, S. Enhanced photocatalytic degradation of industrial dye by g-C₃N₄/TiO₂ nanocomposite: Role of shape of TiO₂. **Advanced Powder Technology**, v. 30, n. 5, p. 1089-1098, 2019.

MOREIRA, N. *et al.* Solar treatment (H₂O₂, TiO₂-P25 and GO-TiO₂ photocatalysis, photo-Fenton) of organic micropollutants, human pathogen indicators, antibiotic resistant bacteria and related genes in urban wastewater. **Water Research**, v. 135, p. 195-206, 2018.

MOUSAVI, M.; HABIBI-YANGJEH, A.; POURAN, S. Review on magnetically separable graphitic carbon nitride-based nanocomposites as promising visible-light-driven photocatalysts. **Journal of Materials Science: Materials in Electronics**, v. 29, n. 3, p. 1719-1747, 2018.

PAN, X. *et al.* Defective TiO₂ with oxygen vacancies: synthesis, properties and photocatalytic applications. **Nanoscale**, v. 5, n. 9, 2013.

PEIRIS, S. *et al.* Recent development and future prospects of TiO₂ photocatalysis. **Journal of the Chinese Chemical Society**, v. 68, n. 5, p. 738-769, 2021.

PONIEDZIAŁEK, B.; RZYMSKI, P.; WIKTOROWICZ, K. Toxicity of cylindrospermopsin

in human lymphocytes: Proliferation, viability and cell cycle studies. **Toxicology in Vitro**, v. 28, n. 5, p. 968-974, 2014.

PRIHOD'KO, R.; SOBOLEVA, N. Photocatalysis: oxidative processes in water treatment. **Journal of Chemistry**, v. 2013, p. 1-8, 2013.

REZA, K. M.; KURNY, A.; GULSHAN, F. Parameters affecting the photocatalytic degradation of dyes using TiO₂: a review. **Applied Water Science**, v. 7, n. 4, p. 1569-1578, 2017.

SARKAR, S. *et al.* Green polymeric nanomaterials for the photocatalytic degradation of dyes: a review. **Environmental Chemistry Letters**, v. 18, n. 5, p. 1569-1580, 2020.

SERPONE, N.; EMELINE, A. V. Semiconductor photocatalysis – past, present, and future outlook. **The Journal of Physical Chemistry Letters**, v. 3, n. 5, p. 673-677, 2012.

SRIKANTH, B. *et al.* Recent advancements in supporting materials for immobilized photocatalytic applications in waste water treatment. **Journal of Environmental Management**, v. 200, p. 60-78, 2017.

SUN, X. *et al.* Surface modification of TiO₂ with polydopamine and its effect on photocatalytic degradation mechanism. **Colloids and Surfaces A: Physicochemical and Engineering Aspects**, v. 570, p. 199-209, 2019.

TAYEL, A.; RAMADAN, A.; EL SEOUD, O. Titanium dioxide/graphene and titanium dioxide/graphene oxide nanocomposites: synthesis, characterization and photocatalytic applications for water decontamination. **Catalysts**, v. 8, n. 11, p. 491, 2018.

TU, H. *et al.* Incorporation of rectorite into porous polycaprolactone/TiO₂ nanofibrous mats for enhancing photocatalysis properties towards organic dye pollution. **Composites Communications**, v. 15, p. 58-63, 2019.

WANG, X. *et al.* Adsorption of methylene blue on azo dye wastewater by molybdenum disulfide nanomaterials. **Sustainability**, v. 14, n. 13, 2022.

WANG, W. *et al.* Advances in photocatalytic disinfection of bacteria: Development of photocatalysts and mechanisms. **Journal of Environmental Sciences**, v. 34, p. 232-247, 2015.

WU, Z. *et al.* Photocatalytic decontamination of wastewater containing organic dyes by metal-organic frameworks and their derivatives. **ChemCatChem**, v. 9, n. 1, p. 41-64, 2017.

XU, M. *et al.* Photodecomposition of NO_x on Ag/TiO₂ composite catalysts in a gas phase reactor. **Chemical Engineering Journal**, v. 307, p. 181-188, 2017.

ZHANG, J. *et al.* Photocatalytic degradation of rhodamine b on anatase, rutile, and brookite TiO₂. **Chinese Journal of Catalysis**, v. 32, n. 6-8, p. 983-991, 2011.

ZHANG, W. *et al.* Photocatalytic performance of ZnGa₂O₄ for degradation of methylene blue and its improvement by doping with Cd. **Catalysis Communications**, v. 11, n. 14, p. 1104-

1108, 2010.

ZHU, D.; ZHOU, Q. Action and mechanism of semiconductor photocatalysis on degradation of organic pollutants in water treatment: A review. **Environmental Nanotechnology, Monitoring & Management**, v. 12, p. 100255, 2019.